OPTICAL FREQUENCY COMB IN A BIOLOGICAL ENVIRONMENT

by

Gwangho Choi

A Dissertation Submitted to the Faculty of the

JAMES C. WYANT COLLEGE OF OPTICAL SCIENCES

In Partial Fulfillment of the Requirements
For the Degree of

DOCTOR OF PHILOSOPHY
WITH A MAJOR IN OPTICAL SCIENCES

In the Graduate College

THE UNIVERSITY OF ARIZONA

2023

THE UNIVERSITY OF ARIZONA
GRADUATE COLLEGE

As members of the Dissertation Committee, we certify that we have read the dissertation prepared by **Gwangho Choi**, titled ***Optical Frequency Comb in a Biological Environment*** and recommend that it be accepted as fulfilling the dissertation requirement for the Degree of Doctor of Philosophy.

Judith Su

Professor Judith Su Date: 4/24/2023

Khanh Kieu Digitally signed by Khanh Kieu
DN: cn=Khanh Kieu, o=UA, ou=OSC, email=kkieu@optics.arizona.edu, c=US
Date: 2023.04.25 15:32:12 -07'00'

Professor Khanh Q. Kieu Date: 4/24/2023

Professor Dalziel Wilson Date: 4/26/23

Final approval and acceptance of this dissertation is contingent upon the candidate's submission of the final copies of the dissertation to the Graduate College.

I hereby certify that I have read this dissertation prepared under my direction and recommend that it be accepted as fulfilling the dissertation requirement.

Judith Su

Professor Judith Su Date: 4/24/2023
Dissertation Committee Chair
Wyant College of Optical Sciences

ACKNOWLEDGEMENTS

I would like to express my deepest gratitude to my advisor, Dr. Judith Su, for her unwavering support, mentorship, and motivation. Her exceptional guidance, patience, and unwavering commitment to my success have been immeasurable, and I am profoundly thankful for her invaluable contributions to my research journey. Dr. Su has not only imparted valuable knowledge and expertise, but she has also exemplified professionalism through her positive attitude, open-mindedness, and respect. Her dedication to excellence and her exemplary professionalism have been truly inspiring, and I am privileged to have had her as my advisor.

I would also like to extend my gratitude to the members of my dissertation committee, Dr. Khanh Kieu and Dr. Dal Wilson, for their valuable insights, feedback, and suggestions. Their expertise and constructive criticisms have greatly contributed to the rigor and quality of this dissertation. I express my sincere gratitude to Dr. Kieu for his invaluable service as a member of not only my defense committee but also my comprehensive exam committee. I also extend my thanks to Dal for providing guidance during my laboratory experiments.

I am grateful to my colleagues, Dr. Cheng Li, Adley Gin, Shuang Hao, Sand Suebka, Yisha Tang, Chang Ge and Yinchao Xu, who have provided stimulating discussions, thought-provoking insights, and a supportive academic community. Their intellectual engagement and encouragement have been a source of inspiration and motivation.

I am deeply appreciative of my family, parents, and friends for their unwavering support and belief in my abilities. Their love, understanding, and encouragement have been a driving force behind my perseverance in completing this dissertation. Their unwavering belief in my abilities and their constant encouragement have been the foundation of my academic pursuits.

Lastly, I would also like to express my sincere gratitude to the funding sources that have supported this research, including National Institutes of Health (NIH) R35GM137988 and National Science Foundation (NSF) 1842045. Their financial support has enabled me to pursue this study and has been vital in the completion of this dissertation.

In conclusion, I am deeply grateful to all those who have contributed to the completion of this dissertation. Their support, guidance, and encouragement have been invaluable, and I am honored to acknowledge their contributions.

DEDICATION

To my wife, Hyeonjung Baek, and my son, Sion Choi

TABLE OF CONTENTS

TABLE OF CONTENTS – *Continued*

LIST OF FIGURES

LIST OF FIGURES – *Continued*

LIST OF FIGURES – *Continued*

LIST OF FIGURES – *Continued*

LIST OF FIGURES – *Continued*

LIST OF FIGURES – *Continued*

LIST OF FIGURES – *Continued*

LIST OF FIGURES – *Continued*

LIST OF FIGURES – *Continued*

LIST OF FIGURES – *Continued*

ABSTRACT

The ability to detect individual molecules without the need for labels or capture probes is a topic of great interest in medical applications and scientific research. Frequency-locked microtoroid optical resonators have shown promise in label-free single molecule detection, but currently require prior knowledge of the molecule to be detected and surface functionalization of the cavity. Meanwhile, microresonator-based optical frequency combs have the potential to provide spectral information on molecules, but generating them in aqueous biological sensing environments has been challenging due to altered dispersion, coupling instability, and reduced quality factor of the resonator.

In this study, we propose a novel approach to achieve bio-sensing compatible spectroscopy by demonstrating the generation of frequency combs in both water and air at near-visible wavelengths, using a microtoroid optical resonator. Microtoroid resonators are well-suited for biosensing due to their high quality (Q) factors and small mode volumes. We achieve local anomalous dispersion by leveraging the interaction between different transverse mode families within an overall normal dispersion region, while preserving the advantageous structure and material of the microtoroid resonator for biosensing. Our approach can eliminate the need for labels or capture probes and has the potential to enable simultaneous detection and identification of single molecules in both air and liquid at any wavelength. By utilizing microresonator-based frequency combs to measure absorption spectra, we can detect binding events and identify molecular species on the same device, without the

need for additional structures or surface functionalization. This has the potential to significantly reduce experimental costs and save time.

Despite the advantages of this application, there have been no previous demonstrations of frequency comb generation in a biodetection setting where the resonator is covered with liquid. Conventional dispersion engineering techniques have not been effective in addressing the significant alteration of resonator dispersion caused by an aqueous solution. In this study, we generated an optical frequency comb based on a toroid resonator immersed in high-purity water, using an avoided mode crossing (AMX) approach. We also discuss technical challenges associated with this demonstration and present numerical solutions to overcome them.

Overall, our findings can pave the way for label-free single-molecule spectroscopy in aqueous environments using microtoroid resonators. We believe that this approach has promising potential for various biomedical and scientific applications. Further studies are warranted to explore the full potential of this approach in diverse sensing environments and applications.

CHAPTER 1

Fundamental Principles of Optical Microresonators

Research on optical microresonators has been ongoing for more than 20 years, and interest in this field continues to grow due to advances in micro/nano fabrication technologies. Optical microresonators offer unique and rich optical physics, and their potential applications in miniaturizing bulky optical systems and integrating them on a chip have significant implications, similar to electronics. In this chapter, basic concepts and background knowledge of optical microresonators is briefly reviewed, with a focus on silica microtoroid resonators, which are the subject of study in this thesis.

The basic principles of silica microtoroid resonators, including their optical modes and resonance frequencies, are discussed in this chapter. The fabrication techniques used to create these resonators are also described, including the use of lithography and etching processes.

1.1 Whispering-gallery-mode resonators

A whispering gallery mode (WGM) optical resonator is a type of optical cavity where light waves are confined and circulate along the circumference of the resonator via total internal reflection. The name "whispering gallery" comes from the effect that occurs in some circular or elliptical buildings, such as the whispering gallery in St. Paul's Cathedral in London, where a person standing at one end of the gallery can

hear a whisper from someone standing at the other end due to the reflection of sound waves.

Similarly, in a WGM optical resonator, light waves can be confined and "whispered" around the perimeter of the resonator due to the total internal reflection of the light waves. This results in a highly localized and long-lived optical field that can be used for a variety of applications, including sensing [2, 3, 4], filtering, and nonlinear optics. WGM resonators can be made from a variety of materials, including glass, silica, and polymers, and can have different shapes, such as spheres, disks, and toroids [5].

1.1.1 Resonance frequencies

The resonance frequencies of optical microresonators are evenly spaced and determined by the following equations:

$$\omega_m = \frac{2\pi m c}{n_{\text{eff}} L} \quad \text{or} \quad \lambda_m = \frac{n_{\text{eff}} L}{m} \tag{1.1}$$

In these equations, m represents the mode number, ω_m represents the angular frequency of the mth mode (λ_m represents the wavelength), n_{eff} represents the effective refractive index, L represents the roundtrip length of the resonator, and c represents the speed of light. The roundtrip time, t_R, is the inverse of the free-spectral range (FSR) of the resonator, which can be expressed as $t_R = 1/\text{FSR}$. It is important to note that the FSR is a frequency-dependent value that is influenced by the material and geometric dispersion of the medium.

1.1.2 Microresonator dispersion

The dispersion of a microresonator arises from both material dispersion, which describes the frequency dependence of the refractive index, and geometric dispersion, which is caused by the resonator's structure. This results in non-equidistant resonance frequencies and frequency-dependent mode spacings. The resonance frequency of an arbitrary mode with a relative mode number μ can be expressed as a Taylor series as following

$$\omega_\mu = \omega_0 + D_1\mu + \frac{1}{2!}D_2\mu^2 + \frac{1}{3!}D_3\mu^3 + ... \tag{1.2}$$

The equidistant frequency grid is represented by $D_1/2\pi$, and D_2 and D_3 describe the deviation of FSR from the center frequency in terms of second- and third-order dispersion, respectively. Positive (negative) D_2 coefficient represents anomalous (normal) dispersion, respectively. The deviation of the resonance frequencies from the equidistant frequency grids, also known as integrated dispersion D_{int}, can be expressed as

$$D_{\text{int}} = \omega_\mu - \omega_0 - D_1\mu = \frac{1}{2!}D_2\mu^2 + \frac{1}{3!}D_3\mu^3 + ... \tag{1.3}$$

In this thesis, we only focus on the second order dispersion coefficient and ignore the higher order dispersion coefficients. Dispersion is crucial for frequency comb generation, affecting its bandwidth and phase-matching condition. A detailed explanation of microresonator dispersion will be provided in chapter 2.

1.2 Silica microtoroid resonators

The whispering-gallery-mode resonator has become a significant platform in various fields of study, including nonlinear photonics and bio-detection, due to its ultra-high quality factor and small mode volume. About two decades ago, researchers developed the toroid resonator to address the surface roughness issues of the disk resonator [6]. The microtoroid resonator, in particular, has become one of the primary platforms for biosensing applications [7, 8], as the sensitivity of particle detection is proportional to the quality factor over the mode volume. Figure 1.1 depicts the schematic of the fabrication procedures for a toroid resonator. The process involves preparing a thermally grown silica layer on top of a silicon substrate, patterning disks using photolithography, followed by a buffered oxide etch (BOE) to remove the disks. The silicon layer is etched using XeF_2 gas to isolate optical modes from the silicon pillar. Finally, a CO_2 laser is used to heat and reflow the surface of the disks, forming a surface-induced structure. The results of the fabrication process are presented at the top of Figure 1.1.

A microscopic images for a microdisk and microtoroid resonators are shown in Figure 1.2. It's worth noting that as fabrication techniques have improved, using a CO_2 laser to reflow the disk layer is no longer advantageous or even desirable due to the high demand for integrating the resonator in a chip and precise geometrical design of the cavity structure [9, 10]. It is challenging to control the melting and reforming of the outer rim of the resonator with precision that can be easily achieved with current chip-based fabrication techniques. However, Despite the limited fabrication control, the toroid resonator's small mode volume and ultra-high

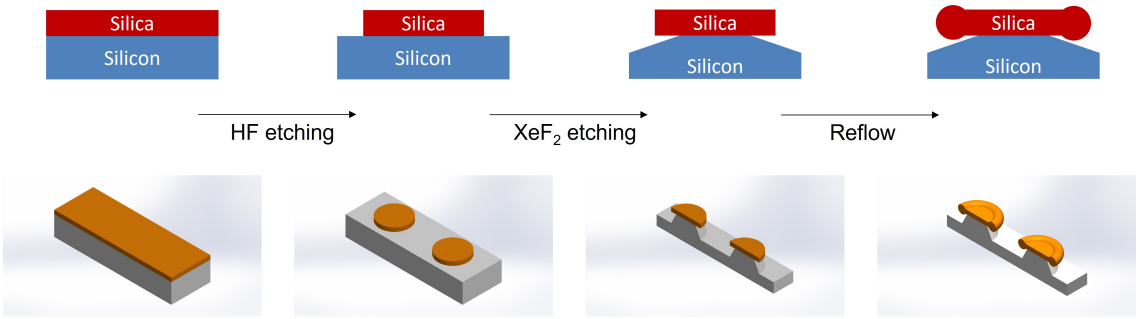

Figure 1.1: Fabrication procedures of silica microtoroids. (a) A thermally grown silica on top of a silicon substrate is prepared. A photoresist is applied, followed by patterning disks using photolithography on the photoresist layer. (b) The pattern is generated using HF wet etching. (c) XeF_2 dry etching is performed to undercut the silicon substrate. At this stage, this device is called microdisk resonator. (d) CO_2 laser is focused on the silica and melts silica to enhance surface roughness dramatically. A toroidal shape is generated due to surface tension.

quality factor are still attractive properties that are useful for various fields of study, including optomechanical photonics and single-particle detection.

1.2.1 Finite element analysis for optical eigenmodes

The finite element method (FEM) is used for eigenmode analysis of microresonators. In FEM, the microresonator is modeled as a three-dimensional structure consisting of various materials and shapes. The structure is discretized into small finite elements, each of which is described by a set of equations based on its material properties and geometry. These equations are then solved to obtain the electric and magnetic field distributions inside the microresonator.

Eigenmode analysis involves finding the modes of electromagnetic fields that satisfy the boundary conditions of the microresonator. These modes are known as eigenmodes, and they correspond to the standing waves that can exist inside the

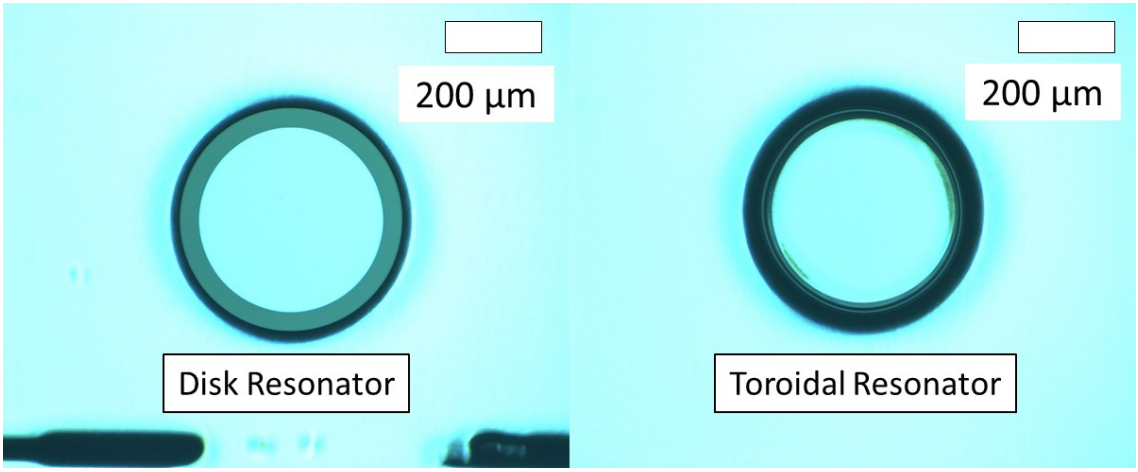

Figure 1.2: Microscopic images of silica microdisk resonator and microtoroid resonator. (Left) A diameter of a fabricated microdisk resonator is 700 μm. A CO_2 laser is focused to form a toroid resonator. (Right) A diameter of the toroid resonator is around 500 μm.

microresonator. Each eigenmode has a unique frequency and field distribution (figure 1.3).

1.3 Experimental setup

Figure 1.4 shows an experimental schematic for this experiment. A tunable laser is amplified and injected into the cavity using a tapered fiber. A photodetector (PD) is used to measure the intensity of the light that is transmitted through the microresonator. This can be used to monitor the resonance characteristics of the microresonator over time. A scanning of the laser is calibrated by a Mach-Zehnder interferometer (MZI). A high sampling rate data acquisition (DAQ) card or an oscilloscope monitors both the MZI and transmission signal. An optical spectrum analyzer (OSA) is used to measure the optical spectrum of the light that is transmitted through the microresonator. The microresonator is typically sensitive to

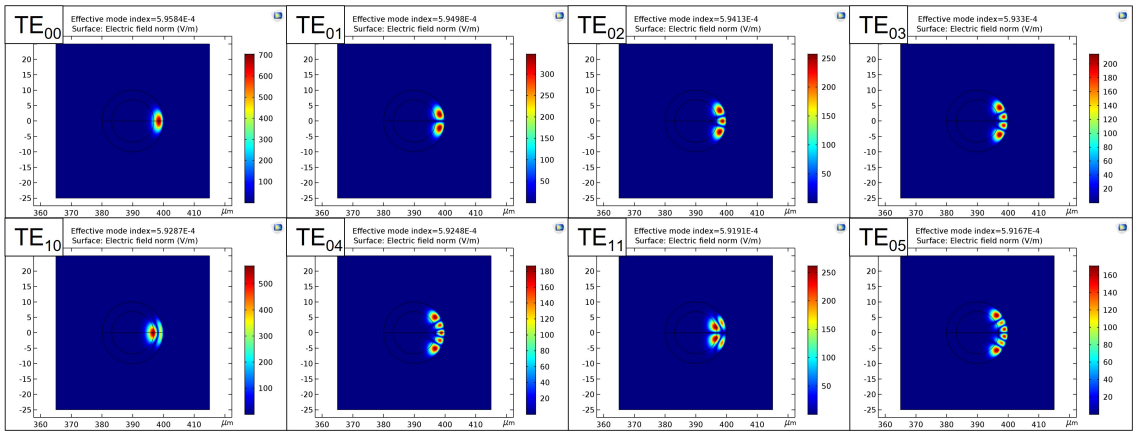

Figure 1.3: Eigenmode analysis for a microtoroid resonator. Representative mode profiles for 8 optical modes are labeled with their orders of modes as TE_{ij}, where i represents the radial mode number and j represents the azimuthal mode number.

temperature fluctuations, so a thermo-electric cooler is often used to maintain a stable operating temperature. The experimental setup is shown in figure 1.5.

1.4 Coupling light into microresonators

There are several methods available to achieve the coupling of light into an optical microcavity. One such method involves using a prism to couple light into a microcavity. The prism is positioned near the microresonator, and laser light is focused onto a spot close to it. Total internal reflection within the prism occurs, allowing the evanescent tail of the light wave to couple into the resonator and vice versa.he angle of incidence is adjusted to match the resonant wavelength of the resonator. A similar method involves using angle-cleaved fibers. This technique requires two fibers for coupling, which increases the degrees of freedom for proper positioning of the fibers.

In this work we use tapered fiber coupling which has several advantages over

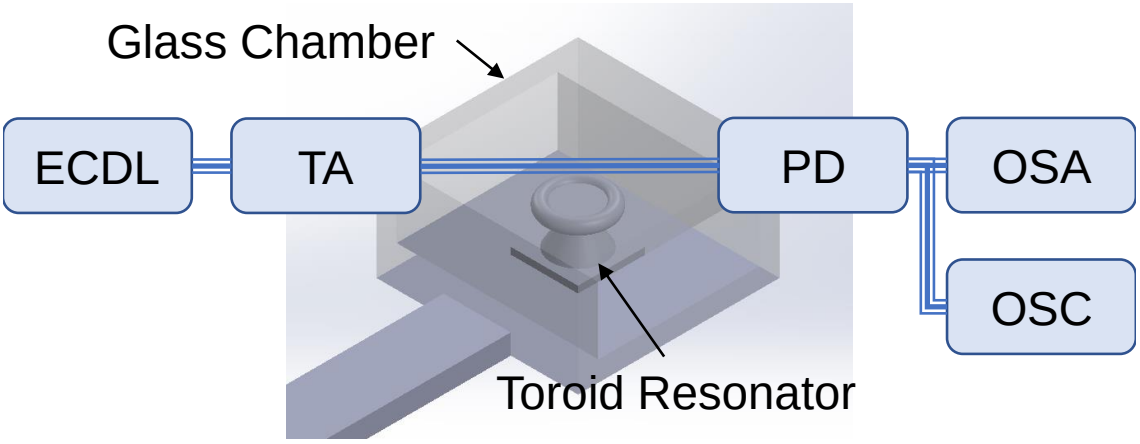

Figure 1.4: Simplified experimental setup for device characterization and measurement. ECDL: external cavity laser diode; TA: tapered amplifier; PD: photodiode; OSA: optical spectrum analyzer. OSC: oscilloscope

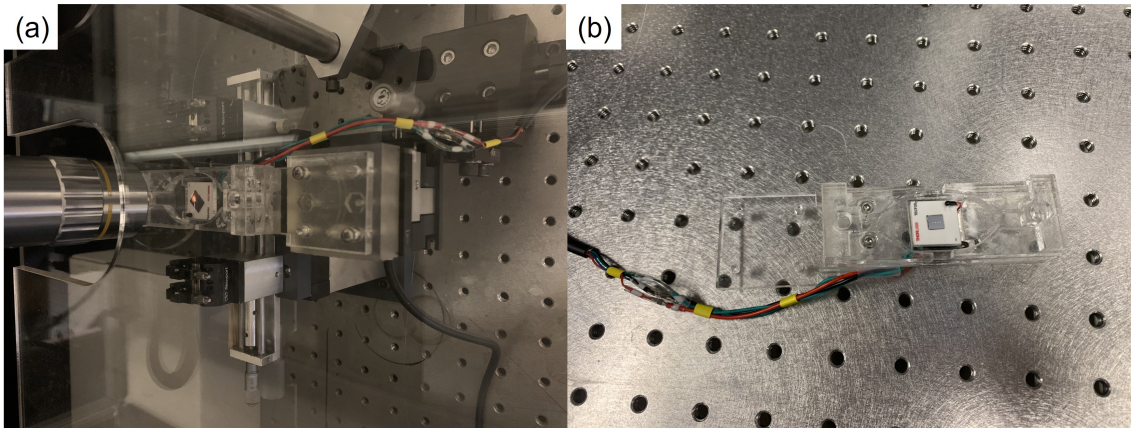

Figure 1.5: Experimental setup. (a) An optical microresonator is mounted on a nano-positioning stage that allows it to be precisely aligned with the tapered fiber. The microresonator is imaged with a microscope to monitor the alignment. (b) The optical microresonator is placed on a thermo-electric cooler (TEC) attached on a custom-built sample holder. The TEC is used to reduce a thermal fluctuation in the surrounding environment.

other coupling techniques. These advantages include high coupling efficiency, low insertion loss, easy alignment, a wide range of wavelengths, and a compact size. The tapered fiber can be precisely fabricated to match the mode of the resonator, which leads to efficient coupling, and it can be used over a broad range of frequencies. Tapered fiber coupling is a simple and easy technique to align, requiring only a single fiber, which makes it suitable for applications where space is limited.

1.4.1 Fabrication of optical tapered fiber

The fabrication of an optical tapered fiber generally entails utilizing the fiber pulling technique, which involves heating and elongating a fiber until it thins out at the heated section. A standard single-mode optical fiber is used as the starting material, which is initially cleaned using isopropyl alcohol and a lint-free cloth to remove any impurities that may hinder the tapering process. Next, the fiber is secured within a fiber pulling apparatus, comprising a heat source, fiber holder, and stretching mechanism. The heat source is directed at a specific area of the fiber, typically a few millimeters in length, with a uniform and stable heating region desired as shown in Figure 1.6. While gradually elongating the fiber using the stretching mechanism, heat continues to be applied cautiously to prevent breakage.

Throughout the process, the fiber diameter or transmitted light power after the tapered fiber region is monitored. As the fiber diameter decreases, interference between multi-modes within the tapered fiber leads to oscillation at the output power. When the oscillation vanishes, the tapering process stops, and the tapered fiber converts back to a single-mode fiber. It is important to note that the tapered fiber guides light via the air-silica boundary.

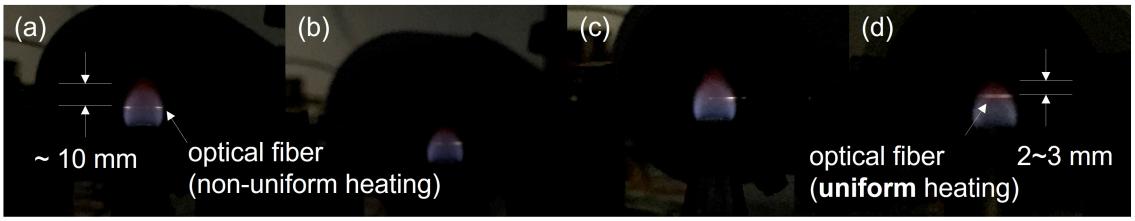

Figure 1.6: Heating an optical fiber with a hydrogen flame. The heating region of the fiber is observed at various positions. The distance between the top of the flame and the fiber is adjusted to 10 mm (a), 7 mm (b), 5 mm (c), and 3 mm (d). When the distance is around 10 mm (a), only the ends of the heating region of the fiber are illuminated (or heated), resulting in a fabrication failure. On the other hand, at a distance of approximately 2 mm (d), the heating region of the optical fiber is uniformly bright.

Theoretical description

The simplest possible model of coupling to and from a microresonator can be described by a single mode of the waveguide and a single-cavity mode. The resonant excitation of the internal cavity field is given by the equation:

$$\frac{da}{dt} = -\frac{1}{2}(\kappa_0^2 + \sigma_0^2)a + i\kappa_0 s \tag{1.4}$$

where a represents the energy amplitude in the resonator. The total energy amplitude loss rate of the cavity is determined by the first term, which accounts for contributions from the intrinsic resonator loss σ_0 and external coupling κ_0. The last term describes the excitation of the resonator by the waveguide with coupling coefficient κ_0, where s is the power normalized with waveguide field. The phase of this term reflects a $\pi/2$ phase shift upon coupling between the cavity and waveguide. This equation applies when the internal losses and external coupling are small enough to be treated independently, which is satisfied for the low-loss resonators

investigated in this thesis.

The waveguide transmission is given by the interference between the optical power not coupled into the resonator ($t_0 \approx s$) and the amount coupled out of the cavity ($e^{\pi/2}\kappa_0 a$). Under the steady-state excitation condition for equation (1.4), the transmission can be given by

$$T = |t_0/s + i\kappa_0 a/s|^2 = \left(\frac{1-K}{1+K}\right)^2 \tag{1.5}$$

where $K = \kappa_0^2/\sigma_0^2$ is a dimensionless parameter, known as ideality. In this analysis, the coupling parameter K is introduced as the ratio of coupling between the waveguide and resonator to intrinsic resonator loss. This parameter allows a simple way to investigate the coupling regimes and properties of the system. There are three coupling regimes that are commonly used to describe the coupling between a waveguide and a microresonator: undercoupling, critical coupling, and overcoupling.

Undercoupling occurs when the coupling between the waveguide and the microresonator is weaker than the intrinsic loss of the microresonator ($K < 1$ or $\kappa_0 < \sigma_0$). For a highly undercoupled regime ($K \ll 1$), most of the light in the waveguide does not couple into the microresonator and the transmission through the waveguide in this regime is high, close to unity, and the circulating power inside the microresonator is low. However, as power is coupled into the cavity, there is a transmission drop.

Critical-coupling is the point where the coupling coefficient is equal to the intrinsic loss of the resonator ($K = 1$ or $\kappa_0 = \sigma_0$). At this point, the input light is perfectly coupled into the resonator, and the waveguide transmission drops to zero.

The circulating power inside the resonator is at a maximum, which means that all the input light is trapped inside the resonator.

Overcoupled regime occurs when the coupling coefficient is greater than the intrinsic loss of the resonator ($K > 1$ or $\kappa_0 > \sigma_0$). In this regime, the waveguide transmission increases, and the circulating power inside the resonator decreases. The output coupling dominates the cavity loss, resulting in a π phase-shift of the waveguide field.

When two multimode waveguides or resonators are coupled, there will typically be cross-coupling between all available optical guided and radiation modes. To account for the effect of output coupling to additional optical modes, the equation for the internal energy amplitude decay rate can be modified by adding loss terms for higher-order waveguide modes ($\kappa_{i>0}$) to equation (1.4). This modification results in a generalized ideality expressed as

$$K = \frac{\kappa_0^2}{\sum_{i\neq 0} \kappa_i^2 + \sigma_0^2} \tag{1.6}$$

The ideality of a system can be precisely measured experimentally by examining the waveguide transmission, which is obtained by varying the distance, x, between the waveguide and resonator. As the coupling amplitudes decrease exponentially with the distance the coupling amplitude can be expressed as $\kappa^2 = \overline{\kappa}^2 e^{-\gamma_0 x}$ where γ is spatial decay rate. Assuming a single higher-order waveguide mode is a dominant source of coupling loss, the generalized ideality can provide the information on additional losses in the coupling regime as follows

$$K = \frac{\bar{\kappa}_0^2 e^{-\gamma_0 x}}{\bar{\kappa}_i^2 e^{-\gamma_i x} + \sigma_0^2} = \left(\frac{1 \pm \sqrt{T}}{1 \mp \sqrt{T}} \right) \tag{1.7}$$

Figure 1.7 illustrates the calculated coupling ideality under different coupling conditions using equations (1.4) and (1.7). To experimentally measure the transmission of a resonance, one can vary the separation between the tapered fiber and the microresonator, resulting in different behaviors depending on the phase-matching conditions or tapered fiber diameters. Under ideal phase-matching conditions, energy can be efficiently transferred from the fiber's single mode to the resonator's single mode. However, any phase-mismatch may cause higher order mode coupling loss. To stabilize the system, it is often desired to have the resonator and tapered fiber in contact, although this may require introducing some higher order mode coupling loss to achieve a significant amount of light coupling into the resonator.

1.4.2 Experimental observation of coupling ideality

Two different cases for coupling ideality are discussed: a high and low coupling ideality. For a high coupling ideality case, the most of the light in the waveguide is transferred into the single mode in the microresonator. All of three coupling regimes (under, critical, and over coupling) can be accessed by varying the separation between the tapered fiber and the microresonator. This happens when the phases of the light in the fiber and the resonator are aligned (or wave-vectors of them are the same). Figure 1.8 shows the experimental observation on this condition. When the separation between the fiber and resonator are decreases, a resonance is observed. The transmission increases as the distance gets closer. However, at a

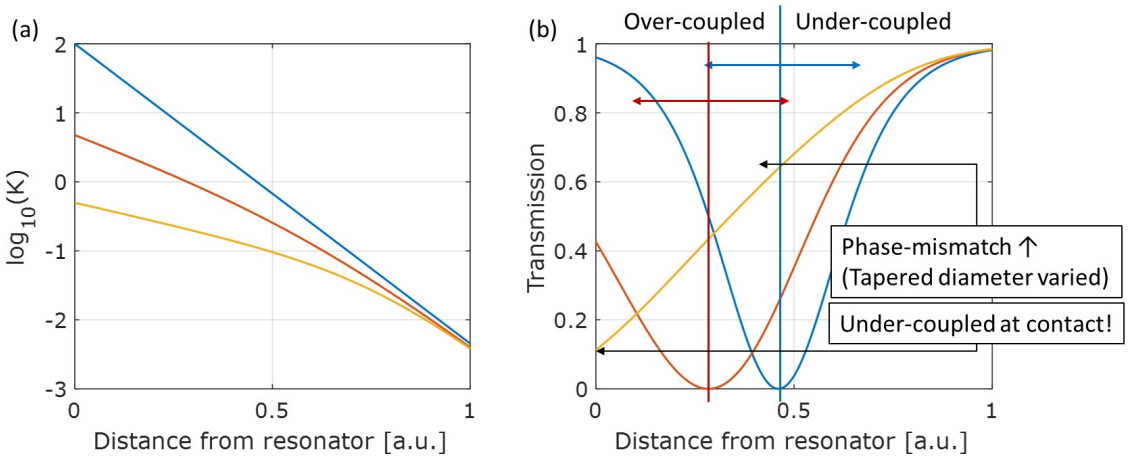

Figure 1.7: Coupling ideality and corresponding transmission. (a) K versus position for various taper diameters (or phase matching conditions) from equation (1.7). Coupling amplitude for the higher order mode (κ_i) are set to zero (blue), low (red), high (yellow). As the distance get smaller, the ideality get larger. The maximum ideality ($x = 0$) decreases as the higher-order coupling loss increase. (b) The corresponding tranmssion through a waveguide as a function of the separation distance. When the higher-order coupling is zero (blue) or small (red), it is shown that all the coupling regimes can be accessed by simply varying the distance. However, as the higher-order coupling is high (yellow), only undercoupled regime can be accessed.

certain distance, the transmission is maximized, then it starts to decrease as the distance gets even closer. And finally the transmission is minimized when they are in contact. Also refer the blue line in figure 1.7.

As discussed earlier in this section, in the case of low coupling ideality, there will be more than one coupling mechanisms between the waveguide and resonator: coupling from the single mode in the resonator to the single mode and higher order mode in the tapered fiber. This happens when the phases of the light in the fiber and the resonator are mis-aligned (or wave-vectors of them are not the same). Typically, only the under-coupled regime can be accessed in this case. When the distance between the fiber and resonator is 0.5 μm, a resonance is excited. As the distance decreases, the transmission increases and reaches a maximum when they are in contact, as indicated by the yellow line in figure 1.9. This condition is often desirable as it ensures stable coupling, making it advantageous to excite a resonance in the in-contact position.

1.5 Q-factor characterization

The Q factor, or quality factor, of an optical resonator is a measure of how well the resonator can store and sustain light within it. It is defined as the ratio of the energy stored in the resonator to the energy lost per optical cycle. In other words, it quantifies the number of oscillations a resonator can undergo before its stored energy is lost due to factors such as scattering, absorption, and transmission.

The Q factor is a crucial parameter for optical resonators, with higher Q factors indicating narrower resonance linewidths and better light storage capabilities. Two methods to measure Q factor are the ring-down method, which measures the decay

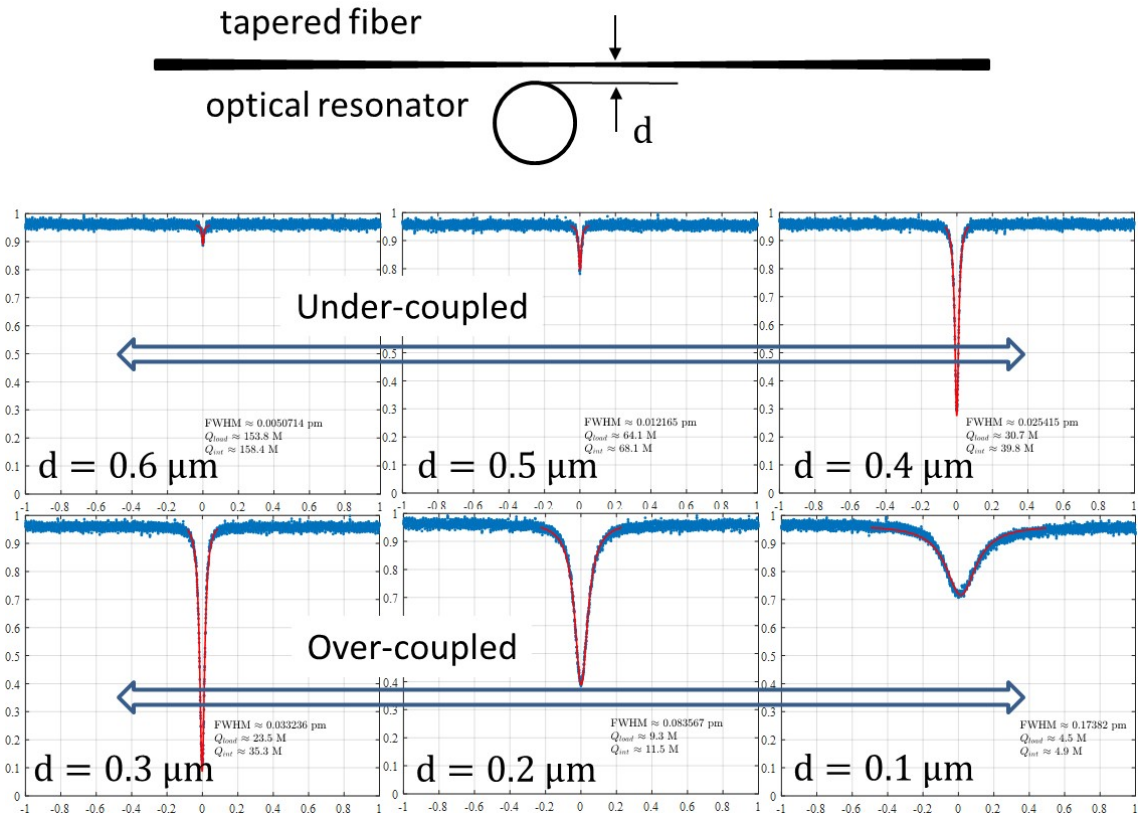

Figure 1.8: Observation of high coupling ideality in experiment. The separation between the tapered fiber and microresonator, d, was varied and the corresponding resonances were observed. At $d = 0.6$ μm, the light began to couple from the fiber to the resonator, referred to as the under-coupled regime. The coupling increased as d decreased and reached a maximum at $d \approx 0.3$ μm, known as the critical coupling regime. However, as the distance decreased further, the transmission decreased again, referred to as the over-coupling regime. When the fiber and resonator were in contact, the transmission dropped to zero (not shown in this figure).

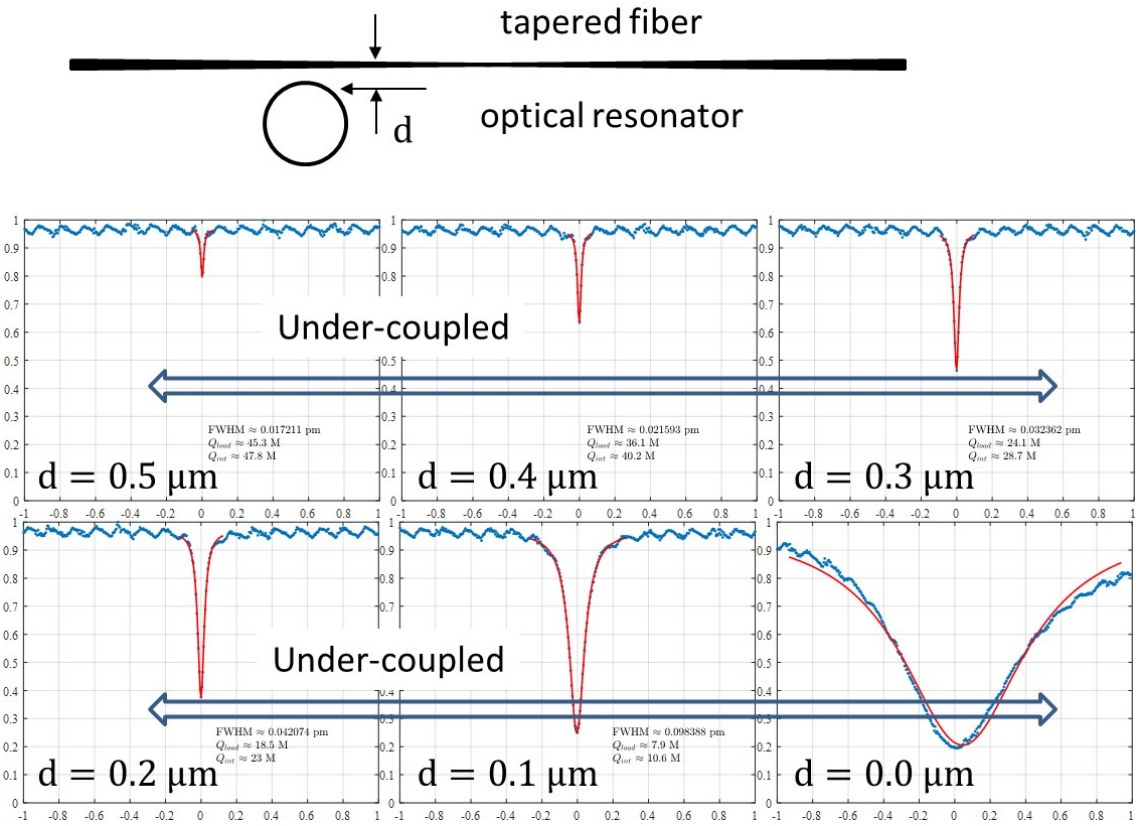

Figure 1.9: Observation of low coupling ideality in experiment. The tapered fiber diameter is increased compared to the high coupling ideality case. The separation between the tapered fiber and microresonator, d, was varied and the corresponding resonances were observed. At $d = 0.5$ μm, the light began to couple from the fiber to the resonator, referred to as the under-coupled regime. The coupling increased as d decreased and reached a maximum in contact. The critical and over coupling regimes were not able to be accessed under this condition. Undesired coupling losses can occur, but in cases where resonance excitation in the in-contact position is preferred, such losses can actually be allowed.

of light intensity over time after initial excitation with a pulse of light, and the frequency scanning method, which involves scanning a continuous wave laser across a resonance and fitting the resulting resonance curve to determine the Q factor. In this work, only the frequency scanning method is used to characterize the Q factor.

The width of the resonance curve at the half-maximum point provides information about the Q factor of the resonator. Specifically, the Q factor is related to the resonance linewidth by the formula:

$$Q_{\text{load}} = \frac{\lambda}{\Delta\lambda} = \frac{\omega}{\Delta\omega} \tag{1.8}$$

where $\lambda(\omega)$ is the resonant wavelength (frequency), $\Delta\lambda(\Delta\omega)$ is the full width at half maximum of the resonance curve in wavelength (frequency), and the Q_{load} is measured Q factor and given by

$$\frac{1}{Q_{\text{load}}} = \frac{1}{Q_{\text{int}}} + \frac{1}{Q_{\text{ext}}} \tag{1.9}$$

where Q_{int} is the intrinsic Q factor and Q_{ext} is the extrinsic Q factor. The intrinsic Q-factor measures the energy lost per cycle within the resonator material, while the extrinsic Q-factor measures the energy lost per cycle due to coupling between the resonator and its surroundings. The total Q-factor is the inverse sum of the inverse intrinsic and extrinsic Q-factors and is limited by the lower of the two Q-factors. The expression for the intrinsic Q factor can expressed as

$$Q_{\text{int}} = \frac{2}{1 \pm \sqrt{T}} Q_{\text{load}} \tag{1.10}$$

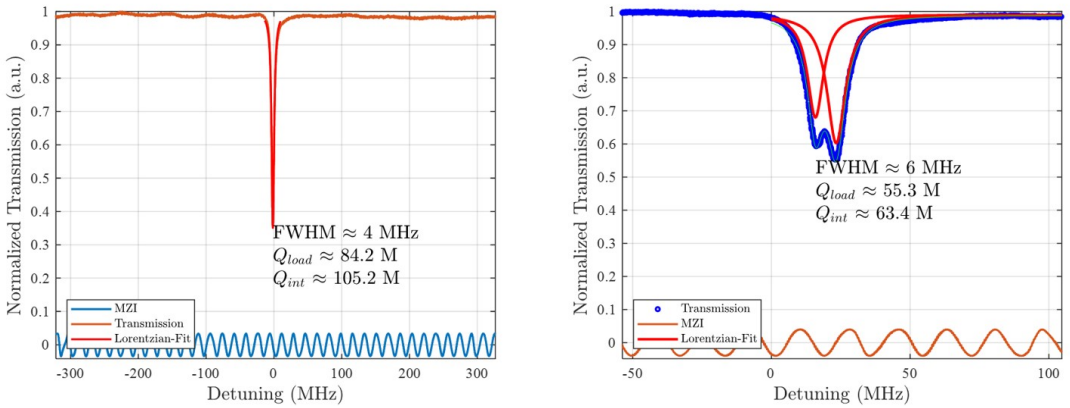

Figure 1.10: Q factor measurement. A continuous wave laser is used to excite the resonator, and the wavelength of the laser is swept across a resonance of the resonator. The resulting intensity of the transmitted or reflected light is recorded as a function of the laser's wavelength. This produces a resonance curve that shows the intensity of the light as a function of the laser's wavelength, with a dip corresponding to the resonance frequency of the optical resonator. The laser's wavelength is calibrated with a fiber-based Mach-Zehnder interferometer (MZI), shown as sinusoidal oscillations. By fitting a single (Left) or double (Right) lorentzian curve the loaded q factor is measured.

where the sign expresses under coupling (+) and over coupling (−). From the measured transmission spectrum, the intrinsic and coupling Q factors can be determined using the above equation. Figure 1.10 shows a representative measurement of the Q factor in experiments.

The fundamental optical mode is typically distinguished by its narrow resonance linewidth and high quality factor, and can be identified by its unique spectral characteristics, such as the mode spacing (or free spectral range) or the largest evanescent tail. The mode structure of the microresonator can be analyzed by examining the transmission spectrum and identifying the resonant peaks corresponding to the different optical modes. In experimental setups, the fundamental mode can be

identified using the following technique: Initially, a thick part of a tapered fiber is brought into contact with the microresonator where no optical mode coupling is observed. Subsequently, the diameter of the tapered fiber is gradually decreased until the coupling of the optical mode with the largest evanescent tail is observed, which corresponds to the fundamental mode.

1.6 Thermal resonance shift

When a low power probe laser is scanned over a resonance of a microresonator, a Lorentzian resonance dip can be observed in the transmission through the coupling waveguide. On the other hand, if the same experiment is repeated with a high power pump laser, an almost triangular resonance shape, known as the 'thermal triangle', can be observed when the scan is performed in the direction of decreasing optical frequency.

The thermal frequency shift in an optical microresonator is influenced by several factors, including the intracavity power. The intracavity power refers to the power of the light circulating within the microresonator. In general, the thermal frequency shift is proportional to the intracavity power. This is because the intracavity power can generate heat within the microresonator, which can cause thermal expansion and affect the resonant frequency. As the intracavity power increases, the amount of heat generated also increases, leading to a larger thermal frequency shift.

Figure 1.11 shows examples of the thermal resonance shift. When the wavelength scans from small to large wavelengths, the intracavity power increases and the resonance wavelength shifts to longer wavelengths. Then, the resonance is broadened and a 'thermal triangle' can be observed. When the scan is performed slowly

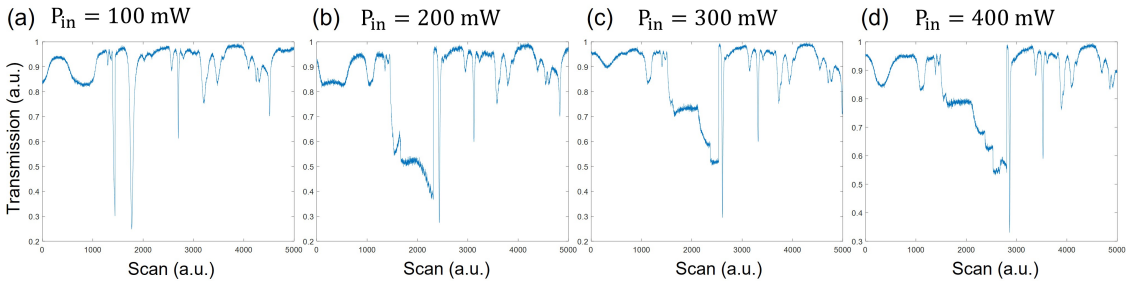

Figure 1.11: Thermal resonance shift at various pump powers. The 'thermal triangle' gets bigger as the pump power increases. The total width of the resonance is proportional to the pump power. The same resonance is shown with different input pump power 100 mW (a), 200 mW (b), 300 mW (c), and 400 mW (d). It can be also observed that the two adjacent resonances couple together as the thermal triangle gets broader.

enough compared to the thermal time constants of the system, the resonator can be considered thermally locked to the resonator.

1.6.1 Q-factor and thermal triangle at various coupling conditions

In figure 1.12, the resonance of the microresonator when the fiber is in contact at the equatorial plane is shown with varying tapered fiber diameter. And the corresponding resonance measurements are shown. At positions 1 and 2, a narrow resonance with an observable thermal triangle is present, but with low transmission and intracavity power. As the tapered diameter increases, additional losses in the coupling region cause the resonance to become broader.

Figure 1.13 displays the same resonance when the tapered fiber heights are varied while the tapered diameter is fixed. The fiber and the resonator are in-contact. The coupling height variation can change the coupling regime and measured Q factor. At a height of y = 4 μm, the transmission is at its maximum, and the loaded Q

factor is high, with an observable thermal triangle. In experiments, this coupling condition is preferred for maximizing intracavity power.

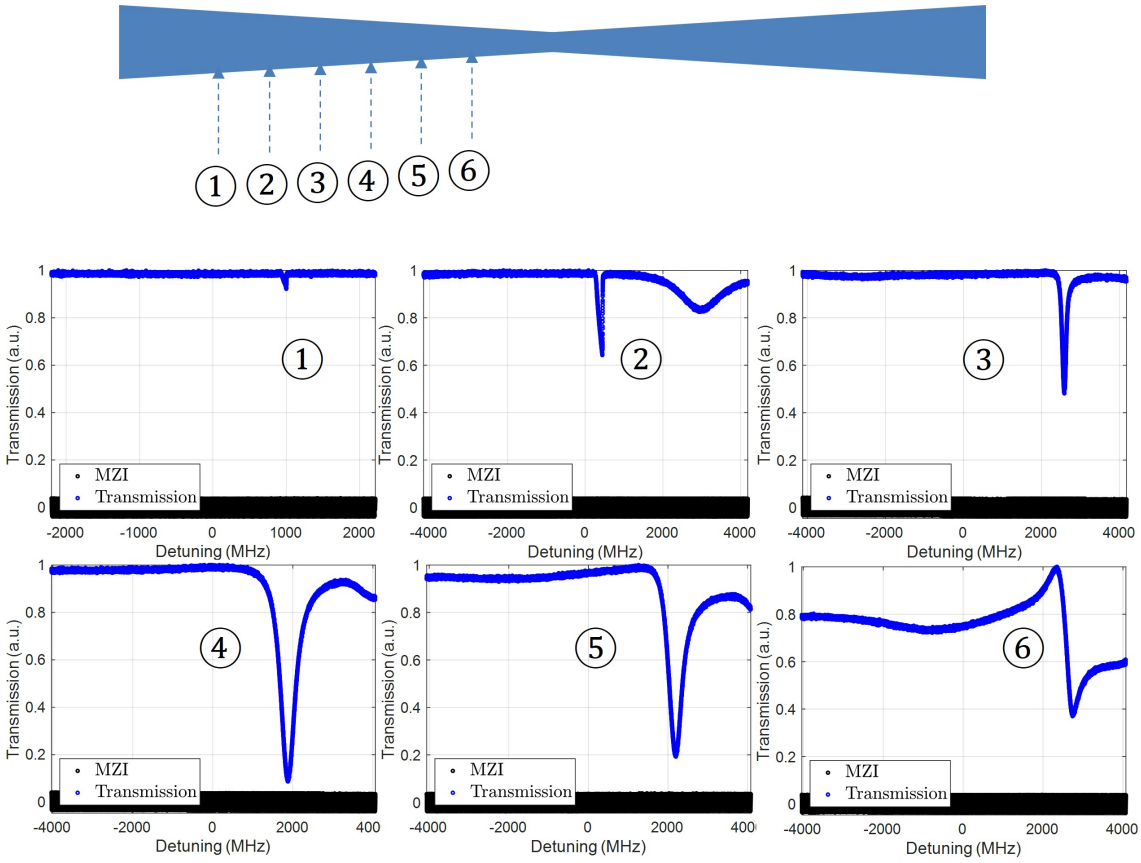

Figure 1.12: Measured resonances with various tapered fiber diameters at the equatorial plane between the fiber and the microresonator. The resonacne is undercoupled at position 1, 2, and 3. The resonance is close to critical-coupled at position 4. The resonance is close to over-coupled at position 5 and 6. The measured Q factor is higher at position 1 and 2 and the thermal triangle is observed . The measured Q factor decreases as the tapered diameter decreases.

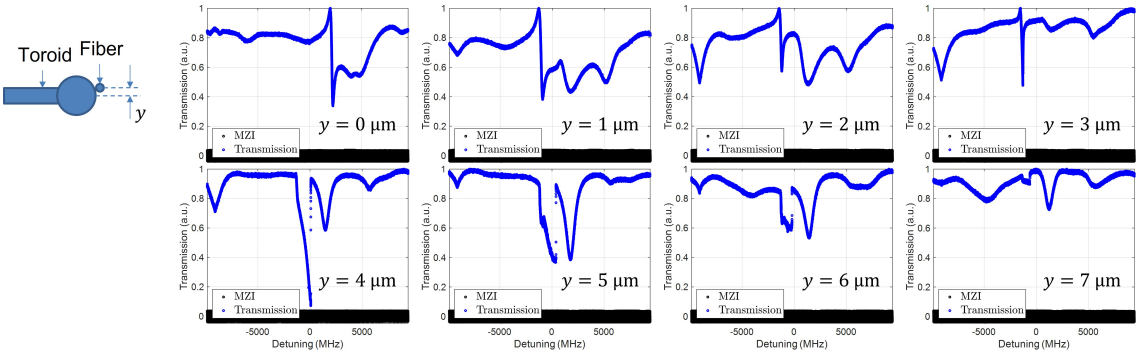

Figure 1.13: Measured resonances with various tapered fiber heights, y, from the equatorial plane of the microresonator (inset). The resonacne is over-coupled at y = 0, 1, 2, and 3 μm. The resonance is close to critical-coupled at y = 4 μm. The resonance is close to under-coupled at y = 5, 6, and 7 μm. The measured Q factor is higher at under- and critical-coupled regimes and the thermal triangle is observed. A high transmission and measured Q factor are observed at y = 4 μm.

CHAPTER 2

Microresonator-Based Nonlinear Optics

Microresonator-based optical frequency comb generation has several advantages over other frequency comb techniques. These include small size, low power consumption, wide spectral range, high repetition rates, compatibility with other systems, and lower cost. However, microresonator-based frequency comb systems also have some disadvantages, such as difficulty in tuning the comb line spacing, thermal fluctuations and mechanical vibrations affecting the comb line stability, and nonlinear processes causing unwanted noise and crosstalk.

Despite these challenges, microresonator-based frequency comb systems are gaining popularity due to their unique advantages and the potential for further development. Ongoing research is focused on improving the stability and precision of the system, exploring new materials and fabrication techniques for the microresonators, and optimizing the system for specific applications. In comparison to other frequency comb techniques, such as mode-locked lasers and supercontinuum sources, microresonator-based frequency combs offer a distinct set of advantages.

Mode-locked lasers are widely used for frequency comb generation but are bulky, complex, and require a high level of expertise to operate. Supercontinuum sources, on the other hand, are compact and can generate a broad spectral range, but they lack the high repetition rates of microresonator-based frequency combs. Overall, microresonator-based optical frequency comb generation is a promising technique

with potential for various applications, including spectroscopy, metrology, and communication systems. As research in this field continues, the performance and capabilities of the technology are likely to improve, further expanding its potential applications.

2.1 Optical nonlinear process: four-wave mixing (FWM)

The response of a nonlinear medium to an electromagnetic wave typically describes nonlinear optical effects. This response is characterized by the dielectric polarization P, which can be expressed as a power series expansion of the electrical field E.

$$P = \epsilon_0 \chi^{(1)} E + \epsilon_0 \chi^{(2)} E^2 + \epsilon_0 \chi^{(3)} E^3 + ... \tag{2.1}$$

where ϵ_0 is the vacuum permittivity and $\chi^{(n)}$ is the n-th order electrical susceptibility. The second order nonlinearity term $\chi^{(2)}$ vanishes in silica due to inversion symmetry, allowing for an approximation of the dielectric polarization in four-wave mixing as following

$$P = \epsilon_0 \chi^{(1)} E + \epsilon_0 \chi^{(3)} E^3 \tag{2.2}$$

where $P_L = \epsilon_0 \chi^{(1)} E$ represents linear induced polarization and $P_{NL} = \epsilon_0 \chi^{(3)} E^3$ denotes nonlinear induced polarization. The nonlinearity term $\chi^{(3)}$, known as the parametric Kerr nonlinearity, plays a significant role in self- and cross-phase modulation, as well as parametric frequency conversion processes. When the electric fields with three different frequencies $(\omega_k, \omega_l, \omega_m)$ and corresponding wave-vectors (k_k, k_l, k_m) are introduced, the nonlinear polarization P_{NL} contribution for the four-

wave mixing process can lead to generation of waves with new frequencies given by $\omega_n = \pm\omega_k \pm \omega_l \pm \omega_m$.

The process responsible for generating frequency combs in microresonators is FWM which can be classified into two types: degenerate and nondegenerate. Degenerate FWM occurs when two of the three input waves are at the same frequency, and the third input wave is at a different frequency. Nondegenerate FWM involves the mixing of three input waves at different frequencies in a nonlinear medium inside the resonator to produce a fourth output wave at a new frequency. In terms of photons, FWM can be interpreted as the annihilation of two photons. In the case of degenerate FWM, two photons with the same frequency $\omega_k = \omega_m$ are annihilated, and two photons with respective frequencies ω_l and ω_n are created, where $2\omega_k = \omega_l + \omega_n$. In the non-degenerate case, two photons with different frequencies ω_k and ω_l are destroyed, and two photons with frequencies ω_m and ω_n are created, conserving energy such that $\omega_k + \omega_l = \omega_m + \omega_n$. These processes require the phase-matching conditions as

$$k_n = k_k - k_l + k_m \qquad (\text{non} - \text{degenerate})$$

$$k_n = 2k_k - k_l \qquad (\text{degenerate})$$

Dispersion requirement for FWM process

There are two types of dispersion that can occur in microresonators. Normal dispersion occurs when the refractive index increases with increasing wavelength, while anomalous dispersion occurs when the refractive index decreases with increasing

wavelength. The dispersion of the microresonator consist of three main contributions: material dispersion, waveguide (or geometrical) dispersion, and modal dispersion. The Material dispersion refers to the variation in the refractive index of a material with respect to the wavelength of light. This can cause different wavelengths of light to travel at different speeds in the material, which can lead to dispersion and distortion of the signal. The waveguide dispersion arises due to the geometrical structure of the resonator. The modal dispersion refers to the variation in the propagation delay of different modes of light in a waveguide or a resonator. This can occur when the waveguide or the resonator has a geometrical structure that supports multiple modes of light with different phase velocities. Material dispersion is typically the dominant source of dispersion in many microresonators, while geometrical and modal dispersion can also contribute.

The dispersion requirement for FWM in an optical resonator varies depending on the specific application, such as parametric amplification or frequency comb generation. The frequency comb generation requires an anomalous dispersion in the optical resonator. Anomalous dispersion helps in effectively phase-matching the different optical frequencies involved in the FWM process, leading to efficient mixing and high conversion efficiency. Also note that the quality factor of the resonator, the nonlinearity of the medium, and the power levels of the interacting waves are also crucial factors that determine the efficiency and performance of FWM in the optical resonator. In the following subsection, it will be shown that the dispersion of microresonators can be engineered to satisfy the dispersion requirement.

2.1.1 Dispersion engineering on silica microbubble resonators

It is demonstrated that engineering geometry of a microbubble resonator can yield anomalous dispersion at near-IR wavelength ($\sim$ 780 nm) [11]. A microbubble resonator with around 1 micrometer wall thickness was fabricated and the optical frequency comb was able to be observed (Figure 2.1). As a thickness of a microbubble resonator gets thinner, the light gets confined tighter in the waveguide and compensate the material dispersion. However, this demonstration is performed in air and injecting liquid into or over the resonator can degrade the confinement, resulting in normal dispersion at near-IR wavelength ($\sim$ 780 nm). Figure 2.2 shows second order dispersion parameters of a silica microbubble resonator with a diameter of 120 µm and thickness of 1.5 µm for given boundary conditions. It can be clearly observed that as the surrounding material is replaced by liquid from air anomalous dispersion ($D_2 > 0$) at$\sim$ 780 nm cannot be achieved. In the next section, alternative methods for frequency comb generation will be discussed.

Fabrication techniques

Optical microbubble resonators can be fabricated through the following steps. First, prepare a fused silica glass capillary with a diameter of a few hundred micrometers and a length of a few centimeters. The capillary is heated with a CO_2 laser or a gas torch, and the glass is softened to form a bubble at the heating point. A gas flow is introduced into the softended region of the capillary, causing the softened glass to inflate and form a microbubble. The diameter and wall thichkness of microbuble resonators can be fine-controlled with the capillary size, CO_2 laser power, heating

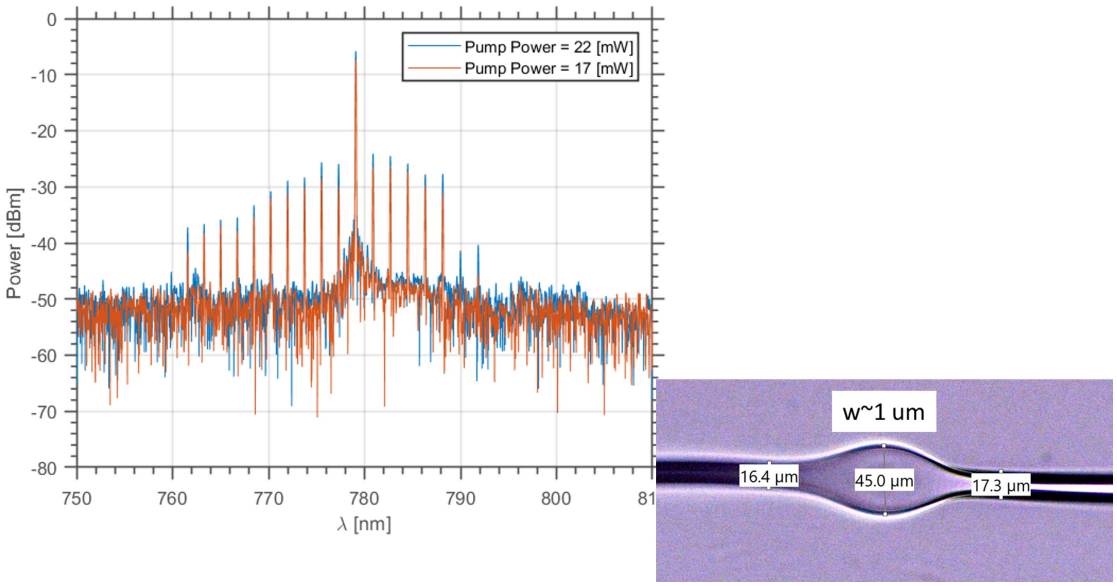

Figure 2.1: By engineering the geometry of the microbubble resonator, optical frequency comb generation at 780 nm is achieved. The resonator's design produces anomalous dispersion, as depicted in the inset image. The tightly confined light can counteract the normal dispersion of the silica and initiate the four-wave mixing (FWM) process. Increasing the pump power can generate additional frequency components.

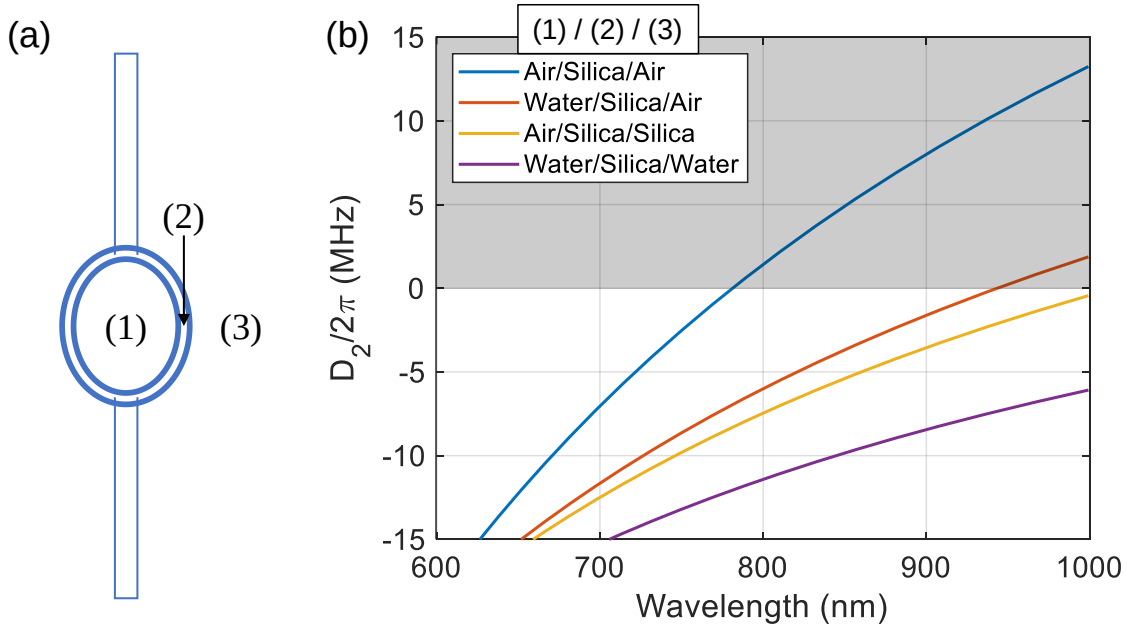

Figure 2.2: Finite element simulation on a microbubble resonator. (a) Geometry of a microbubble resonator. Inside (1) and outside (3) of the resonator can be air or liquid. Silica is chosen for material of the resonator (2). (b) Simulated second order dispersion parameters at various wavelengths. A diameter of a microbubble resonator is 120 µm and thickness of a wall is 1.5 µm in the simulation.

time, and gas pressure. Fabricating a thin-walled microbubble resonator is a key requirement for the FWM process to be initiated. We use CO_2 laser with double-sided heating technique for uniform heating (Figure 2.3). Note that non-uniform heating leads to asymmetric microbubble shape and fabrication failure.

2.2 Avoided mode crossing (AMX)

In an optical resonator, there can be multiple resonant modes with slightly different frequencies. When the frequency separation between two modes becomes small, they can interact with each other and cause a phenomenon known as avoided mode crossing (AMX). At the point of mode interaction, the modes exchange energy, and their frequencies shift. This can result in an unexpected change in the resonator's spectral properties, such as a splitting or broadening of the resonance peak. AMX occurs due to the complex interplay between the resonator's geometry, material properties, and the excitation conditions.

AMX can cause unwanted effects in some applications, such as in optical filters, where the modes can interfere with each other and cause signal distortion. However, in some cases, AMX can be desirable, such as in mode-locked lasers or optical frequency combs, where the crossing can lead to the formation of new frequencies. Understanding and controlling mode crossing is an important aspect of designing and optimizing optical resonators for specific applications.

By virtue of this technique, regardless of the overall dispersion of a mode family at a particular wavelength, the four-wave mixing (FWM) process can still be initiated. In a resonator, different optical modes have their own free spectral ranges (FSRs) that can intersect or couple, causing deviations in FSRs. This localized

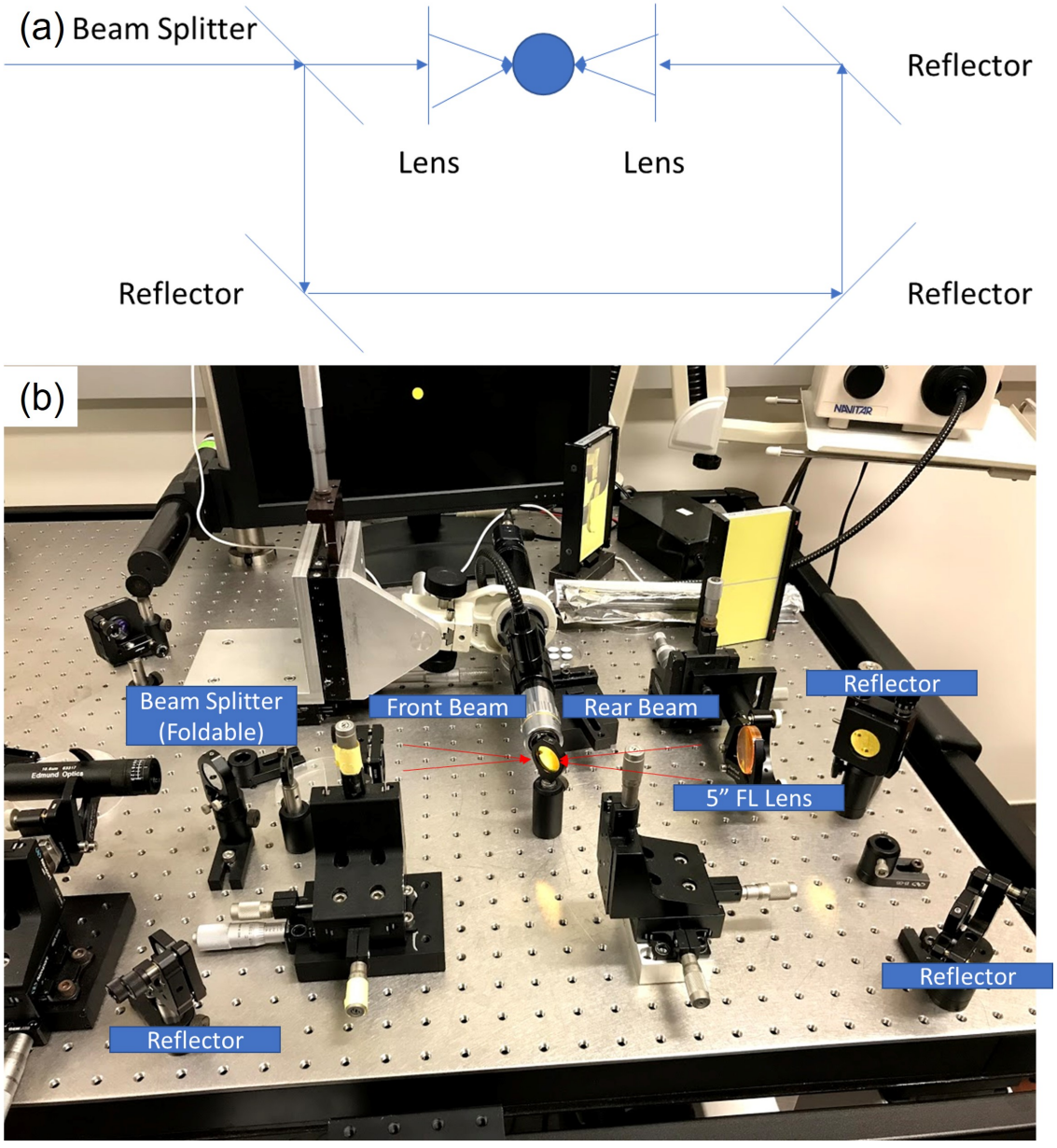

Figure 2.3: Microbubble resonator fabrication technique. (a) Schematic of CO_2 laser alignment. To heat and melt the silica uniformly, two beams are focused on the silica capillary. (b) CO_2 laser alignment for microbubble resonator fabrication. Aperture stops are added to adjust the power of the front and rear beam, so that we could make the beam power match each other.

dispersion perturbation can create a local anomalous dispersion that satisfies the phase-matching condition for the FWM process. This occurrence is also known as intermodal coupling, mode hybridization, or mode anti-crossing. In this work, we will refer to this phenomenon as AMX.

2.2.1 Large-size silica microtoroid resonators

There are several advantages of fabricating a larger size microresonators in a manner of observing the AMX. Firstly, the mode spacing in a large microresonator is much smaller than that in a small microresonator, which leads to a higher density of resonant modes. This makes it easier to access a larger number of modes and to investigate mode crossings in detail. And also, the resonant modes in a large microresonator have a smaller free spectral range (FSR), which is the frequency difference between adjacent resonant modes. In this case, the resonator supports more optical modes that are spectrally overlapping, and the system exhibits more AMXs.

A finite element simulation is performed to find the effective refractive indices of 19 different optical modes in a toroid resonator with a major diameter of 300 μm and minor diameter of 30 μm as a function of wavelength [Fig. 2.4(a)]. The integrated dispersion which reveals second-order or higher dispersion parameters is plotted based on the simulation results [1] and mode crossings can be observed [Fig. 2.4(b)].

Note actual dimensions of a toroid resonator cannot be precisely designed due to its unique fabrication process. Thus, there are some discrepancies between the mode crossings from the simulation and the measurements. However, we believe, even though the measurement and simulation data cannot be directly compared,

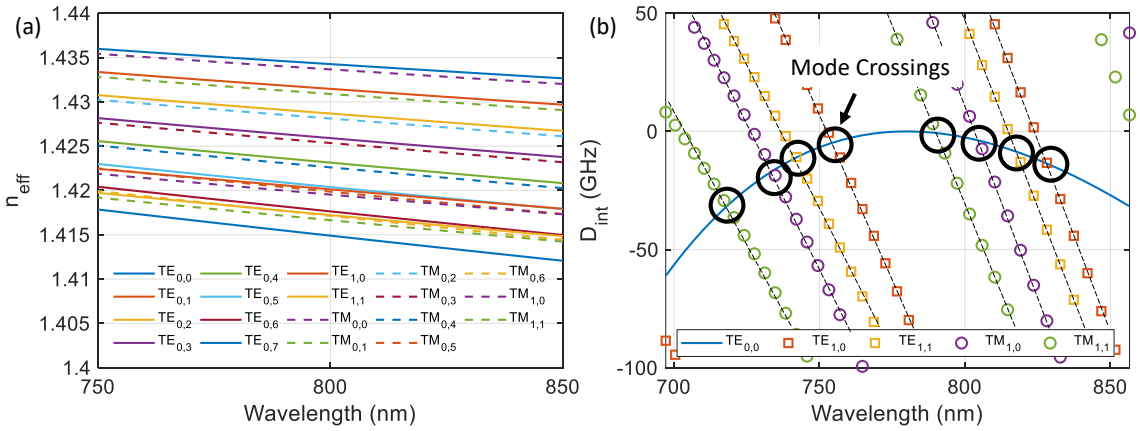

Figure 2.4: (a) Mode families of a microtoroid resonator. Effective refractive indices of a toroid resonator with a major diameter of 300 μm and minor diameter of 30 μm. (b) Integrated dispersion with respect to the fundamental TE mode. Mode crossings with higher-order optical modes are observed.

the presence of AMXs may be claimed [Fig. 2.4(b)].

Fabrication techniques

It is found that a thicker silicon oxide layer are required to obtain high-Q microtoroid resonators due to the thermal expansion mismatch between the silica layer and the silicon substrate [12]. A proper control of thermally induced stress is critical to obtain high-Q resonances. We choose a 6 μm thick silica layer in order to fabricate a toroid resonaotr with a diameter of around $300 - 500$ μm. Figure 2.5 shows the major and minor diameter of the toroid resonator with different silica layer thickness. We can estimate the minor diameter of the toroid resonator for a given major diameter and silica thickness.

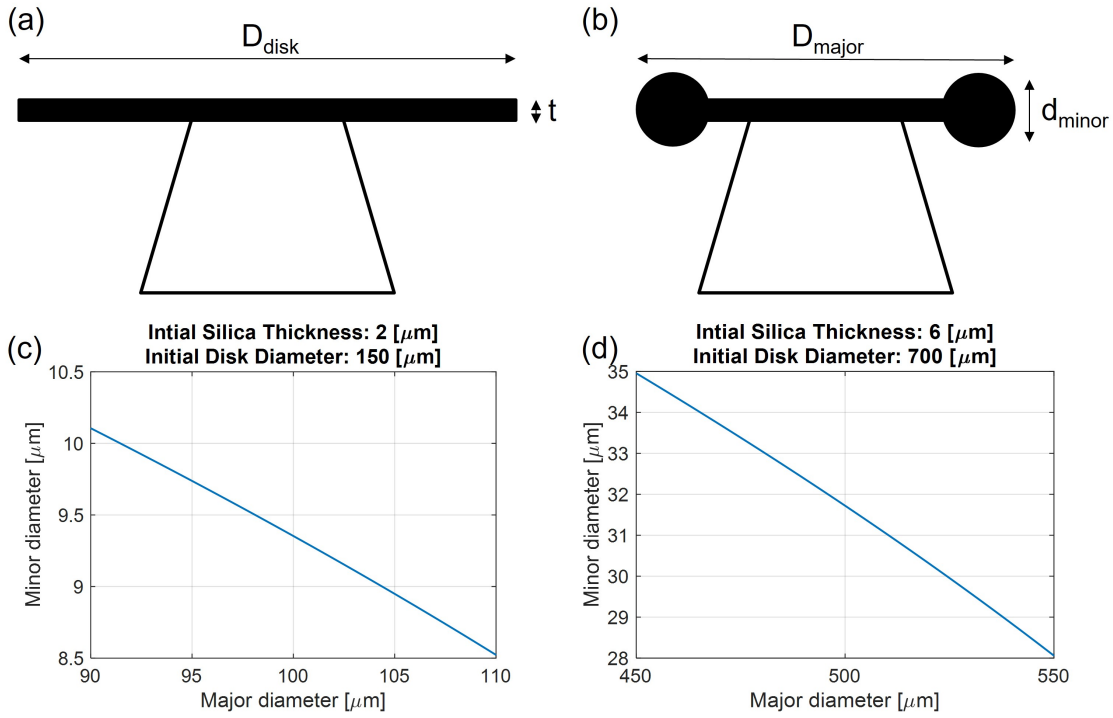

Figure 2.5: Major and minor diameter of toroid resonators with different silica layer thicknesses. (a) A schematic of a fabricated microdisk resonator. D_{disk} is the diameter of the disk and t is the silica layer thickness. (b) A schematic of a fabricated microtoroid resonator. D_{major} is the major diameter and D_{minor} is the minor diameter as depicted in the figure. (c) A relationship between the major and minor diameter of the toroid resonator for $D_{\text{disk}} = 150$ μm and $t = 2$ μm. The major diameter and the minor diameter are inversely proportional for a given disk resonator. (d) A relationship between the major and minor diameter of the toroid resonator for $D_{\text{disk}} = 700$ μm and $t = 6$ μm.

2.3 Lugiato-Lefever equation (LLE) simulation

The Lugiato-Lefever equation (LLE) is a mathematical model that describes the dynamics of light in a driven, Kerr-nonlinear microresonator [13]. It is a partial differential equation that captures the interplay between the Kerr nonlinearity, dispersion, and driving input in the microresonator. The LLE is widely used to study the behavior of optical frequency combs, solitons, and other nonlinear phenomena in microresonators.

The master equation can be written as [13, 14]:

$$\frac{\partial A}{\partial t} - i\frac{1}{2}D_2\frac{\partial^2 A}{\partial \phi^2} - ig|A|^2A = -\left(\frac{\kappa}{2} + i(\omega_0 - \omega_p)\right)A + \sqrt{\frac{\kappa\eta P_{in}}{\hbar\omega_0}}, \tag{2.3}$$

where $A(\phi, t)$ is the internal electric field within the resonator. ϕ is the azimuthal coordinate around the resonator. $\kappa = \kappa_{ex} + \kappa_0$ is the total cavity loss rate, where κ_{ex} and κ_0 are the coupling rate and intrinsic loss rate. $\eta = \kappa_{ex}/\kappa$ is the coupling efficiency. ω_0 and ω_p are the resonance frequency and the pumping frequency. $g = \hbar\omega_0^2 c n_2/n^2 V_0$ is the Kerr frequency shift per photon, where n is the refractive index, n_2 is the nonlinear optical index, and V_0 is the effective mode volume. D_2 is the second order dispersion parameter. In this study, we ignore higher-order ($D_{i>2}$) dispersion parameters to simplify simulations.

The split-step method is a numerical technique commonly used to solve the Lugiato-Lefever equation. It involves splitting the equation into two parts, one that describes the linear propagation and another that accounts for the nonlinear Kerr effect. The linear part is solved using a fast Fourier transform (FFT) algorithm, while the nonlinear part is solved using an iterative numerical method, such as the

Runge-Kutta method.

Simulation parameters can be obtained from a dispersion measurement and a finite element method. Figure 4.4 displays a representative simulation result. The parameters for this simulation are given as follows: $D_1/2\pi = 200$ GHz, $\kappa = \kappa_{ex}/2 = \kappa_0/2 = 24$ MHz, $V_0 = 10866\ \mu\text{m}^3$, $P_{in} = 50$ mW, and $\lambda_0 = 780$ nm. A two-parameter model is used to simulate avoided mode crossings (AMXs) as introduced in [1]. The two parameters, a and b, illustrate the coupling strength and an AMX location, respectively. As shown in Fig. 4.4(a), we introduced one weak and one strong modal crossing in the integrated dispersion (D_{int}) as experimentally measured (similar to what is shown in Fig. Fig. 4.2(c) but not exactly the same). The model parameters a is $\kappa/2$, 10κ, and b is 5, 20 for the weak and strong AMXs, respectively. The resonance is swept from the blue-detuned side to the red-tuned side. The simulation is stopped when a primary comb is observed as shown in Fig. 4.4(b).

2.4 Other third-order nonlinear interactions

There are several nonlinear optical processes that can occur in a microresonator with the third-order nonlinearity besides four-wave mixing (FWM). Third harmonic generation and triple sum frequency generation are possible and have been observed, but they are typically not of interest for the present case as they are not within the comb bandwidth. Stimulated Brillouin scattering and stimulated Raman scattering are other efficient nonlinear processes that can compete with FWM. However, these inelastic photon-phonon scattering processes in the resonator material do not conserve photonic energy unlike FWM, which is necessary for equidistant comb spectra.

2.4.1 Stimulated Raman scattering (SRS)

Stimulated Raman scattering (SRS) is a third-order nonlinear process that can be observed without any dispersion engineering techniques, as it does not require a phase matching condition. To observe SRS, a resonance with an ultra-high quality factor is pumped and thermally locked. Once the pumping power exceeds a certain threshold, Raman lasing occurs, and Figure 2.6 shows the generated spectrum of the SRS process. In this particular case, the pumping wavelength is 778.83 nm and power is 3 mW.

FWM involves the interaction of three or more optical waves to generate a fourth wave, while SRS involves the interaction of light with the vibrational modes of a material, leading to the generation of a scattered photon with a different frequency. In FWM, the generated frequency is either the sum or the difference of the original frequencies, while in SRS, the scattered frequency is shifted from the incident frequency by the frequency of the vibrational mode.

2.4.2 Threshold power for FWM and SRS

The Raman lasing threshold occurs when cavity round-trip gain equals round-trip loss. For an intensity-dependent gain coefficient, the threshold power for SRS is given by

$$P_t^{\text{Raman}} = \frac{\pi^2 n^2}{\lambda_P \lambda_R g_R} V_{\text{eff}} Q_{\text{int},P}^{-1} Q_{\text{int},R}^{-1} \frac{(1+K_P)^2}{K_P}(1+K_R) \tag{2.4}$$

where n is the index of refraction, V_{eff} is the effective pump mode volume, $\lambda_P(R)$ is the pump (Raman) wavelength, g_R is the nonlinear bulk Raman gain

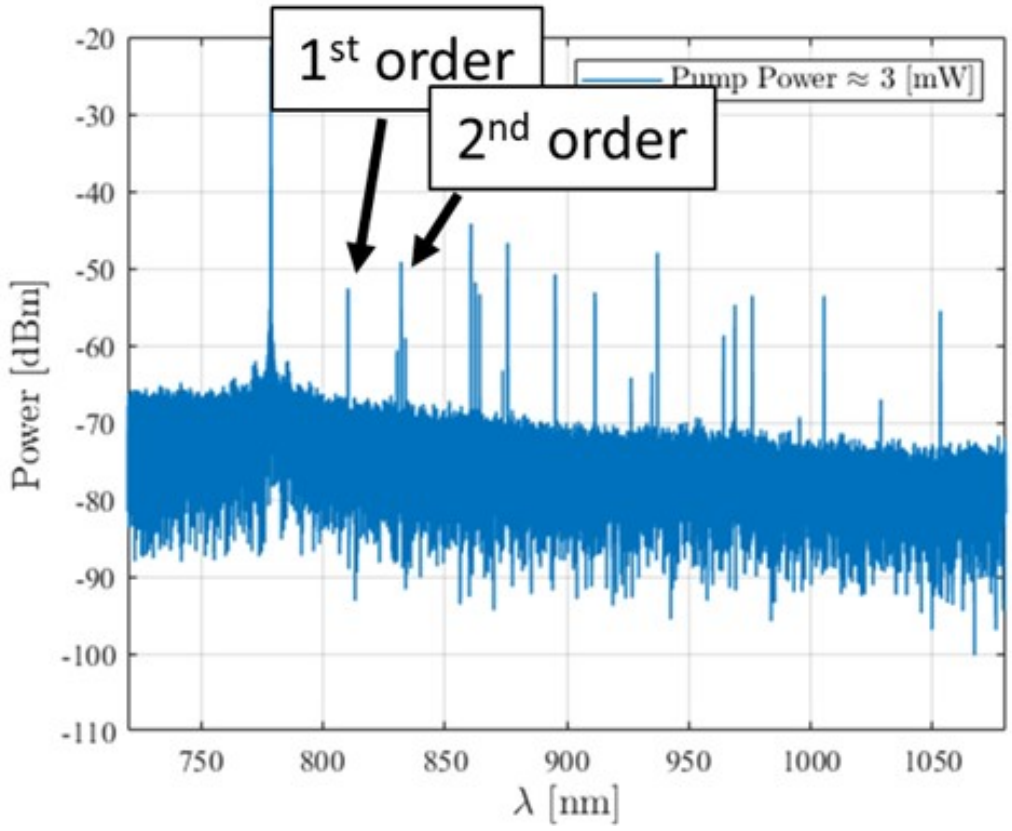

Figure 2.6: Generated stimulated Raman scattering (SRS) spectrum. A pump wavelength is 778.83 nm. The first SRS happens at 810 nm. A cascaded process is observed and continues up to around 10th order. The last SRS is observed at 1050 nm which is more than 200 nm away from the pump wavelength.

coefficient, $Q_{\text{int},P(R)}$ is the intrinsic Q factor for the pump (Raman) mode, and $K_{P(R)} = Q_{\text{int},P(R)}/Q_{\text{ext},P(R)}$ is the coupling parameter for the pump (Raman) mode.

The threshold pump power for FWM is expressed as

$$P_t^{\text{FWM}} = \frac{\omega_0^2 Q_{\text{int}}^{-2}(1+K)^2 + (\Delta\omega/2)^2}{\gamma\Delta\omega(c/n_{\text{eff}})} \frac{\pi^2 R n_{\text{eff}}}{2\lambda_P} \frac{(K+1)^2}{Q_{\text{int}}K} \tag{2.5}$$

where $K = Q_{\text{int}}/Q_{\text{ext}}$ is the coupling parameter, ω_0 is the angular mode frequency, $\gamma = (\omega_P n_2)/(cA_{\text{eff}})$ is the effective nonlinearity, n_2 is the Kerr nonlinearity for silica, c is the speed of the light, A_{eff} is the effective mode area, R is the radius of the resonator,

$$\Delta\omega = 2\omega_P - \omega_s - \omega_i = D_2/2 - \delta\omega$$

is the frequency detuning, $\omega_{s(i)}$ is the angular signal (idler) frequency, D_2 is the second order dispersion coefficient, $\delta\omega = \omega_0 - \omega_P$ is the effective frequency detuning, ω_0 is the angular pump frequency.

Figure 2.7 shows threshold power for FWM as a function of the detuning frequency and coupling parameter. In experiment, $\delta\omega$ is negative and D_2 is positive for the anomalous dispersion regime, and the frequency detuning is positive.

2.4.3 Competition between FWM and SRS processes

In microresonators, four-wave mixing (FWM) and stimulated Raman scattering (SRS) can both be efficient nonlinear optical processes. The competition between these two processes depends on several factors, including the resonator properties, the input power, and the material properties.

FWM is typically more efficient than SRS in microresonators due to the strong

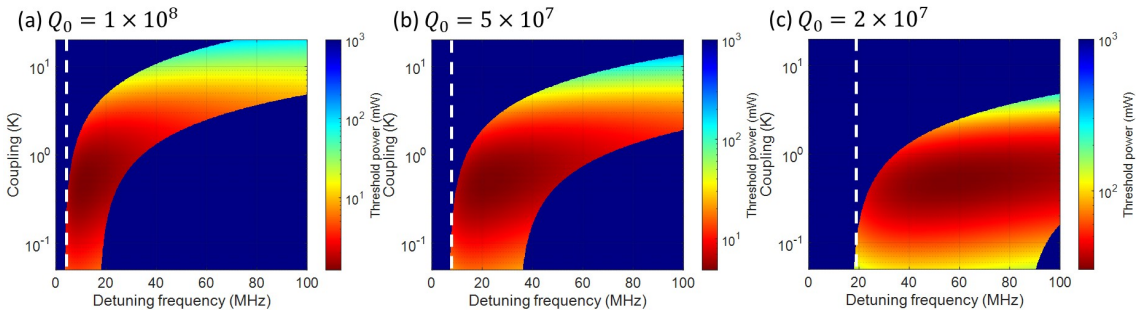

Figure 2.7: Threshold power for FWM and SRS. The SRS dominant region is color-coded as blue, while the FWM dominant region is as red. The threshold power for the FWM is plotted at Q factor of 1×10^8 (a), 5×10^7 (b), and 2×10^7 (c). The minimum threshold power can be found for slightly under-coupled regime. Simulation parameters: $\lambda_0 = 780$ nm, $R = 150$ μm, $n_{\text{eff}} = 1.445$, $g_R = 1.32 \times 10^{-13}$ W/m, $A_{\text{eff}} = 10$ μm^2, $n_2 = 2.2 \times 10^{-20}$ m^2/W.

confinement and enhancement of the optical fields. This makes FWM dominant at low input powers. However, as the input power increases, SRS can become more important, especially when the resonator material has a high Raman gain coefficient. At high input powers, the Raman gain coefficient can be larger than the Kerr coefficient, leading to a switch from FWM to SRS.

Overall, the competition between FWM and SRS in microresonators depends on a complex interplay of resonator properties, input power, material properties, and temperature. Understanding this competition is important for optimizing the performance of microresonator-based devices for various applications, such as optical frequency comb generation.

Figure 2.8 illustrates the complex competition between FWM and SRS as the pump laser is scanned from a short to long wavelength. A thermal triangle is observed and the laser can be thermally locked. At stage I, the FWM process is triggered. The signal and idler frequencies are generated. A cascaded FWM happens

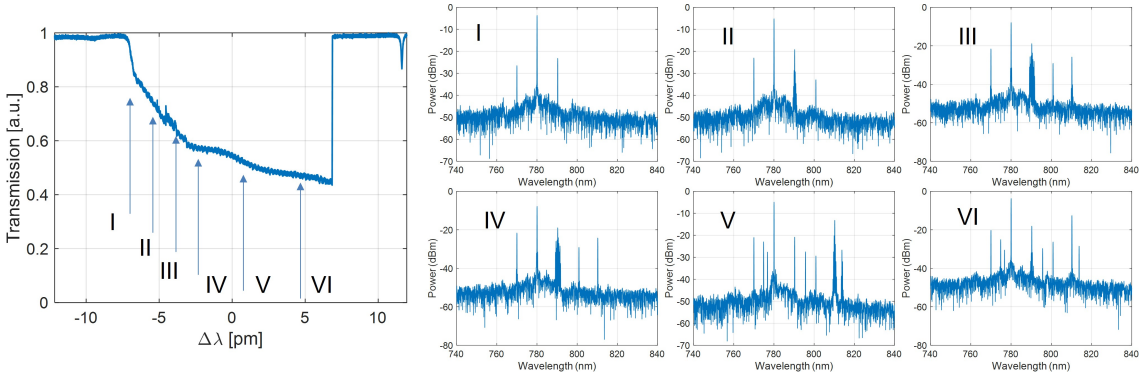

Figure 2.8: Competition between FWM and SRS as a resonance is scanned. (Left) A thermally broadened resonance is scanned from a short wavelength to a long wavelength and (Right) the corresponding measured spectrum at each stage is shown. FWM process is first excited at stage I and the cascaded process continues until stage IV as the laser is scanned. As the intracavity power increases, the SRS is also excited at stage V and the competition between them starts.

and more frequency components are generated at stage II, III, and IV. At stage V, it is interesting that SRS is excited and both of FWM and SRS are present and start to compete each other. This competition is also observed at stage VI and continues.

Coupling sensitive competition

As we discussed in the previous section, the threshold power for the FWM process is dependent on the coupling parameter. Varying the coupling condition may result in different dynamics of the FWM and SRS processes. Figure 2.9 depicts spectra at different coupling condition by varying the contact height between the tapered fiber and the resonator.

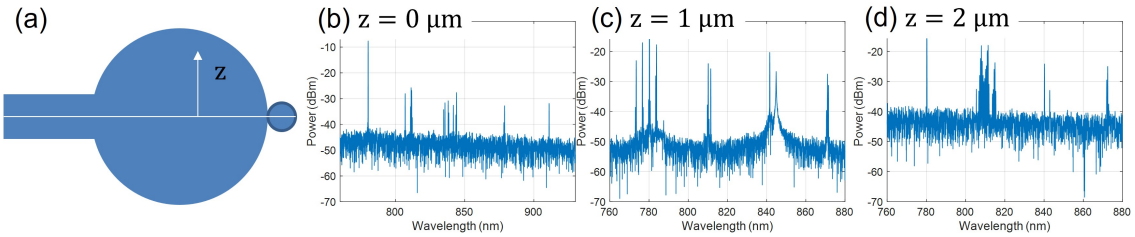

Figure 2.9: Competition between FWM and SRS at various coupling conditions. (a) The microtoroid and the tapered fiber kept in contact. The height, z, is varied from 0 to 2 μm. The toroid resonator and the tapered fiber are in the same equatorial plane at $z = 0$ μm. (b) The SRS is dominant process at $z = 0$ μm. The cascaded SRS is observed. (c) The FWM and SRS are present simultaneously at $z = 1$ μm. (d) The SRS is dominant process at $z = 2$ μm. A Raman comb is also observed.

CHAPTER 3

Optical Frequency Combs in Aqueous and Air Environments at Visible to Near-IR Wavelengths[†]

The ability to detect and identify molecules at high sensitivity without the use of labels or capture agents is important for medical diagnostics, threat identification, environmental monitoring, and basic science. Microtoroid optical resonators, when combined with noise reduction techniques, have been shown capable of label-free single molecule detection, however, they still require a capture agent and prior knowledge of the target molecule. Optical frequency combs can potentially provide high precision spectroscopic information on molecules within the evanescent field of the microresonator; however, this has not yet been demonstrated in air or aqueous biological sensing. For aqueous solutions in particular, impediments include coupling and thermal instabilities, reduced Q factor, and changes to the mode spectrum. Here we overcome a key challenge toward single-molecule spectroscopy using optical microresonators: the generation of a frequency comb at visible to near-IR wavelengths when immersed in either air or aqueous solution. The required dispersion is achieved via intermodal coupling, which we show is attainable using larger microtoroids, but with the same shape and material that has previously been shown ideal for ultra-high sensitivity biosensing. We believe that the continuous evolution

[†]Contents presented in this chapter has been published in "Optical Frequency Combs in Aqueous and Air Environments at Visible to Near-IR Wavelengths," Optics Express, 30, 8690-8699 (2022) [15]

of this platform will allow us in the future to simultaneously detect and identify single molecules in both gas and liquid at any wavelength without the use of labels.

3.1 Introduction

Optical microtoroid resonators are attractive biochemical sensors due to their ultra-high quality (Q) factors and small mode volumes [16, 13, 17, 18, 19, 20, 21, 22]. In addition, microtoroids have a larger capture area compared to nanoscale sensors such as nanorods, nanowires, and nanotoroids [23] thus making detection events more likely [24]. We have previously demonstrated that single molecules can be detected without the use of labels using a microtoroid optical resonator in combination with noise reduction techniques [8, 25, 26]. To achieve specific detection, the surface of the resonator needs to be functionalized for the target molecule of interest. A non-functionalized resonator can also detect binding events; however, in this case not only does the target molecule need to be known in advance, but the solution must either be pure or the molecules of interest must have very different binding characteristics.

In many cases, however, target analytes are unknown and need to be identified. Since optical frequency combs can be used to identify molecular species [27, 28, 29], generating a frequency comb with a microtoroid may enable detection and molecular identification on the same device without having to functionalize the surface of the sensor by measuring amplitude attenuation of comb lines (or absorption spectrum of the target). Surface functionalization adds both complexity and cost to the experiment and reduces the Q-factor which reduces sensitivity. A toroidal geometry is desired for biochemical sensing over other high-Q geometries such as microdisks

that have been used to generate combs as it has a large ($\sim$ 100 nm) evanescent field sensing region that is needed for biochemical sensing.

Despite the potential advantages of using frequency combs for biochemical sensing, frequency comb generation in aqueous solution has not previously been demonstrated. A key challenge is that resonator dispersion is altered significantly when an aqueous solution is injected over the resonator, making it difficult to realize the required anomalous mode dispersion. To the best of our knowledge, conventional dispersion engineering techniques have not addressed this issue [30, 31]. Here, we generated an optical frequency comb in water and air at visible to near IR wavelengths on a microtoroid optical resonator overcoming a limit of conventional dispersion engineering. This can be achieved via an avoided mode crossing (AMX), which is an interplay between different transverse optical modes in a resonator.

3.2 Dispersion engineering and avoided mode crossings

Typically, dispersion engineering is needed to generate microresonator based frequency combs [32]. Total cavity dispersion is a function of material, waveguide geometry, and optical mode distribution. Material dispersion can be engineered by either replacing a material or doping it. For biosensing experiments which are performed in aqueous solutions, it is often desired to use visible or near visible wavelengths as the absorption of light in water at those wavelengths is minimized. At these wavelengths, the group velocity dispersion of a typical material is strongly normal, so the overall cavity dispersion is also normal. However, waveguide dispersion can be engineered to compensate the material dispersion [10], resulting in overall anomalous dispersion even at visible wavelengths. Since different optical modes have

their own mode profile and effective refractive index (n_{eff}) the overall dispersion is also a function of optical mode [1, 11, 33].

Numerous forms of microresonator dispersion engineering have been demonstrated in the near-visible regime. In a microbubble resonator, a very thin waveguide structure was fabricated that confined the light and overcompensated the normal dispersion of the silica for the fundamental TM mode at 780 nm [11]. A silica microdisk with a large wedge angle was shown to achieve an anomalous dispersion at 780 nm by controlling the angle of the wedge (a form of waveguide dispersion) [34]. Anomalous dispersion was also generated in a silicon-nitride integrated ring resonator by using a high radial order mode (modal dispersion) [33, 35]. These demonstrations are all based on a fixed cladding material; however, varying the surrounding material can alter the overall dispersion.

While tight confinement of light can overcompensate material dispersion in the visible and NIR wavelength regime, a high refractive index contrast between the waveguide material (i.e., silica) and the cladding (i.e., air) is needed. If the surrounding air is replaced by a liquid ($n > 1.33$), the light loses strong confinement, and the normal dispersion of the material cannot be compensated (see Supplementary Information Section 1 for more details). Several ways to overcome this issue include adding a high index material coating on the resonator surface [36, 37, 38], engineering the modal dispersion of a cavity [33], or replacing the waveguiding material by a higher index material [39, 30, 31].

If, however, it is desired to preserve the material and structure of a resonator, a different approach is needed. A distinct property of a resonator where different optical modes have their own free spectral range (FSR) is that they can interact

and couple with one another resulting in deviations from the original, unperturbed FSR [40, 41, 1, 42]. This localized dispersion perturbation can lead to a local anomalous dispersion which can meet a phase-matching condition for the four wave mixing (FWM) process. At visible or near visible wavelengths, optical frequency combs have been generated via AMXs in a crystalline WGM resonator [41], a microring resonator [43, 44, 45], dual microring resonators [46, 47], and a wedge disk resonator [9, 48, 49]. Chip-based ring resonators can be designed to introduce AMXs at desired locations using a thermal heater [50] or by adding an another resonator nearby [51, 46, 47]. Although toroidal resonators have been one of main platforms in biosensing experiments, there has been no demonstration of optical frequency comb generation under a sensing environment where the toroid is immersed in liquid.

3.3 Device fabrication & dispersion measurement

Currently, microtoroids with a major diameter of ~ 100 μm are used for biosensing applications [8] . This diameter, however, yields a large FSR ($\sim$ 700 GHz in the NIR) resulting in only tens of mode numbers in the scanning wavelength range ($\sim$ 8 THz) of our system. To efficiently introduce and characterize AMXs, it is highly desirable to have many modes. This can be done by fabricating a larger diameter toroid [52]. To fabricate larger toroids [Fig. 3.1(b)], we chose a thicker silica layer in order to avoid stress induced defects ("buckling") caused by different thermal expansion coefficients between the silica layer and the substrate as the cavity diameter increases [12]. Buckling can significantly degrade the fabrication quality but can be controlled by proper choice of the device layer thickness and the amount of undercut and is therefore not a limiting factor for the optical performance of the

device if for example, we wish to change the FSR of the resonator [9].

To fabricate a large ($\sim$ 500-μm) diameter microtoroid, a $\sim$ 700-μm diameter disk resonator is first fabricated using conventional lithography and etching techniques [6, 53, 54]. A thermally grown 6 μm thick silicon dioxide layer on top of the silicon substrate (WaferPro) was used. The amount of undercut for the microdisk needs to be large enough to isolate an optical mode from the silicon pillar and small enough to prevent buckling. By defocusing our laser beam and increasing the power of the CO_2 laser, we can reflow $\sim$ 500-μm-diameter or larger toroids [Fig. 3.1(b)]. An ultra-high Q factor ($Q > 10^8$) is routinely measured. Figure 3.1(c) shows a linewidth measurement of a resonance of a large-diameter toroid in air. Laser scanning is calibrated with a Mach-Zehnder interferometer (MZI). A linewidth measurement of the cavity in water is shown in Fig. 3.1(e). Typically the linewidth broadens by around a factor of two when the cavity is immersed in a liquid due to less mode confinement or particle binding due to impurities in the liquid.

The cavity is characterized by first positioning a large-diameter toroid resonator in a sample chamber built by gluing a glass coverslip on top of a custom made sample holder [Fig. 3.1(b)]. Water which is de-gassed in a vacuum chamber is then injected into the chamber with a syringe pump. When the chamber is filled with liquid, a tapered fiber is coupled to the resonator to inject light into the cavity. A tunable laser (New Focus TLB-6712-P) scans wavelengths from 765 nm to 781 nm while its scan wavelength is precisely calibrated by a MZI with a FSR of 17.5 MHz. The calibration data and the transmission signal are both received by photodetectors (New Focus 1801) and monitored by a high sampling rate data acquisition card (NI PCI-6115) [55, 32]. An example spectrum is shown in Fig. 3.1(d). More than 10

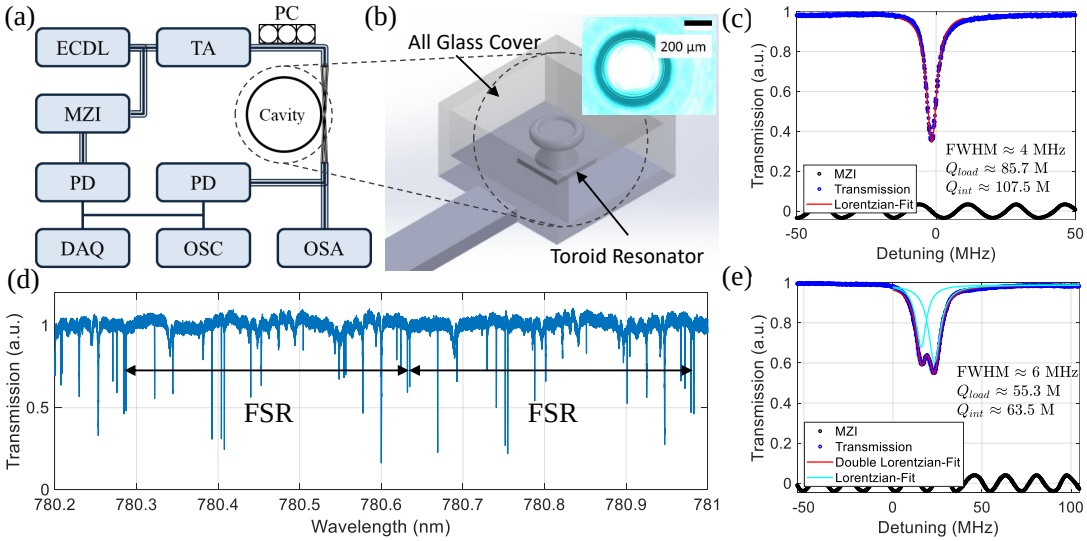

Figure 3.1: (a) Experimental Setup. An external cavity diode laser (ECDL) is amplified by a tapered amplifier (TA) and pumped into a cavity. A polarization controller (PC) is used to excite either the TE or TM mode family. Laser wavelength scanning is calibrated using a Mach-Zehnder interferometer (MZI). The calibration and transmission data are received by photodetectors (PDs) and monitored using a data acquisition (DAQ) system or an oscilloscope (OSC). The spectrum was simultaneously measured using an optical spectrum analyzer (OSA). (b) Schematic of the sample chamber. Inset: microscope image of the microcavity. (c) Q-factor measurement in air for a microtoroid. The frequency axis is calibrated by a MZI of $FSR_{MZI} \approx 17.5$ MHz. The loaded Q-factor of the fundamental mode was $\sim 1 \times 10^8$. (d) Representative example of the calibrated spectrum scan. (e) Linewidth measurement for the same toroid in water. Typically, the quality factor drops by around a factor of 2. For simplicity, the linewidth of the left peak is used for the Q-factor estimation.

modes are excited as shown in the spectrum of approximately two FSRs. In order to introduce AMXs, we excited not only the low order modes but also other higher order modes in the cavity by placing the tapered fiber in contact with the top of the toroid [56] and adjusting phase-matching conditions [57]. In order to enhance the stability of the coupling condition, a wall is fabricated next to the toroid and used to support the fiber [58]. The laser is tuned to a resonance by decreasing optical frequency to achieve thermal locking [59]. The spectrum is recorded using an optical spectrum analyzer (OSA, Thorlabs 202C).

3.4 Frequency comb generation in water and air

Frequency comb generation in water using a microtoroid resonator via the AMX approach is shown in Figure 3.2. The dispersion of the cavity is characterized and plotted in Figs. 3.2(a), (c), and (e). The measured resonance frequencies are marked as dots over the whole scan spectrum. The resonance frequencies are plotted as deviations from an equidistant frequency grid with a FSR (D_1). A mode family can be interpreted as a line connecting dots. If a mode family has a FSR of D_1 and no dispersion, it may be shown as a horizontal line. Different slopes of each line can be understood as different FSRs for each mode family. The color of the dots represent measured Q-factors and helps trace a mode family.

To better understand the eigenfrequency locations, we analyze the dispersion properties of our comb. The dispersion properties of a mode family with mode frequencies, ω_μ, can be Taylor expanded as, $\omega_\mu = \omega_0 + D_1\mu + \frac{1}{2}D_2\mu^2 + \ldots$, where μ is the relative mode number with respect to the pump (μ_0), ω_μ are the resonance frequencies, ω_0 is the pump frequency, $D_1/2\pi$ is the FSR, and $D_2/2\pi$ is the second

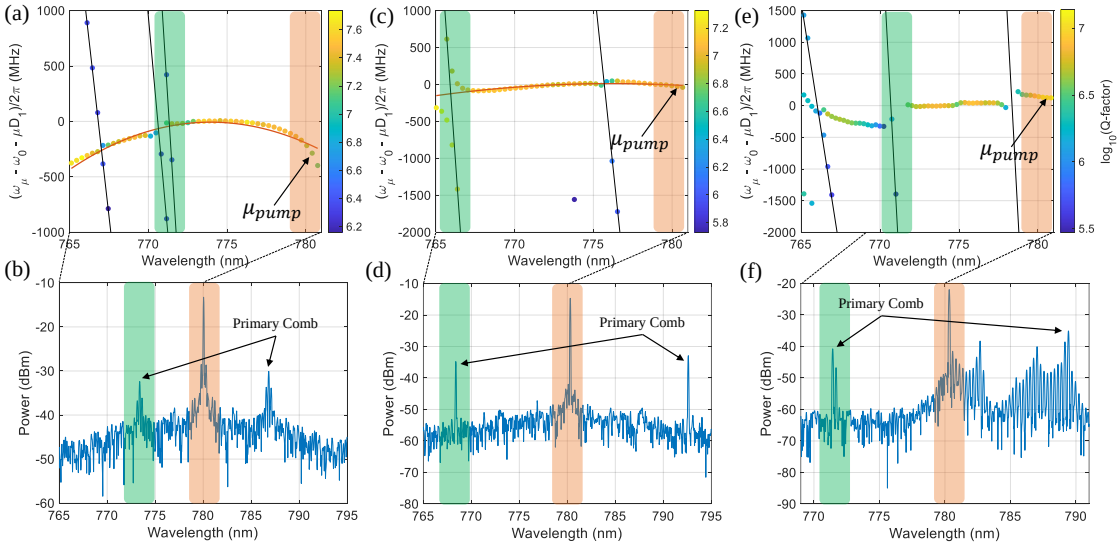

Figure 3.2: Dispersion measurement and frequency comb generation in water. (a) Deviation of the resonance frequencies, $\omega_\mu = \omega_0 + D_1\mu + \frac{1}{2}D_2\mu^2 + \ldots$, from an equidistant frequency grid ($\omega_0 + D_1\mu$) and μ is the relative mode number, where $D_1 = 2\pi \times FSR$ with respect to a pump mode (μ_0). Each dot on the plot related to an eigenfrequency (ω_μ) of the cavity. A particular mode family is represented as a line that consists of colored dots corresponding to measured Q-factors on a logarithmic scale. The dot color may be used to identify a particular mode family because a mode family has similar Q. The integrated dispersion, $D_{int} = \omega_\mu - \omega_0 - D_1\mu = \frac{1}{2}D_2\mu^2 + \ldots$, describes normal dispersion with $D_2/2\pi = -1.1877$ MHz (red solid line; higher-order terms are ignored). Black solid lines are drawn to visualize higher order mode families and AMXs. The AMX can be easily observed because it significantly alters eigenfrequencies, degrades the Q-factor (shown by the dot color) and transmission depth of the resonances (not shown here). The pump wavelength and AMX location is highlighted in orange and green, respectively. (b) Generated frequency comb in water when the mode indicated in (a) is pumped. The primary comb is located at the wavelength where the AMX happens (highlighted in green). (c) The integrated dispersion for a mode family with a $D_2/2\pi \sim -0.5158$ MHz. The pump wavelength and AMX location is highlighted in orange and green, respectively. (d) Generated frequency comb in water by pumping the mode shown in (c). The primary comb is located at the wavelength where the AMX happens (highlighted in green). (e) The integrated dispersion for a mode family where AMXs are considerably strong and dispersion cannot be measured precisely. The pump wavelength and AMX location is highlighted in orange and green, respectively. (f) The generated frequency comb when the mode indicated in (e) is pumped.

order dispersion (with higher order dispersion terms ignored) [60]. It is often useful to introduce an integrated dispersion, $D_{int} = \omega_\mu - \omega_0 - D_1\mu = \frac{1}{2}D_2\mu^2 + \ldots$, which shows the deviation of the resonance frequencies from the equidistant frequency grid (FSR $= D_1/2\pi$) with respect to a pump mode ($\mu = 0$). The integrated dispersion is plotted to extract D_2 by fitting a curve ($D_{i>2}$ are ignored). Note that $\mu_0 \neq \mu_{pump}$ for plotting purposes. The fitted dispersion coefficients are $D_1/2\pi = 170.7088$ GHz, $D_2/2\pi = -1.1877$ MHz for a family [Fig. 3.2(a)] and $D_1/2\pi = 170.7073$ GHz, $D_2/2\pi = -0.5158$ MHz for another mode family [Fig. 3.2(c)]. Dispersion for a mode family shown in Fig. 2(e) may not be estimated where a dispersion curve is distorted due to several strong AMXs present for the mode family. Because of the limited wavelength scan range and the presence of strong and weak modal couplings, an accurate measurement of these fits can not be faithfully guaranteed. The discrepancy between the fitted $D_2/2\pi \approx -1.19$ MHz and the simulated $D_2/2\pi \approx -1.63$ MHz can be attributed to fabrication uncertainty and the aforementioned limits.

Frequency comb generation in water was observed by pumping a resonance at $\sim$ 780 nm at a pump power of $\sim$ 20 mW [Fig. 3.2(a)]. The primary comb (the first generated sideband) is located where the AMX happens [Fig. 3.2(b)]. A small deviation between the AMX location ($\lambda > 772$ nm) and the primary comb location ($\lambda > 773$ nm) can be explained by a frequency shift resulting from a temperature increase of the cavity as a function of input power and detuning. As the resonance is swept from high to low frequencies, an increase in intracavity power makes the cavity hot and the frequency shift. This alters AMX locations because different transverse modes might have different temperature shift coefficients [47, 61]. Another mode family with a strong AMX at $\sim$ 767 nm and a weak perturbation at $\sim$ 776 nm

is pumped [Fig. 3.2(c)]. As shown in Fig. 3.2(d), a stronger modal coupling may satisfy the phase-matching condition first over others when multiple AMXs exist even though the AMX is positioned further away from the others. Thus, the primary comb line is located at ~ 767 nm rather than ~ 776 nm. Finally, the other mode family [Fig. 3.2(e)] is pumped where strong AMXs are present and undisturbed dispersion may not be characterized faithfully. The generated frequency comb is shown in [Fig. 3.2(f)] and a significant asymmetry can be observed.

Some applications such as environmental monitoring require sensing and identification of particles in air [62]. Thus, a broadband frequency comb in air via an AMX is demonstrated and shown in Fig. 3.3. Two different mode families are investigated. A high order mode family is pumped and the integrated dispersion is shown in Fig. 3.3(a) with $D_1/2\pi$ of 214.8031 GHz and $D_2/2\pi$ of -1.4099 MHz approximately. There is no interaction between the pump mode family and a higher-order mode family at $\lambda \sim 773$ nm where no apparent frequency shift and line broadening are observed. A weak perturbation is present at $\lambda \sim 779$ nm, but primary comb lines appear at $\lambda \sim 788$ nm (48 FSRs away) which is beyond the scan range of our tunable laser [Fig. 3.3(b)]. It is interesting to note that when several AMXs exist at the pump wavelength, they compete to determine which is dominant in forming the comb. A strong AMX outside the scan range may explain the position of the primary comb line. As the laser is tuned from high to low frequency, a broader frequency comb is generated covering more than 300 nm [Fig. 3.3(c)]. A strong AMX might also explain the broad spectrum of the frequency combs [63]. Figure 3.3(d) shows intergrated dispersion for a low order mode family. Fitting a curve yields $D_1/2\pi \approx 214.7849$ GHz and $D_2/2\pi \approx -1.5074$ MHz. There is a weak AMX at

$\lambda \sim 772$ nm and a strong AMX $\lambda \sim 778$ nm. However, it is unexpected the primary comb is not positioned at the strong AMX but rather ~ 30 nm (63 FSRs) away from the pump wavelength. We believe this observation can be attributed to detuning dependent AMXs and the competition between AMXs. Resonators of similar size have been used to sense $H^{13}CN$, CH_2Cl_2, and acetone [64, 29, 65]. Proteins, due to their larger molecular weight, have a broader absorption spectrum. In practice, finer spectroscopic resolution can be obtained by using a dual comb technique to record sharp absorption features in a particular gas phase sample.

In order to better understand primary comb generation in the presence of multiple AMXs for a particular pump wavelength, a numerical simulation was performed using the Lugiato-Lefever equation [13, 66, 67] (see Supplementary Information Section 2 for more details). The integrated dispersion is determined using a simplified two-parameter model [1] from experimental data [Fig. 3.2(e)] and is shown in Fig. 3.4(a). A strong AMX is present at $\mu = 20$ and a weak AMX exists at $\mu = 5$. A resonance is pumped at 780 nm with 50 mW. Figure 3.4(b) shows the primary comb lines which agree with the strong AMX location ($\mu = 20$). It was found that adjusting modal coupling strengths results in different comb generation dynamics (see Supplementary Information Section 4 for more details). For example, from the simulation, by increasing the coupling strength for the weak perturbation, the primary comb lines may appear at both weak and strong AMX locations.

3.5 Conclusion

In conclusion, we generated optical frequency combs in water with a microtoroid resonator using an AMX approach. Although this demonstration is limited by nat-

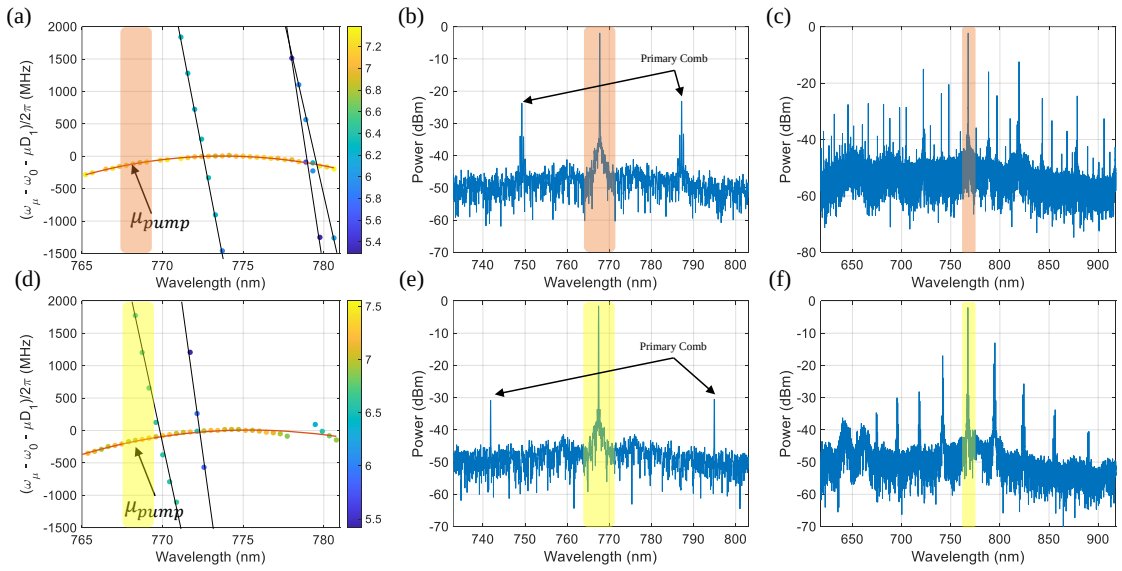

Figure 3.3: Measured dispersion and generated frequency comb in air. (a) Integrated dispersion of a mode family where only a weak modal coupling is present in the scan range. The pump wavelength is highlighted in orange. The dot color represents the quality factor in a logarithmic scale and helps to trace a mode family as shown in (a) and (d). (b) Primary comb lines appear beyond the wavelength scan range from the blue-detuned side. When multiple AMXs exist for the mode family, the primary comb does not appear at the closest AMX location but rather might be dependent on coupling power between the modes. (c) A broadband frequency comb generated as the laser scans from short to long wavelengths. The spectrum spans over 300 nm and covers the visible wavelength range. (d) Integrated dispersion for another mode family. Several AMXs are observed over the wavelength scan range. The pump wavelength is highlighted in yellow. (e) Primary comb lines occur at ~ 30 nm away from the pump wavelength. (f) A broadband frequency comb spanning more than 200 nm.

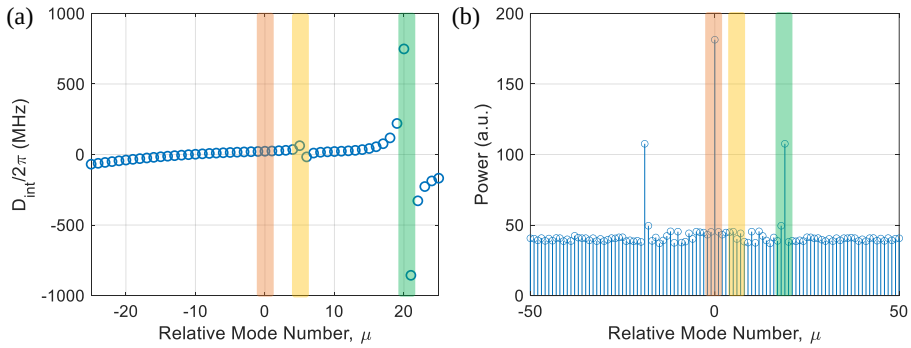

Figure 3.4: Numerical simulation on primary comb. (a) Simulation of the integrated dispersion. Simulation parameters are described in the main text. A simple two-parameter model is used [1]. The pump mode, and weak and strong mode location are highlighted in orange, yellow, and green, respectively. (b) Primary comb line generation. The primary comb is generated where the stronger AMX happens (highlighted in green).

urally occurring AMXs and a few comb lines observed, it suggests that one optical resonator may function as both a spectrometer and a biosensor without building additional structures. By introducing a Pound-Drever-Hall (PDH) locking mechanism, improving the mechanical stability, and controlling temperature of the device via a thermoelectric cooler (TEC) in liquid, we believe a broadband and low phase noise frequency comb (or dark soliton) can be generated with a proper choice of pumping power and detuning [50]. A further investigation on AMXs was performed in air when there were multiple AMXs for a pump's mode family. It was found that if multiple AMXs are present, they compete with each other and the primary comb line location may be determined by the intermodal coupling strength. A broadband optical frequency comb spanning 300 nm was generated with the aid of a strong AMX far away from the pump wavelength in the visible to NIR regime in air. We note that the binding of molecules on the toroid could affect frequency comb genera-

tion dynamics, but this effect might be minimized in case the frequency shift caused by a particle binding (about 5 MHz for a particle size of 100 nm) is much smaller than the FSR of the resonator (200 GHz) in this study [8]. This study suggests a path for a new multi-functional photonic device that may detect and identify a single molecule of interest in both gas and liquid.

CHAPTER 4

Impact of Stimulated Raman Scattering on Dark Soliton Generation in a Silica Microresonator[†]

Generating a coherent optical frequency comb at an arbitrary wavelength is important for fields such as precision spectroscopy and optical communications. Dark solitons which are coherent states of optical frequency combs in normal dispersion microresonators can extend the operating wavelength range of these combs. While the existence and dynamics of dark solitons has been examined extensively, requirements for the modal interaction for accessing the soliton state in the presence of a strong Raman interaction at near visible wavelengths has been less explored. Here, analysis on the parametric and Raman gain in a silica microresonator is performed, revealing that four wave mixing parametric gain which can be created by a modal-interaction-aided additional frequency shift is able to exceed the Raman gain. The existence range of the dark soliton is analyzed as a function of pump power and detuning for given modal coupling conditions. We anticipate these results will benefit fields requiring optical frequency combs with high efficiency and selectable wavelength such as biosensing applications using silica microcavities that have a strong Raman gain in the normal dispersion regime.

[†]Contents presented in this chapter has been published in "Impact of stimulated Raman scattering on dark soliton generation in a silica microresonator," Journal of Physics: Photonics, 5, 014001 (2022) [68]

4.1 Introduction

The ultra-high quality (Q) factor and small mode volume of a microresonator greatly enhances the intracavity intensity in the microresonator and yields nonlinear effects such as stimulated Raman scattering (SRS) and four-wave mixing (FWM) [69, 70, 71]. While FWM is a parametric process where phase matching should be satisfied, SRS does not require phase matching [72, 16]. Engineering the dispersion of the cavity and choosing proper experimental parameters can excite FWM over SRS, and generate optical frequency combs [16, 73, 74, 75]. The FWM process can initiate a Kerr frequency comb and lead to soliton generation in microresonators with a proper choice of power and detuning [60, 13, 14]. It was shown that a bright soliton which is a coherent state of an optical Kerr frequency comb in the anomalous dispersion regime can be soft-excited inherently (i.e., the soliton state can be reached with a continuous wave (cw) background) only recently in microresonators [76, 13], while more extensive studies had been performed in other platforms such as fiber lasers [77, 78, 79, 80, 81, 82]. In contrast, dark solitons may be soft-excited via intermodal interaction [50, 83, 44] or aid of an auxiliary resonator [47, 51, 61, 84], and hard-excited (i.e., the soliton state cannot be reached with a cw background and may require manipulation of the background) by a modulated pump [85, 86, 87] or self-injection locking [88, 89, 90] in the normal dispersion regime.

While optical microresonators can be designed to possess anomalous dispersion at near-visible wavelengths by engineering the geometry of the resonator, often this requires precise fabrication control or additional fabrication processes (e.g., incorporation of a particular coating) [32]. Anomalous dispersion, however, can also be

created locally via interaction of different optical mode families supported in the resonator. This can occur regardless of the dispersion of the cavity and operating wavelength [45, 50]. Since WGM resonators such as microtoroids and spheres can support a greater number of optical modes compared to integrated microring resonators, they can introduce modal interaction without precise fabrication techniques. Thus, in this paper, we only focus on the mode-interaction-aided excitation method which may be readily implemented on WGM resonators (e.g., microtoroid or microsphere resonators) that are an attractive platform due to their higher Q factor and do not need ultra-fine fabrication techniques as their surface roughness can be greatly reduced by a thermal reflow process [91, 6]. Note that a higher Q factor not only decreases the threshold power for nonlinear effects but is beneficial in applications, such as biosensing [8, 15, 92, 20, 21, 24, 26, 93, 94].

SRS can lead to Raman lasing by pumping a resonance above its SRS threshold power regardless of the dispersion of the cavity [72, 95]. Although engineering dispersion of a cavity can make the FWM process dominant over the SRS process in the anomalous dispersion regime, there may still be effects of the Raman interaction including Raman self-frequency shift [96] and Stokes solitons [97, 98]. In crystalline materials where the Raman gain has a narrow bandwidth, SRS can be avoided by not overlapping the Raman gain and a mode of a cavity [99, 100]. Moreover, due to the narrow Raman gain, it was demonstrated that SRS can assist FWM in normal dispersion [101]. The interaction between FWM and SRS can also yield effects such as Raman combs [102, 103], and broader Kerr frequency combs [104, 105].

The transition and competition between SRS and FWM has been studied in the context of frequency detuning between a pump laser frequency and a resonant

frequency, coupling conditions, and geometrical factors [16, 106, 74, 107, 108]. The transition from Raman oscillation to FWM based parametric oscillation was reported in these works, but their analysis is limited to comparing the gains (or threshold powers) for both phenomena. In fact, complex dynamics of these nonlinear effects can be better understood by considering their interactions combined with discrete resonance modes separated by a free-spectral range (FSR) in a microcavity [109, 110, 111, 112]. While there are a number of studies on this interaction in optical resonator systems in the anomalous dispersion regime [113, 102, 114, 96, 115, 97, 116, 105, 117, 118, 104], only a limited number of studies focus on this in the normal dispersion regime [119, 101, 120, 121]. This is partly due to its difficult excitation in experiments [76, 50]. Although the excitation dynamics of dark solitons [63, 122, 44] and the influence of SRS on dark solitons [121] has been investigated, the complex interaction of SRS and dark solitons and their excitation dynamics has been less explored. Furthermore, in a material with a strong Raman gain, dark soliton generation may be significantly perturbed by SRS. This will, in turn, yield more limited conditions for both the excitation and stability region of the dark soliton.

In this work, to address a lack of exploration on the issues above, we numerically study the excitation and accessibility of dark solitons in the presence of Raman interactions in a normally dispersive microresonator at near-visible wavelengths (here, 780 nm). We choose this wavelength region for potential biological sensing applications where aqueous solutions absorb less light compared to infrared region. Since the Raman gain (g_{R}) at this wavelength is twice as big as at infrared wavelengths (i.e., $g_{\mathrm{R}}\ (\lambda = 0.78\,\mu\mathrm{m}) \approx 2g_{\mathrm{R}}\ (\lambda = 1.55\,\mu\mathrm{m})$), the interaction may be even

more complex [123, 124]. It was found that an additional frequency shift caused by an avoided-mode-crossing (AMX) effect due to intermodal coupling can create parametric gain whose amplitude and bandwidth are dependent on both location and amplitude of the AMX. In case the pump power is below the threshold power for SRS, FWM can be initiated and a dark soliton can be generated with a proper AMX condition. Moreover, even if the pump power is above the threshold power for SRS, a dark soliton can still exist but under more restricted conditions. We first study how parametric gain can be introduced by the mode-interaction (or AMX) and compare the parametric gain with the Raman gain with different simulation parameters in section 4.2. Next, we numerically simulate a dark soliton under fixed parameters (section 4.3). In section 4.4, we discuss in detail interactions of FWM and SRS under different conditions. Finally, simulated stability charts are presented in section 4.5.

4.2 Gain curves for FWM based parametric oscillation and stimulated Raman oscillation

Raman gain exists regardless of the dispersion of a cavity, and can stimulate Raman oscillation with no phase matching condition satisfied if it is externally pumped beyond its threshold power [16]. The Raman gain per roundtrip, g_{R}, in silica can be expressed as follows [123, 125, 111]:

$$g_{\mathrm{R}} = \alpha + g^{R}_{\mathrm{bulk}} \frac{P_0}{A_{\mathrm{eff}}} L_{\mathrm{eff}}, \tag{4.1}$$

where $\alpha = (\alpha_i + \theta)/2$ is the total roundtrip loss in amplitude, α_i is the roundtrip loss in intensity due to absorption and scattering, θ is the coupling coefficient between the cavity and the waveguide. $g^R_{\text{bulk}} \approx 1.3 \times 10^{-13}$ m/W is the bulk Raman gain of silica at 780 nm, A_{eff} is the effective mode area, $L_{\text{eff}} = (\alpha/L)^{-1}(1 - \exp(-\alpha))$ is the effective length, L is the length of the cavity, and P_0 is the intracavity power which can be obtained by the following equation [125, 111]:

$$(\gamma L)^2 P_0^3 - 2\delta_0 \gamma L P_0^2 + (\delta_0^2 + \alpha^2) P_0 = \theta P_{\text{in}}, \tag{4.2}$$

where $\delta_0 = t_R(\omega_0 - \omega_{\text{p}})$ is the phase detuning of the pump frequency (ω_{p}) with respect to the nearest resonant frequency (ω_0), t_R is the cavity roundtrip time, $\gamma = n_2\omega_0/(cA_{\text{eff}}) \approx 0.014$ is the nonlinear coefficient, n_2 is the nonlinear refractive index, c is the speed of light in vacuum, and P_{in} is the pump power. Note that the Raman gain is linearly dependent on the intracavity power which can be determined by choosing a detuning and pump power for a cavity.

In the anomalous dispersion regime, the parametric gain of a cavity, g_{cav}, can be created and expressed by the equation [16, 110, 111]

$$g_{\text{cav}}(\Omega) = \alpha + \sqrt{(\gamma L P_0)^2 - (\delta_{\text{mis}})^2}, \tag{4.3}$$

where $\delta_{\text{mis}} = \delta_0 - (\beta_2/2)L\Omega^2 - 2\gamma L P_0$ is the phase-mismatch due to the detuning, dispersion, and nonlinearity, β_2 is the second-order dispersion coefficient ($\beta_2 < 0$ in anomalous dispersion regime), $\Omega = bD_1$ is the modulation frequency, b is the mode number with the additional frequency shift ($b = 1$, unless otherwise stated,

for simplicity), and $D_1 = 2\pi\text{FSR}$ is the FSR in angular frequency at ω_0.

The parametric gain created by AMX may be expressed by adding an additional phase shift in the normal dispersion regime ($\beta_2 > 0$). The phase-mismatch term then becomes

$$\delta_{\text{mis}} = \delta_0 - (\beta_2/2)L\Omega^2 - 2\gamma LP_0 + \Delta\delta \tag{4.4}$$

where $\Delta\delta = \Delta\omega t_R$ is the additional phase shift per roundtrip, $\Delta\omega = a\kappa$ is the corresponding angular resonance frequency shift, a is the normalization factor of the additional frequency shift, and $\kappa/2\pi$ is the FWHM of the resonance of the cavity. The second term in equation (4.4) which is negative in the normal dispersion regime may be compensated by the additional frequency shift due to AMX (i.e., $\Delta\delta > 0$). Figure 4.1(a) shows both the normalized parametric gain and Raman gain at different additional frequency shifts as a function of normalized power, $S = \sqrt{\gamma L\theta P_{\text{in}}/\alpha^3}$, at a fixed detuning, $\delta_0 = 0$. Raman gain is not dependent on the additional frequency shift and it remains the same. Interestingly, parametric gain can be created by the $\Delta\omega$. It was found that the threshold power, existence range, and maximum gain for the FWM process are dependent on the $\Delta\omega$. The threshold power tends to increase linearly with the addition frequency shift, while the existence range and maximum gain hit a maximum at a certain $\Delta\omega$ value.

In practice, only the detuning is swept from high to low frequency instead of the pump power to access a 'thermal triangle' [59]. Thus, it may be straightforward to plot the gain curves as a function of detuning from the blue to red-detuned side. Figure 4.1(b) shows the same gain curves as a function of the normalized detuning, $\Delta = \delta/\alpha$, at a fixed normalized power, $S = 4$, for different $\Delta\omega$ values. The

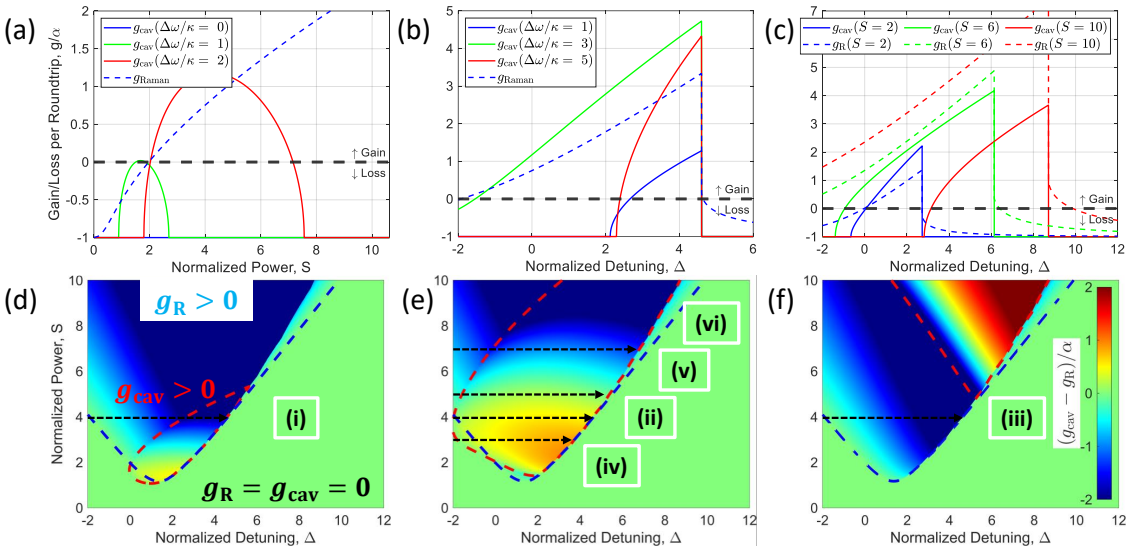

Figure 4.1: Parametric four-wave mixing (FWM) and stimulated Raman scattering (SRS) gain curves. (a - c) Gain/loss per roundtrip vs (a) normalized power and (b), (c) normalized detuning in the normal-dispersion regime. (a) Detuning (δ_0) is fixed at 0. No gain is present in the absence of modal interaction. Parametric gain can be created by introducing modal interaction ($\Delta\omega > 0$), which determines an amplitude and width of the gain envelope, and a threshold power. (b) Normalized power (S) is fixed at 4. Raman gain is not dependent on the frequency shift. Parametric gain is maximized at $a \approx 3$. (c) Parametric and Raman gains at different pump powers with a fixed frequency shift ($a \approx 2$). Raman gain increases linearly with the pump power, while parametric gain can be a function of both the pump power and additional frequency shift. (d - f) Difference between the FWM and SRS gains in 2D-parameter space. The FWM (SRS) dominant region is filled with red (blue). Red (blue) dashed line represents zero gain for FWM (SRS). Horizontal dashed arrows indicate excitation pathways explored in upcoming sections. The difference between the FWM and SRS gains is normalized by loss (α) with the chosen additional frequency shifts of (d) $a = 1$, (e) $a = 2$, and (f) $a = 4$. Cases (i - vi) shows parameters analyzed in the following sections. Note b is assumed to be 1 in all calculations.

parametric gain is created at a small additional frequency shift ($a = 1$), maximized at a certain point ($a = 3$), and shrinks at a large frequency shift ($a = 5$). It may be found that a certain amount of additional frequency shift is required to overcome

the loss in the cavity, i.e., $g_{\text{cav}} > 0$. In addition, there can be FWM dominant regions over SRS for certain frequency shifts, i.e., $g_{\text{cav}} > g_{\text{R}} > 0$. Figure 4.1(c) presents the same gain curves as a function of detuning at a fixed frequency shift ($\Delta\omega = 2\kappa$) for different normalized powers. The Raman gain curves increase with pump power, while the parametric gain is bigger at $S = 6$ than other cases. SRS dominates over FWM at relatively high pump powers; however, under a proper frequency shift condition it is possible that FWM can overcome SRS at relatively low pump power. A direct comparison between parametric and Raman gain is shown in two-dimensional parameter space at different additional frequency shifts in Figures 4.1(d - f). The red (blue)-colored region represents the larger parametric (Raman) gain region. The Raman gain (blue dashed region) remains the same, while the parametric gain (red dashed region) region gets bigger as a function of the additional frequency shift, but shrinks after a maximum point.

4.3 Numerical model

The intracavity field of the microsresonator can be modeled by the well-known Lugiato-Lefever equation (LLE) as follows [66, 109, 121]:

$$t_R \frac{\partial E}{\partial t} = -(\alpha + i\delta_0)E + \sqrt{\theta}E_{in} - i\frac{\beta_2 L}{2}\frac{\partial^2}{\partial \tau^2}E + i\gamma L(1 - f_{\text{R}})|E|^2 E + i\gamma L f_{\text{R}}(R * |E|^2)E \quad (4.5)$$

where $E(t, \tau)$ is the internal electric field within the resonator, t is the slow time describing the evolution of the field envelope, $\tau = t_R(\phi/\pi)$ is the fast time describing

the temporal profile of the field envelope, and ϕ is the azimuthal coordinate around the resonator. f_{R} is the fractional coefficient which determines the strength of the SRS term, and $*$ denotes the convolution. f_{R} is assumed 0.18 for silica [124]. $R(\tau)$ is the Raman response function

$$R(\tau) = \frac{\tau_1^2 + \tau_2^2}{\tau_1 \tau_2^2} \exp^{-\tau/\tau_2} \sin\left(\tau/\tau_1\right) \tag{4.6}$$

where $\tau_1 = 12.2$ fs and $\tau_2 = 32$ fs for fused-silica based fibers [124]. A complex dispersion profile of a microresonator without AMX can be described in the frequency domain as follows: $D_{\mathrm{int}} = \omega_\mu - (\omega_0 + D_1\mu) = \frac{1}{2}D_2\mu^2 + \ldots$, where D_{int} is the integrated dispersion, and ω_μ is the angular frequency of the relative mode number (μ) with respect to the pump mode ($\mu = 0$). Note that we ignore higher-order ($\beta_{i>2}$ or $D_{i>2}$) dispersion coefficients to simplify simulations and focus on effects of AMX and SRS. The integrated dispersion with the AMX effect may be simply expressed as [1]

$$D_{\mathrm{int}}(\mu, a, b) = \omega_\mu - (\omega_0 + D_1\mu) = \frac{1}{2}D_2\mu^2 - \frac{a\kappa/2}{\mu - b - 0.5} \tag{4.7}$$

where a and b determine the normalized amplitude and the location of the additional frequency shift. Note this model describes the dispersion for resonators with a strong intermodal coupling, while adding a single additional frequency shift for a specific mode number better describes resonators with a weak AMX [50, 126]. Then the LLE may be rewritten by taking the Fourier transform and the inverse Fourier transform

of the dispersion and Raman terms:

$$t_R\frac{\partial E}{\partial t} = -(\alpha + i\delta_0)E + \sqrt{\theta}E_{in} - i\mathcal{F}^{-1}\left[t_R D_{\text{int}} \cdot \mathcal{F}[E]\right] + i\gamma L(1-f_{\text{R}})|E|^2E + i\gamma L f_{\text{R}}(\mathcal{F}^{-1}\left[\mathcal{F}[R]\cdot\mathcal{F}[|E|^2]\right])E \quad (4.8)$$

where $\mathcal{F}$ and $\mathcal{F}^{-1}$ denote the Fourier transform and the inverse Fourier transform, respectively. The LLE is solved numerically using the split-step method where the nonlinear and dispersion contributions are treated separately [125].

We consider a silica microtoroid resonator with a radius of 250 μm at 780 nm for LLE simulations. The simulation parameters are set as follows: $D_1/2\pi = 130.4$ GHz, $D_2 = -5.72$ MHz, $Q_{\text{load}} = 1\times10^8$, $\alpha = t_R\omega_0/2Q_{\text{load}} = 9.25\times10^{-5}$, $\theta = 2.71\times10^{-5}$, $\gamma = 0.014$, and $S = 4$. The integrated dispersion with a AMX, $D_{\text{int}}(\mu, a = 8, b = 3)$, is shown in figure 4.2(a). The normalized detuning is linearly increased over time from -2 to 14 to scan the resonance from the blue-detuned side to the red-detuned side which is usually done in real experimental situations. The corresponding average intracavity power is shown in Figure 4.2(b). The spectral evolution of the intracavity field is shown in Figure 4.2(c). The spectral and temporal profile are plotted in Figure 4.2(d) at different detuning values which are indicated as vertical dashed lines in Figures 4.2(b) and (c). Unlike its counterpart bright soliton where 'step-like' patterns indicate transition to soliton states in the effectively red detuned side [13, 55], dark solitons can be accessed in the effectively blue detuned side [50, 44, 84]. Dark soliton states can be determined by their temporal profiles which indicate pulse-like patterns.

As discussed in section 4.2, the AMX effect may generate parametric gain. Here

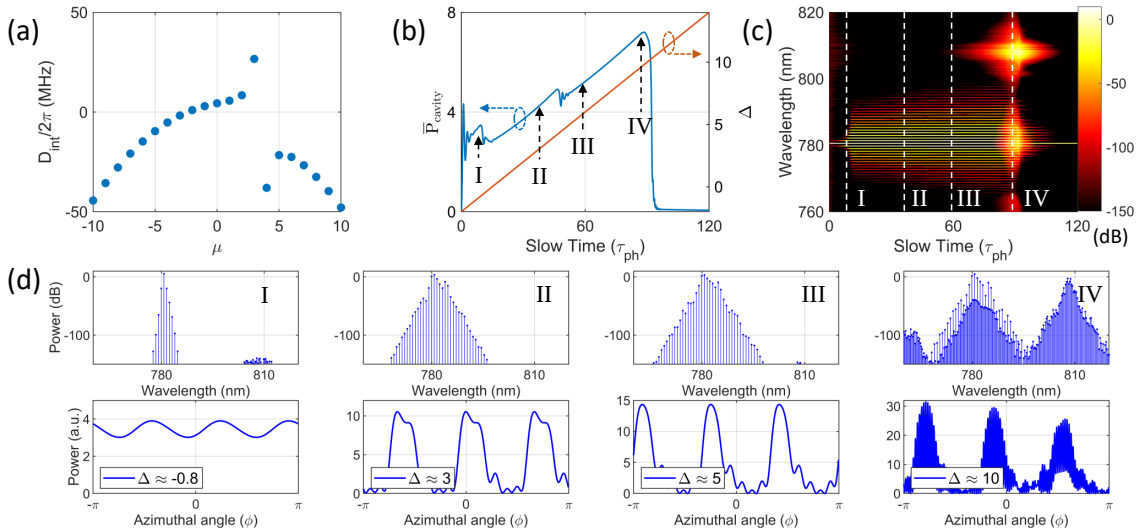

Figure 4.2: Excitation of dark soliton and SRS. (a) The integrated dispersion with an AMX ($a = 8, b = 3$) based on equation (4.7). (b) The averaged intracavity power (blue) and detuning (orange) as a function of time. The normalized pump power is set to 4. (c) The spectral evolution of the intracavity power. (d) The spectrum and temporal profile at the stages marked in (b). Four stages are chosen at different detuning values. A 'Turing' pattern appears at stage I. Solitons are generated as shown at stages II and III. SRS is excited when the intracavity power reaches the threshold intracavity power at stage IV.

we focus on the excitation pathway corresponding to case (**ii**) as labeled in Figure 4.1(e). In this case, it is expected that the FWM process is dominant over the SRS process because the parametric gain is bigger than the Raman gain. But as Δ increases, the intracavity power also increases and generates strong Raman gain along with the parametric gain. Thus, some complex interaction or competition between them may be expected. At stage I in Figure 4.2(d), it is shown that FWM comb can be initiated and leads to a Turing pattern [50, 44]. The first sideband location coincides with the AMX location (here, $\mu = b = 3$) [45]. As the pump wavelength increases, the bandwidth of the comb increases and a 'step-like' pattern in the blue-detuned side is observed indicating a transition to a coherent state as

reported in [50, 44, 127]. Localized structures in the cavity are observed as the detuning is increased (stages II and III in Figure 4.2(d)). The number of localized structures is equivalent to the AMX location. We also observed that the number of low intensity oscillations at the dark pulse profiles increases at a function of the detuning (i.e., 4 and 5 oscillations at $\Delta = 3$ and 5, respectively) as it is predicted theoretically [128, 129] and verified experimentally [50, 44]. At a large detuning, the intracavity power is high enough to initiate SRS and the Raman oscillation gets dominant (stage IV in Figure 4.2(d)). Note that the SRS gets dominant at a lower intracavity power for a large f_{R}.

4.4 Results and discussions

4.4.1 Influence of AMX on dynamics of dark soliton generation

While suppressing the AMX may simplify and help the excitation of bright solitons in anomalous-dispersion microresonators [1], AMX is required to soft-excite a FWM comb [41] and may lead to dark soliton states in normal-dispersion microresonators [45, 50]. We study three cases (corresponding to cases (**i**), (**ii**), and (**iii**) as labeled in Figures 4.1(d), (e), and (f), respectively) where different excitation dynamics of both the dark soliton and SRS are expected in each case. Again the Raman gain is not dependent on the AMX, while the amplitude and bandwidth of the parametric gain are dependent on the magnitude and location of the AMX as shown in Figure 4.1(b). The first case (**i**) shows the parametric gain is not enough to overcome the Raman gain and the Raman oscillation is a dominant effect. The second case (**ii**) is where the parametric gain is bigger than the Raman gain and

the FWM is the dominant process, but there may be a gain competition as the intracavity power grows. More complex dynamics is observed as in case (**iii**) where the parametric gain envelope shrink compared to the previous case.

The normalized coefficient (a) for the integrated dispersion, $D_{\text{int}}(\mu, a, b)$, is chosen to be 4, 8, and 16 for cases (**i**), (**ii**), and (**iii**) at the fixed location $b = 3$, respectively, as shown in Figure 4.3(a). The normalized detuning is increased from -2 to 14. The averaged intracavity power is shown in Figure 4.3(b) for each case. The spectral evolution profiles are shown in Figure 4.3(c). In case the parametric gain is high and wide, FWM may be effectively excited even though Raman gain is present and solitons can be generated (case (**ii**) in Figure 4.3(c)). In other words, because nonlinear frequency conversion (here, FWM) consumes the intracavity power, it is required to further increase the detuning to reach the threshold intracavity power for the SRS, yielding a large existence range for the soliton. The spectrum and temporal profile are also shown which confirms three pulses in the cavity. However as the parametric gain gets lower and narrower, FWM may be dominant over SRS for relatively limited conditions or cannot be excited (cases (**i**) and (**iii**) in Figure 4.3(c)). Then, SRS may be excited easily and a complex interaction between them can occur which often leads to a chaotic temporal profile with Raman oscillation.

It is critical to introduce an appropriate AMX to access the dark soliton regime. The location can be chosen simply by changing the wavelength of the pump source. The amplitude of the frequency shift may be tuned by indirectly an auxiliary resonator with a microheater [46, 61, 84], directly controlling the temperature of a cavity with a high thermo-optic coefficient [130], or through coupling an auxiliary light into a resonance [131]. It is worth mentioning that an oscillatory behavior in

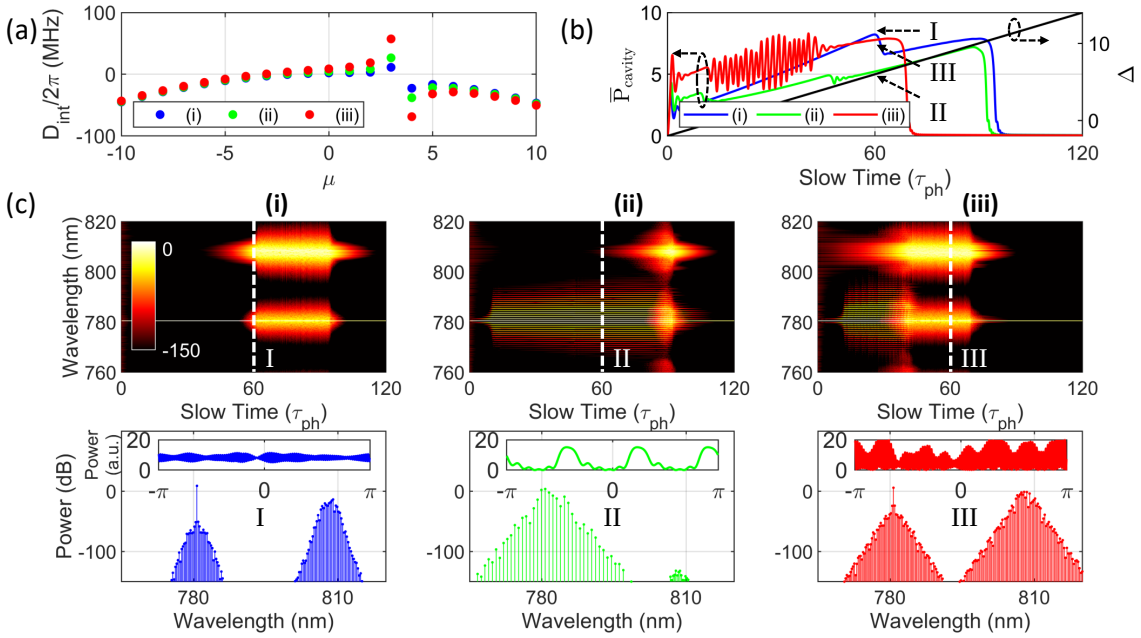

Figure 4.3: Excitation dynamics of a dark soliton and SRS at different AMX conditions. (a) The integrated dispersion with an AMX based on equation (4.7). Parameters for the AMX are $a = 4, 8, 16$ for case (i), (ii), (iii), respectively, and $b = 3$ for all cases. (b) The averaged intracavity power for cases (i) (blue), (ii) (green), (iii) (red) and detuning (black) as a function of time. (c) Spectral evolution of the intracavity fields (top), a representative spectrum (bottom), and temporal waveform (inset) for each case. Different AMX conditions yield different accessible states (either dark soliton or SRS dominant state). Too small or too large AMX strength reduces the dark soliton state region as shown in cases (i) and (iii) compared to a proper AMX condition in case (ii).

the intracavity power for case (**iii**) is shown in red in Figure 4.3(b) which may be interpreted as a dark breather [132, 126].

4.4.2 Influence of pump power on dynamics of dark soliton generation

As the Raman gain does not depend on the AMX as discussed in previous sections, there is a threshold power for SRS regardless of the AMX condition. However the threshold power for FWM is contingent on the AMX effects. In fact, the threshold

power for the parametric oscillation can be lower than the threshold power for the Raman oscillation. In this case, the dark soliton regime can be accessed by pumping the cavity with the power between the two threshold powers. As seen in Figure 4.1(a) the parametric gain is in the shape of a semi-ellipse and has a certain existence range as a function of the power, while the Raman gain increases linearly with the intracavity power. This implies that although the Raman effect may be dominant at high pump power, we may find a FWM dominant region at relatively low pump power.

The parameters a and b for the dispersion profile are fixed to 8 and 3, respectively, to focus on the effects of power. We chose three different normalized pump powers (S = 3, 5, and 7) for simulations as shown for cases (**iv**), (**v**), and (**vi**) in Figure 4.4(c) while keeping the other parameters the same, respectively. As shown in Figure 4.1(e), we examine three cases: a FWM dominant case (**iv**), an intermediate case (**v**), and a SRS dominant case (**vi**). Provided that the pump power is below the SRS threshold but above the FWM threshold power, a dark soliton state can be accessed for a range of detuning conditions with no observation of the SRS effect, as shown for case (**iv**) in Figure 4.4(c). Once the pump power is above the SRS threshold power, SRS can be excited as the intracavity power increases and eventually the system will go to a chaotic state, as shown in Figure 4.4(c) for case (**v**). As the pump power gets higher, SRS will be excited at low detuning values and the soliton state cannot be accessed, as shown in Figure 4.4(c) for case (**vi**). Note that a Raman comb can be observed around 810 nm, but no evidence of pulse-like pattern can be found in this study [119].

In experimental situations, choosing an appropriate pump power and detuning is

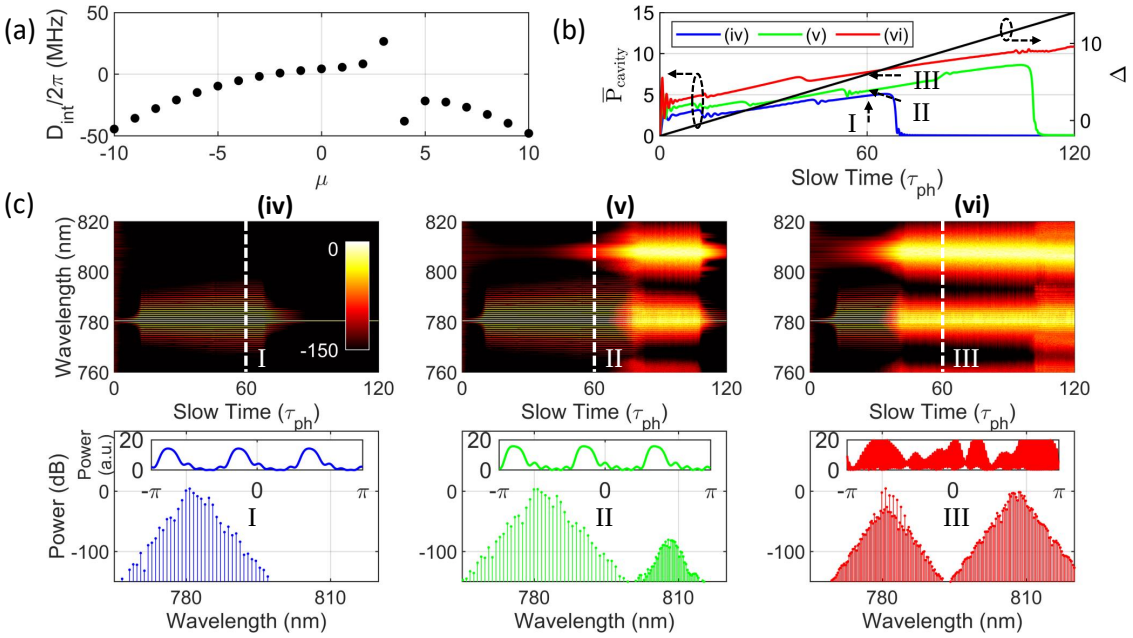

Figure 4.4: Excitation dynamics of a dark soliton and SRS at different pump powers. (a) The integrated dispersion with an AMX based on equation 4.7, $D_{\text{int}}(\mu, 8, 3)$, for all cases. (b) The averaged intracavity power for cases (iv) (blue), (v) (green), (vi) (red) and detuning (black) as a function of time. (c) Spectral evolution of the intracavity fields (top), a representative spectrum (bottom), and temporal waveform (inset) for each case. The dark soliton exists for a shorter detuning range at a higher pump power (stages II and III). In other words, increasing pump power is not always beneficial in accessing a dark soliton state.

highly desired to effectively suppress SRS and generate a dark soliton only. However, depending on the AMX condition, it may never be possible to initiate the FWM effect via the mode-interaction-aided parametric gain (Figure 4.3). In case the modal coupling condition cannot be controlled, increasing the threshold power for SRS or decreasing the threshold power for FWM may lead FWM to be a dominant process over SRS, which is demonstrated via a chemical method [133] or by adjusting the coupling condition between the cavity and the waveguide [16, 106]. While no dark breather is observed in this case, a large AMX strength may excite the breather

state [126].

4.4.3 Stability charts

Because there are two important parameters, the detuning and the pump power, different excited states of the system may be plotted in a two-dimensional parameter plane at different modal coupling conditions. As we are only interested in soliton states, the existence region of the soliton can be marked in the plane, which is called a stability chart. This can give us insights on the dark soliton existence and experimental guidelines. To analyze the stability of soliton states for a certain detuning and pump power, the intracavity field is propagated using the LLE. For a fixed pump power, the detuning is increased from -1 to 12 in a discrete step of 0.1 [134]. In each step, we allowed enough time (here, 30 τ_{ph}) for the field to pass transitory behavior from a sudden detuning increase and converge to a solution. We recorded the evolution of the field for another period of time (here, 20 τ_{ph}). Then, this process is repeated for a different pump power. A soliton state is found if the intracavity field of the frequency comb remains constant for the recorded period of time. If Raman lasing occurs, the state is labeled as a SRS state. Although a dark soliton state can be present in the presence of Raman lasing, we exclude this scenario for simplicity as it quickly collapses into a chaotic state as shown in Figure 4.3(c).

Figure 4.5 shows regions of stable soliton states (blue and red) and SRS states (green) at different AMX conditions. The AMX location (b) is fixed to 1 and the strength (a) is set to 1, 2, and 4 for the stability analysis which are shown in Figures 4.5(a), (b), and (c), respectively. The dark soliton existence region without the Raman interaction is red-colored. The green region represents the presence of

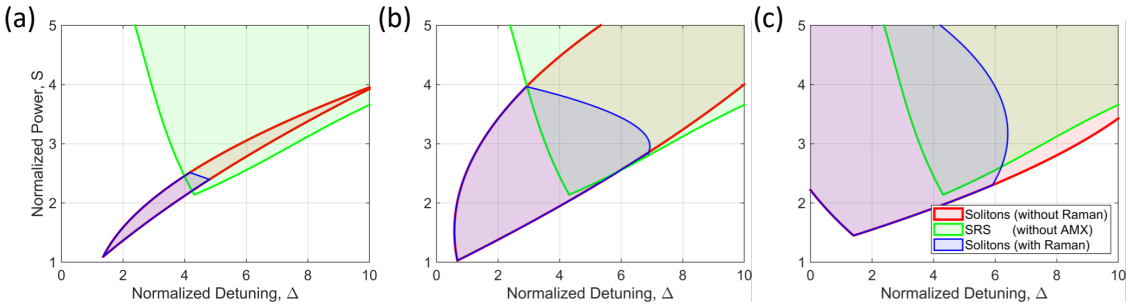

Figure 4.5: Simulated stability chart for different additional frequency shift values. (a - c) The blue region represents the existence range of dark soliton states in the presence of the Raman interaction ($f_R = 0.18$) for various additional frequency shift values of (a) $a = 1$, (b) $a = 2$, (c) $a = 4$. The red region where dark soliton states exist in the absence of the Raman interaction ($f_R = 0$) and the green region where SRS is excited in the absence of the additional frequency shift are shown for comparison. The existence range for dark soliton states with the Raman interaction (blue) is narrower than the one without the Raman interaction (red). The blue region increases along with the additional frequency shift, but decrease after its maximum value (not shown here).

the Raman lasing without the modal coupling. Finally, the blue region describes the existence of dark soliton states with the Raman interaction for an AMX condition. When the AMX is relatively small ($a = 1$), the existence range of soliton states is narrow without the Raman effect (red) and gets narrower with the effect in the normal dispersion regime (blue), which agrees well with literature [132, 128, 129, 121]. Interestingly, when the AMX strength is relatively large ($a = 2, 4$), the stable region becomes bigger and even compatible with the region in anomalous dispersion regime. As shown in Figure 4.1, a relatively large AMX strength can introduce a bigger parametric gain region which yields a wider region of soliton states. Thus, it is desired to introduce a relatively significant AMX-induced frequency shift to expand the stable region of the soliton states. Then, we can choose an appropriate pump power and detuning based on the stability chart.

In practice, unfortunately, it is not trivial to introduce a large modal coupling and control it in a single microresonator. While it is demonstrated that the AMX effects can be controlled by employing a main and an auxiliary microresonators (or coupled microresonators) in an integrated platform [47, 84, 135], the coupled microresonators may not be easily employed in WGM-type resonators due to difficulties in fabrication. It might be desired that indirectly controlling the temperature of the cavity without the additional cavity through an auxiliary light [131]. In experiments, the mode structure of a microresonator has to at first be characterized using dispersion measurement techniques [32]. Then, the AMX effect might need to be controlled based on the stability charts. This will give the desired input power and detuning values. Once a dark soliton is accessed, it will remain stable as long as the other parameters are kept constant such as temperature, detuning, and power [44, 83]. Feedback control of these parameters can assist in ensuring long-term stability.

4.5 Conclusion

The interaction of FWM based parametric process and SRS process is investigated in a normal-dispersion microresonator at near-visible wavelengths. The phase matching requirement for the parametric process is satisfied by an additional phase shift due to the additional frequency shift caused by an intermodal interaction. It is shown that parametric gain can be created by the additional phase shift. Meanwhile, Raman gain is inversely proportional to wavelength, which makes the competition between the parametric and Raman oscillation more complex at shorter wavelengths. Nonetheless, it is found that a significant phase shift can expand and

increase the parametric gain envelope which can overcome the Raman gain even at shorter wavelengths. The dynamics of dark soliton generation is analyzed by solving the LLE numerically at various pump powers and modal coupling conditions. The additional frequency shift can excite a dark soliton and extend the existence range, but too large of a frequency shift induces an oscillatory state (or breather) and shrinks the range. The stable region for dark solitons at various pump powers and detuning conditions is summarized in stability charts.

We believe this work can provide practical experiment guidelines for AMX based dark soliton generation in systems where the Raman gain is broad and large as well as fundamental insights on the AMX effect. Being able to control the AMX condition arbitrarily in a single microresonator (e.g., through temperature control of the cavity) may guarantee dark soliton existence in any microresonator without requiring an auxiliary microresonator, pump modulation, or self-injection-locking.

CHAPTER 5

Summary and Outlook

To summarize, we have generated optical frequency combs in water using a microtoroid resonator with an avoided mode crossing (AMX) approach. This demonstrates that a single optical resonator can function as a spectrometer and a biosensor without additional structures. Further improvements, such as using a PDH locking mechanism, enhancing mechanical stability, and controlling temperature, may result in a broadband and low phase noise frequency comb or dark soliton. We also investigated AMXs in air and found that intermodal coupling strength may determine the primary comb line location. A broadband optical frequency comb spanning a wide wavelength range was generated in air with the help of a strong AMX.

Furthermore, this thesis investigates the interaction between the four-wave mixing (FWM) based parametric process and stimulated Raman scattering (SRS) process in a normal-dispersion microresonator at near-visible wavelengths. The competition between parametric and Raman oscillation is complex at shorter wavelengths due to the inverse proportionality of Raman gain to wavelength. However, it is found that a significant phase shift can expand and increase the parametric gain envelope, overcoming the Raman gain even at shorter wavelengths. The dynamics of dark soliton generation are analyzed numerically, and it is observed that the additional frequency shift can excite dark solitons and extend their existence range. Stability charts are summarized to identify the stable regions for dark solitons at

various pump powers and detuning conditions.

This study presents practical guidelines for dark soliton generation based on the AMX effect and suggests controlling the AMX condition in a single microresonator for guaranteed dark soliton existence. Additionally, it proposes a promising approach for developing a multi-functional photonic device capable of detecting and identifying single molecules in gas and liquid environments and provides fundamental insights into the AMX effect and its potential applications in microresonator-based devices.

Overall, our findings represent a significant advancement towards label-free, single-molecule spectroscopy in both air and liquid environments, with potential applications in medical diagnostics and scientific research. So, this could be a groundbreaking approach to overcome current limitations in single molecule detection and identification without the need for labels or capture probes. With further research and development, our approach has the potential to revolutionize biosensing and open up new possibilities in various fields. Further studies are needed to fully understand and optimize this approach for practical applications. However, our results provide a promising foundation for future research in this area. We hope that our work will inspire further exploration and advancement in the field of label-free, single-molecule spectroscopy.

APPENDIX A

Modal Coupling Strength and Broadband Frequency Combs

Since a whispering gallery mode toroid resonator can support more than ten optical modes, it may by expected that multiple AMXs can be present with respect to a pumping mode as shown in Fig. 2.4. Based on the LLE simulation, we investigated a competition for the four-wave mixing (FWM) process and the relationship between the intermodal coupling strength and the bandwidth of a frequency comb. Figure A.1(a) shows the integrated dispersion with a weak modal crossing ($a = \kappa/2$ and $b = 5$) and a stronger AMX ($a = 2\kappa$ and $b = 5$). Other simulation parameters are written in section 2.3 and fixed for all the simulations shown here. As shown in Fig. A.1(b), the weak modal crossing initiated sideband generation first and no sideband generation at the strong AMX location is observed. This may be understood as when an AMX location is far away from a pump, it requires more frequency shift to meet the phase-matching condition for the FWM process. Next, the coupling strength for the strong AMX increased by $a = 5\kappa$ [Fig. A.1(c)]. Then, the strong AMX met the phase-matching requirement and a comb was generated at both AMX locations. Finally, we increase the coupling strength for the strong AMX by $a = 10\kappa$ [Fig. A.1(e)]. Stronger modal coupling generated a broader frequency comb as shown in Fig A.1(f) [63].

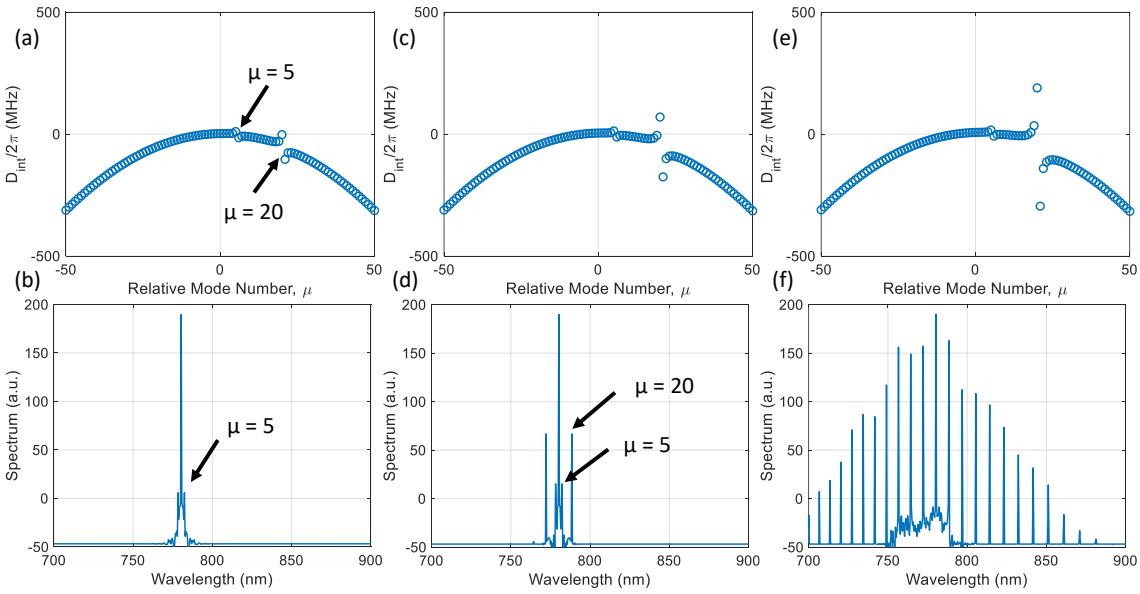

Figure A.1: (a, c, e) Integrated dispersion with a weak perturbation at $\mu = 5$ and a strong modal crossing at $\mu = 20$. Coupling strength increased from left to right for the strong modal crossing. (b, d, f) Simulated spectrum based on the integrated dispersion input from (a, c, e), respectively. A competition for the four-wave mixing process between weak and a strong modal couplings can be observed in (b) and (d). A broadband frequency comb is generated when the coupling strength is further increased as shown in (f).

APPENDIX B

Dispersion Measurement

In this appendix, a technique for measuring dispersion is discussed. The principles of a Mach-Zehnder interferometer are briefly explained, along with details of the experimental setup and measurement results.

B.1 Mach-Zehnder interferometer

Calibrating a tunable laser scan involves setting the wavelength scale of the laser to a known reference. This calibration is important for accurately measuring the wavelength of the laser output. The first step is to identify a stable and precise reference source that can be used to calibrate the laser scan. In this work, we use a fiber-based Mach-Zehnder interferometer.

Fiber-based Mach-Zehnder interferometer

A Mach-Zehnder interferometer (MZI) is an optical device that uses interference of light to measure changes in phase or amplitude. A fiber-based Mach-Zehnder interferometer (MZI) is a type of MZI that uses optical fibers as its main components.

The basic structure of a fiber-based MZI consists of a fiber optic splitter that divides an incoming optical signal into two paths, which then recombine at a second splitter to produce an interference pattern (figure B.1(b)). By adjusting the length

of one of the two fiber arms, the phase difference between the two paths can be tuned, allowing for the measurement of small changes in phase or amplitude.

Experimental setup

Figure B.1(a) depicts the experimental setup for the dispersion measurement. The tunable laser is scanned and splitted into two paths. One goes into the MZI and generates an interference pattern which is a sinusoidal oscillation (or fringes). The other passes the device under test, here, a fiber loop cavity. The fiber loop cavity (FLC) is made with a 50:50 fiber coupler by connecting one input with one output. Both of the light paths are monitored in photodetectors. The signals are collected with a DAQ system. A representative measurement is shown in figure B.1(c). The sinusoidal oscillation is observed with the MZI, while resonances are obtained with the FLC. Since the FSR of the MZI can be measured with a electrical spectrum analyzer, one can use this as a calibration signal. Then, the FSR of the FLC can be calculated.

B.2 Resonance linewidth measurement

In this next experiment, we substitute the FLC with a microtoroid resonator while keeping the rest of the setup the same. Figure B.2 shows the measurement of the Q factor. The laser scanning is calibrated using the MZI pattern, and a lorentzian curve is fitted to the resonance to estimate its full-width at half-maximum (FWHM). The loaded Q factor is then calculated by taking the ratio of the laser frequency to the FWHM. Chapter 1 provides more detailed information.

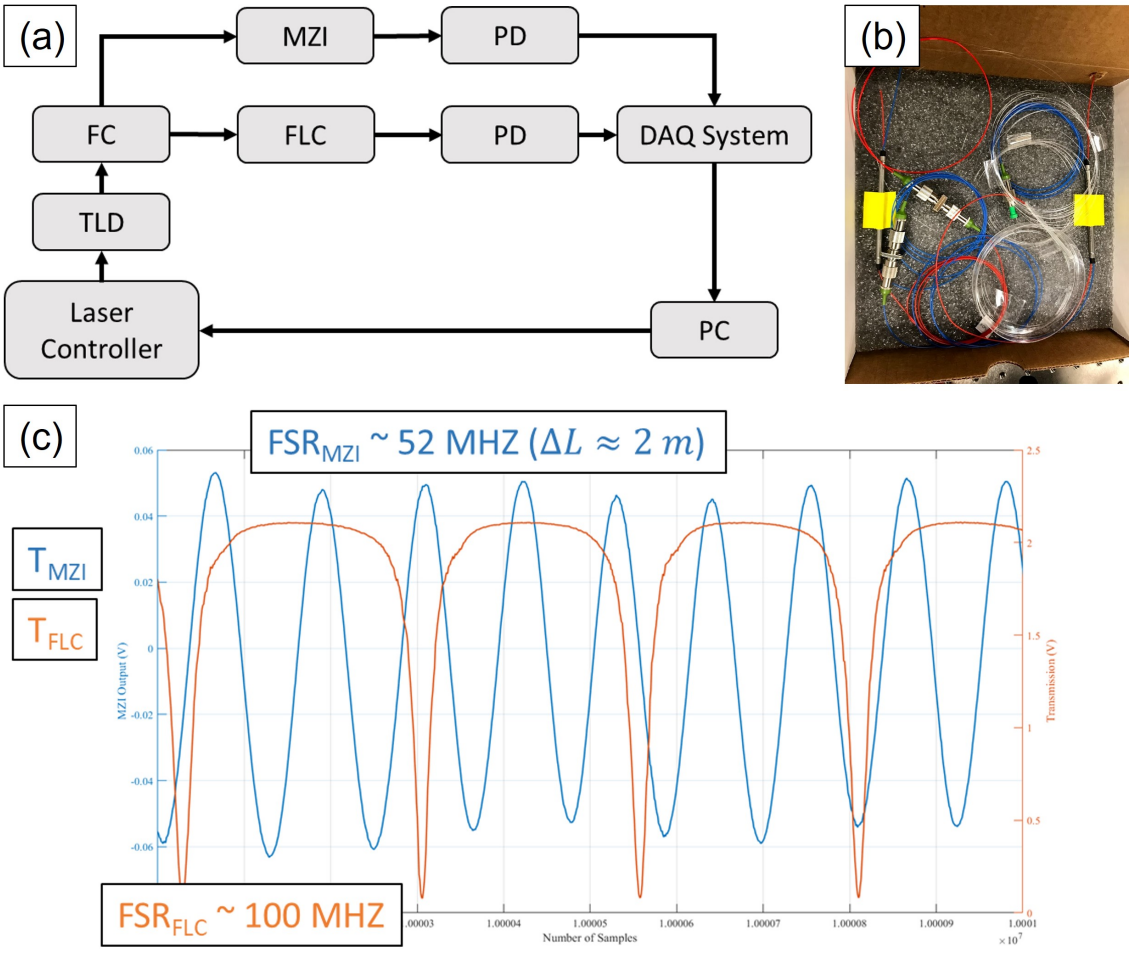

Figure B.1: Mach-Zehnder interferometer calibration setup. (a) The tunable laser is scanned and splitted into two paths. One goes through the MZI and the other passes the fiber loop cavity (FLC). And both of the signals are measured in a DAQ card. (b) The custom-built MZI in a enclosure. (c) The Resonances (Orange) from the FLC and interference patterns from the MZI are measured. The FSR of the FLC is calibrated based on the FSR of the MZI. TLD: tunable laser diode, FC: fiber coupler, MZI: Mach-Zehnder interferometer, FLC: fiber loop cavity, PD: photodiode, DAQ: data acquisition.

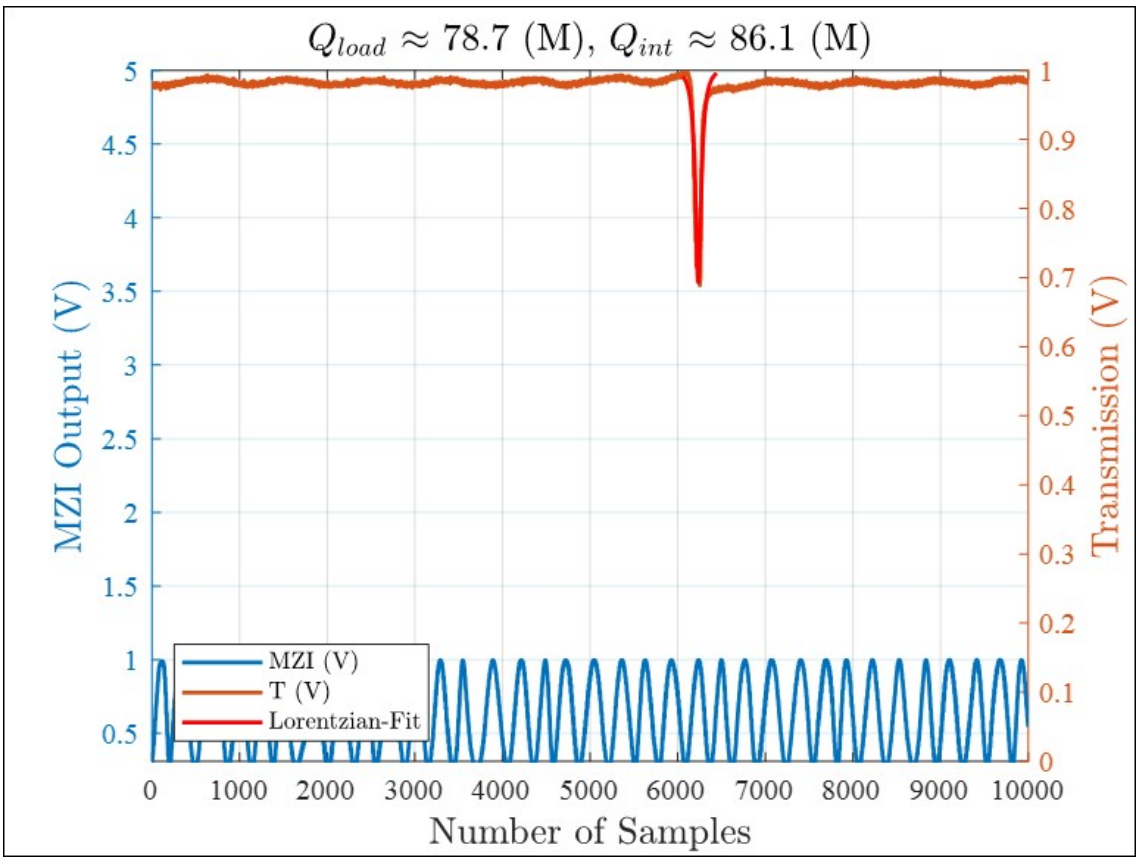

Figure B.2: Q factor measurement with a MZI. A resonance of a microcavity is shown in orange. A MZI pattern is shown in blue. Since the FSR of the MZI is known, the scan can be calibrated into frequency. A lorentzian curve is fitted on the resonance and the linewidth can be estimated. The loaded Q factor, then, can be calculated.

B.3 Dispersion characterization

Now that we covered the principles and examples of the MZI calibration and Q factor measurement, we are ready to apply the same technique for the dispersion measurement. Instead of measuring a single resonance, we increase the scanning range of the laser up to one FSR and repeat it. Figure B.3 illustrates measured transmission for multiple FSRs. Here, the x-axis represents one FSR and the whole scanning range is 9 FSRs. The blue rectangle highlights an intermodal interaction of two optical modes. The spacing between them changes over the scanning frequency. When they are close in frequency and interact each other, a pulling effect can be observed, also known as an avoided mode crossing (AMX) effect.

The AMX effect can be clearly visualized by plotting the integrated dispersion. Please see chapter 1 for more detail. Figure B.4 shows the integrated dispersion. The blue rectangle shows the AMX effect where a frequency difference between the adjacent modes are altered. If there is no AMX effect, we expect to observe a line where the frequency difference between the adjacent modes are nearly constant. However, in the blue rectangle region, a line is bent due to the AMX.

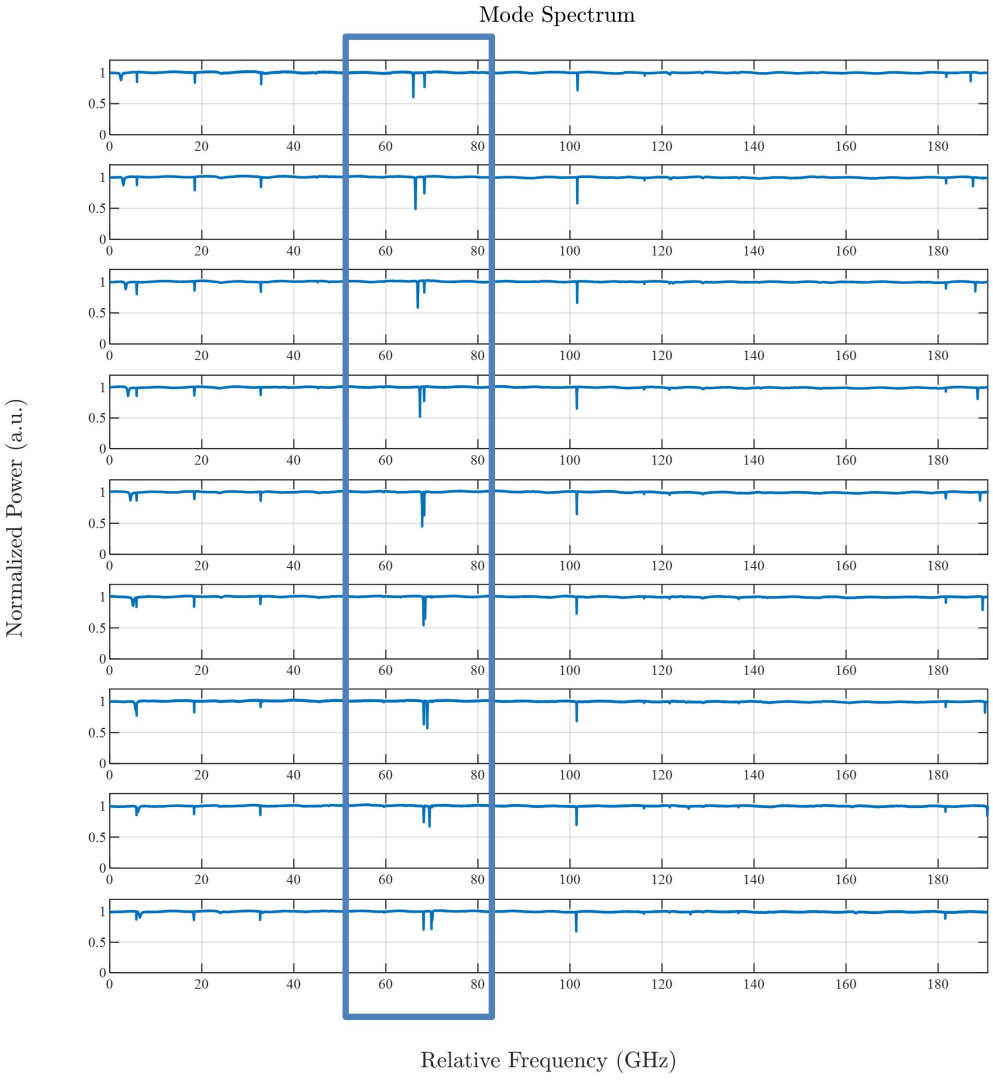

Figure B.3: Transmission spectrum of a microtoroid resonator. A tunable laser is scanned for one FSR of an optical mode, and repeated up to 9 FSRs. The transmission spectrum for each FSR is shown. The scanning frequency is calibrated with a MZI. The blue rectangle highlights two optical modes interacting each other and generating an AMX effect.

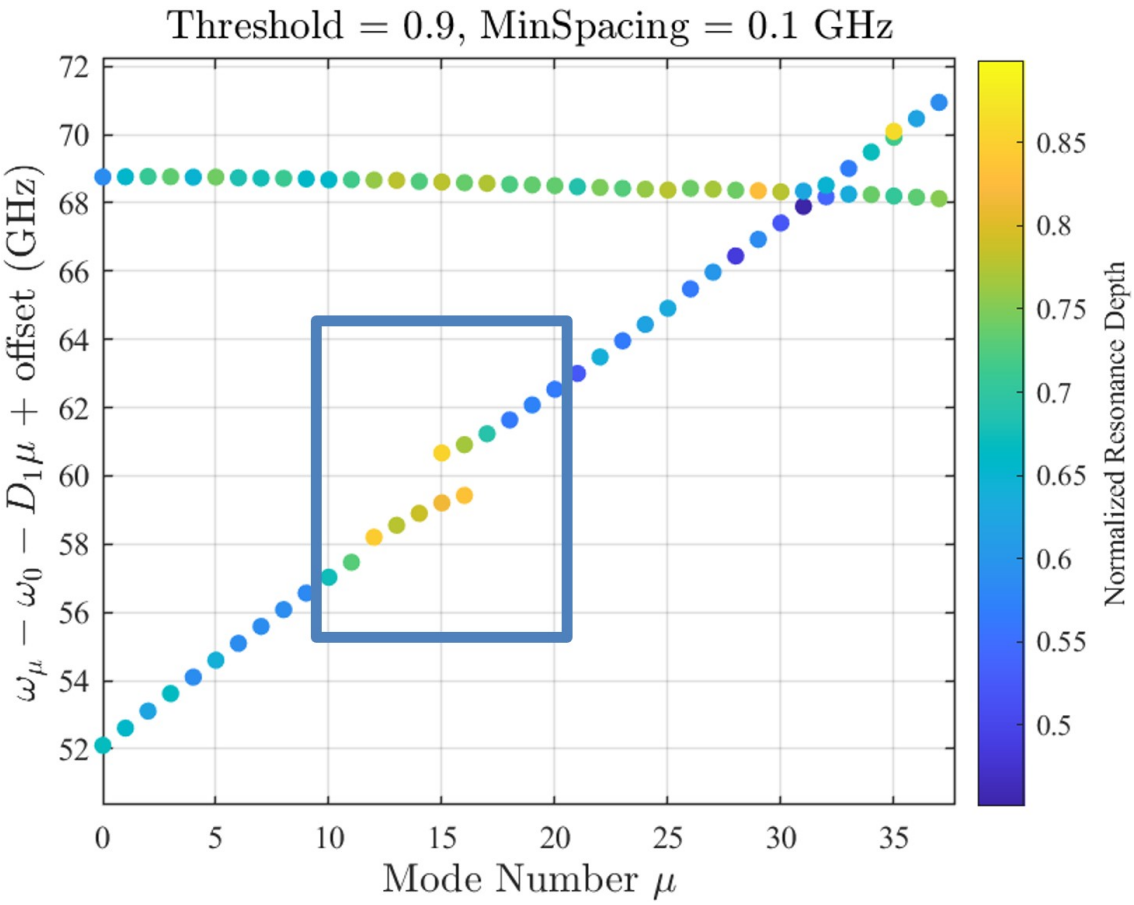

Figure B.4: Integrated dispersion of a microtoroid resonator. The y-axis represents the frequency difference between the the adjacent optical modes over the FSR. The mode number is a relative number. The thres

APPENDIX C

Matlab Codes

C.1 LLE simulation

main.m

```
% This code solves the LLE with the split-step method
% dE/dt' =
%           -(1+1i*Delta)*E + 1i*IFT[-tR/alpha*Dint*FT[E]] + F
% Reference: Phys. Rev. A 89, 063814 (2014) or Nat. Photon. 4, 471  476   (2010)
% Written by Gwangho Choi in Mar. 2022
% Modified from an example code in nonlinear fiber optics book

%---Specify input parameters
inputParams;

%---Sample numbers
nt = 2^9;                   % FFT Points
step_num = 2e5;             % Number of steps in time

%---Set variables
Delta    = detunArray(-2,14,0,1,step_num); % [Delta_initial,Delta_final,Detun_start,
    Detun_stop]
% Pin      = 0.02;                % [W]:          Driving Power
% s        = sqrt(Pin)*sqrt(gamma*L*theta/alpha^3);
s        = 5;                   % [-]:          Normalized Pump Field
S = ones(1,nt)*s;               % [-]:          Pump Field
Pin      = (s/sqrt(gamma*L*theta/alpha^3)).^2;                    % [W]:  Driving
    Power

%---Set simulation parameters
```

```
dp = 2*pi/nt;                % [-]: Sampling Resolution in polar coordinate
tMax = 120*tau_ph*1;           % [s]: Slow Time (default: 120*tau_ph)
t_prime = alpha*tMax/tR;     % [-]: Normalized Slow Time
dt = t_prime/step_num;       % [-]: Step Size in t (Slow Time)
% dt = 0.0005;

%---Define tau and omega arrays
p        = (-nt/2:nt/2-1)*dp;                    % Polar Coordinate Grid (a.u.)
mu       = fftshift(-nt/2:nt/2-1);               % Freq Array
t        = linspace(0,t_prime,step_num); % Slow Time Array (a.u.)
t_ns     = t*tR/alpha*1e9;                    % Slow Time Array (ns)
t_tR     = t*tR/alpha/tR;
f        = fftshift(mu)*FSR + om0/2/pi;
lam      = c./f;

%---Definition of Raman response function
R = ramanResponse(p, 12.2, 32, tR); % tau1 = 12.2; tau2 = 32; [fs]
fR       = 0.18;
% fR       = 0.245;
fR       = 0;

%---Input field profile
P_noise = 1e-12;             % [W]: Noise Power (1 pW)
uu = sqrt(P_noise) * sqrt(gamma*L*theta/alpha^3) * (rand(1,nt));

%---Store dispersive phase shifts to speedup code
Dint = D2 / 2 .* mu.^2;
a = kappa*2;
% a = 0;
b = 1;
% Dint = Dint - a/2./(mu-b-0.5);
Dint = Dint + a * (mu == b);
Disp = tR * Dint / alpha;

% ********* [ Beginning of MAIN Loop] ***********
[sol, spec] = splitStep(Delta,S,uu,dt,nt,step_num,Disp,R,fR);
```

```
% ************ [ End of MAIN Loop ] *************
```

splitStep.m

```
function [sol, spec] = splitStep(Delta,S,uu,dt,nt,step_num,Disp,R,fR)
% ------
% uu: Initial Input
% Delta: Detuning
% dt: Time Step
% nt: Sampling Number
% step_num: Evolution Number
% Disp: Dint
% dp: sampling
% S: External Input
% R: Raman Response
% fR:
% ------
down = 1e2; % Downsample for less storage
dp = 2*pi/nt;
sol = zeros(nt,step_num/down);
sol(:,1) = uu;
% ********* [ Beginning of MAIN Loop] ***********
% Scheme: 1/2N -> D -> 1/2N; first half step nonlinear
temp = uu .* exp((1i*uu.*conj(uu)-1-1i*Delta(1)) * dt/2) + S*dt/2; % note dtau/2
for n = 1:step_num-1
    temp = ifft(temp);                                          % Convert to
        frequency domain
    f_temp = temp .* exp(-1i*Disp * dt);
    uu = fft(f_temp);                                           % Back to time
        domain

    P = uu.*conj(uu);
    convl = (nt*dp)*fft(ifft(R).*ifft(P));
    convl = fftshift(convl);                            % Convolution Term
```

```
    Nlin = 1i*((1-fR)*P + fR*convl) -1 -1i*Delta(n);
    temp = uu .* exp(Nlin * dt) + S.*dt;  % Nonlinear, detuning, dissipation, and
        pump in order
    if rem(n,down) == 0
        sol(:,n/down+1) = temp;                              % Store time evolution
    end
end
% *************** [ End of MAIN Loop ] **************

% uu = temp; % Final field
% temp = fftshift(ifft(uu)); % Final spectrum
spec = fftshift(ifft(sol,[],1),1);
```

detunArray.m

```
function Delta = detunArray(Delta_initial,Delta_final,Detun_start,Detun_stop,
    step_num)
% Delta_initial   = -2;
% Delta_final     = 10;
% Detun_start     = .1;
% Detun_stop      = .9;
Delta_start     = linspace(Delta_initial,Delta_initial,step_num*Detun_start);
Delta_detun     = linspace(Delta_initial,Delta_final,round(step_num*(Detun_stop-
    Detun_start)));
Delta_stop      = linspace(Delta_final,Delta_final,round(step_num*(1-Detun_stop)));
Delta           = cat(2,Delta_start,Delta_detun,Delta_stop);
```

ramanResponse.m

```
function R = ramanResponse(p, tau1, tau2, tR)
tauc = tR/2/pi*1e15;
eta = tauc*(tau1^2+tau2^2)/(tau1*tau2^2);
a = tauc/tau2;
b = tauc/tau1;
```

```
R = eta .* exp(-a.*p) .* sin(b.*p);
R = heaviside(p).*R;
```

C.2 Dispersion characterization

main.m

```
[data_0,data_1,data_2,data_3,file_name] = read_tdms;

mrkrs = mzi_to_markers(data_2);
mzi_fsr0 = 40.1755e6;
mzi_fsr0 = 103.1773e6; % 2 m, 1050 nm
mzi_fsr0 = 39.934e6; % 2 m, 1050 nm
freq = mzi_to_freq(data_2,mrkrs,mzi_fsr0);

% Pick a peak number from the 'findpeaks' function.
idx_start = find_start_manual_user(data_1,data_2,data_3);
[ch_0,ch_1,ch_2,ch_3] = crop_data(data_0, data_1, data_2, data_3, idx_start, mrkrs(
    end));
freq = freq(idx_start-mrkrs(1)+1:end);

trans = detrend(ch_1);

fsr = fsr_manual_user(freq,trans);
```

read_tdms.m

```
function [data_0,data_1,data_2,data_3,file_name] = read_tdms
current_dir = cd;
[file_name,path_name] = uigetfile('*.tdms','Select the datafile(s)',current_dir);
tdms_file_name = fullfile(path_name,file_name);
temp = tdmsread(tdms_file_name); % Now use this function...
temp = temp{1};
data_0 = table2array(temp(:,1));
```

```
data_1 = table2array(temp(:,2));
data_2 = table2array(temp(:,3));
data_3 = table2array(temp(:,4));
end
```

mzi_to_markers.m

```
function result = mzi_to_markers(data)
tic;
% (1): Normalize the MZI (-1 to 1)

mzi = detrend(data)*2 - 1;

% (2): Find zero-crossings
%    : Could be many crossings due to noisy signals
signchange_x = find(diff(sign(mzi))) + 1;
signchange_y = mzi(signchange_x);

% figure; plot(mzi); hold on; plot(signchange_x,signchange_y,'o'); hold off

% Delete zeros. Only find (+) <-> (-) sign changes.
zers = (signchange_y == 0);
signchange_y(zers) = [];
signchange_x(zers) = [];

% (3): Find a peak larger than a value between crossings.
%    : If no peak found, search for next crossing
idx_down = zeros(1,length(signchange_x)-1);
idx_up = zeros(1,length(signchange_x)-1);
% Split data into pieces between the zero crossings
len = length(signchange_x)-1;
mzi_cell = cell(1,len);
for i = 1:length(signchange_x)-1
    idx_down(i) = signchange_x(i);
    idx_up(i) = signchange_x(i+1);
```

```
    mzi_cell{:,i} = mzi(idx_down(i):idx_up(i))';
end
[tmp,I] = cellfun(@max,mzi_cell); % Find max for each piece
I = I+idx_down-1;
result = I(tmp>0.7);

h = figure; plot(mzi); hold on; plot(result,mzi(result),'o'); hold off;

fprintf('Finding "Markers" takes %.2f seconds.\n', toc);
fprintf('Paused... Press Enter to Start...\n');
pause;
close(h);
end
```

detrend.m

```
[up,~] = envelope(data,1e5,'peak');
result = data./up;
```

mzi_to_freq.m

```
function freq = mzi_to_freq(mzi,mrkrs,fsr0)
fprintf('Calibration started...\n');
% Dispersion coefficients. Details can be found in powerpoint slides.
d1 = -9.8646e-3;
d2 = 2*0.10044e-9;
d1 = - 436.6658e-3; % [Hz]: @ 1050 nm
d2 = 2 * 106.0284e-9; % [Hz]: @ 1050 nm
% d1 = 0;
% d2 = 0;
d3 = 0;

len = length(mrkrs); % number of markers
```

```
% 1. Throw data away before the first marker and after the last marker.
idx_low = mrkrs(1);
idx_high = mrkrs(len);

% mzi = mzi(idx_low:idx_high);
freq = zeros(1,idx_high-idx_low+1);
mu = 1:len;
mu0 = floor(len/2); % Roughly at the mode at the center
mu = mu-mu0;% Relative mode number

% Spline Fitting
%%{
t_start = tic;
k = len-1;
t_fit = zeros(1,k);
t_fit_2 = zeros(1,k);
t_fit_3 = zeros(1,k);
t_asin = zeros(1,k);
t_acos = zeros(1,k);

for i = 1:len-1
% for i = 1e5:1e5+2
fsr = fsr0 + d1*mu(i) + d2/2*mu(i)^2 + d3/factorial(3)*mu(i)^3;
x = 1:(mrkrs(i+1)-mrkrs(i)+1);
y = mzi(mrkrs(i):mrkrs(i+1));
xx = linspace(1,x(end),15); % 10 or 15 or 20 points

tic
yy = spline(x,y,xx);
% yy = makima(x,y,xx);
t_fit(i) = toc;
tic
pp = spline(xx,[0 yy 0]);
% pp = makima(xx,yy);
t_fit_2(i) = toc;
tic
```

```
yyy = ppval(pp,x);
t_fit_3(i) = toc;



temp_len = length(yyy);
temp_min = min(yyy);
temp_idx = find(yyy == temp_min, 1, 'first');
yyy_dn = yyy(1:temp_idx);
temp_max = max(yyy_dn);
yyy_dn_norm = ((yyy_dn - temp_min)/(temp_max - temp_min)-0.5)*2;

if i == 1
    idx_prev = 1;
else
    idx_prev = mrkrs(i)-mrkrs(1)+1; % Remember index for the previous loop
end
tic
for j = 1:temp_idx-1
    df = fsr/2/pi*(acos(yyy_dn_norm(j+1))-acos(yyy_dn_norm(j)));
    freq(j + idx_prev) = freq(j + idx_prev - 1) + df;
end
t_acos(i) = toc;
yyy_up = yyy(temp_idx:temp_len);
temp_min = min(yyy_up);
temp_max = max(yyy_up);
yyy_up_norm = ((yyy_up - temp_min)/(temp_max - temp_min)-0.5)*2;
tic
for j = 1:temp_len-temp_idx
    df = fsr/2/pi*(asin(yyy_up_norm(j+1))-asin(yyy_up_norm(j)));
    temp_idx_up = j + temp_idx - 1;
    freq(temp_idx_up + idx_prev) = freq(temp_idx_up + idx_prev - 1) + df;
end
t_asin(i) = toc;
% figure; plot(x,y,xx,yy,x,yyy);
% figure; plot(freq(idx_prev+1:idx_prev+temp_len),yyy);
```

```
end
t_sum_fit = sum(t_fit);
t_sum_fit_2 = sum(t_fit_2);
t_sum_fit_3 = sum(t_fit_3);
t_sum_acos = sum(t_acos);
t_sum_asin = sum(t_asin);
% temp = freq(mrkrs(1e5)-mrkrs(1): mrkrs(1e5+3)-mrkrs(1));
tEnd = toc(t_start);
%}
fprintf('Calibrating "Markers" takes %.2f seconds.\n', tEnd);
end
```

find_start_manual_user.m

```
function idx_start = find_start_manual_user(data_1,data_2,data_3)
% 1: Find the first a few resonances of the FLC
% 1-1: Crop the first 1 M data
num = 2e6;
crop_1 = data_1(1:num); % Transmission
crop_2 = data_2(1:num); % MZI
crop_3 = data_3(1:num); % FLC. Note: use 125 kHz detector for minus values.
% 1-2: Find the resonances of the FLC.
% 1-2-1: Find max and min values
% crop_3_max = max(crop_3);
% crop_3_min = min(crop_3);
% 1-2-2: Find peaks with a high prominence and minus value.
% thres = (crop_3_max - crop_3_min)*.8; % 80% is an arbitrary number. Note: this
    didn't work if the max is falsely big
thres = mean(crop_3);
[pks_y,pks_x,~,~] = findpeaks(-crop_3,...
    'Threshold',0,'MinPeakProminence',thres/2,'MinPeakDistance',1e3);
pks_y = -pks_y;
% 1-2-3: Visualization
h = figure; hold on;
plot(crop_3,'b-');
```

```
plot(crop_1,'r-');
plot(crop_2,'g-');
plot(pks_x,pks_y,'ko');
text(pks_x,pks_y-0.02,num2str((1:numel(pks_x))'))
% 2: Find the second resonance, because the first one may not be stable.
answer = inputdlg('Choose a number for a FLC resonacne','Input',1,{'2'});
idx = str2double(answer{1});
idx_start = pks_x(idx);
close(h);
end
```

crop_data.m

```
function [ch_0,ch_1,ch_2,ch_3] = crop_data(data_0, data_1, data_2, data_3,
    idx_start, idx_end)
% len = length(data_0);

ch_0 = data_0(idx_start:idx_end);
ch_1 = data_1(idx_start:idx_end);
ch_2 = data_2(idx_start:idx_end);
ch_3 = data_3(idx_start:idx_end);

end
```

fsr_manual_user.m

```
function fsr = fsr_manual_user(freq,trans)
% We don't need the whole data.
% Let's focus on 10 milion data
n = 10e6;
freq = freq(1:n);
trans = trans(1:n);
[pks_y,pks_x,~,~] = findpeaks(-trans,...
    'Threshold',0,'MinPeakProminence',0.2,'MinPeakDistance',1);
```

```
% findpeaks(-trans,freq,...
%     'MinPeakHeight',-thresh,'MinPeakProminence',1-thresh,'MinPeakDistance',10);

pks_y = -pks_y;
h = figure; hold on;
plot(freq/1e9,trans);
% xlim(min(freq)/1e9*[1 1] + [0 1]);
% xlim([min(freq) max(freq)]/1e9);
xlim(min(freq)*[1 1]/1e9 + [0 400]);
plot(freq(pks_x)/1e9,pks_y,'ko');
text(freq(pks_x)/1e9,pks_y-0.02,num2str((1:numel(pks_x))'))



answer = inputdlg('Choose two peaks for the mode family (Put a space between the
    numbers)','Input',1,{'1 10'});
answer = str2num(answer{1});
idx_first = answer(1);
idx_second = answer(2);

freq_first = freq(pks_x(idx_first));
freq_second = freq(pks_x(idx_second));

fsr = freq_second - freq_first;

close(h);

end
```

REFERENCES

[1] T. Herr, V. Brasch, J.D. Jost, I. Mirgorodskiy, G. Lihachev, M.L. Gorodetsky, and T.J. Kippenberg. Mode Spectrum and Temporal Soliton Formation in Optical Microresonators. *Physical Review Letters*, 113(12):123901, September 2014.

[2] Cheng Li, Trevor Lohrey, Phuong-Diem Nguyen, Zhouyang Min, Yisha Tang, Chang Ge, Zachary P. Sercel, Euan McLeod, Brian M. Stoltz, and Judith Su. Part-per-Trillion Trace Selective Gas Detection Using Frequency Locked Whispering-Gallery Mode Microtoroids. *ACS Applied Materials & Interfaces*, 14(37):42430–42440, September 2022. Publisher: American Chemical Society.

[3] Gordon T. Luu, Chang Ge, Yisha Tang, Kailiang Li, Stephanie M. Cologna, Joanna E. Burdette, Judith Su, and Laura M. Sanchez. An integrated approach to protein discovery and detection from complex biofluids. preprint, Cancer Biology, January 2022.

[4] Lei Chen, Cheng Li, Yumin Liu, Judith Su, and Euan McLeod. Three-dimensional simulation of particle-induced mode splitting in large toroidal microresonators. *Sensors*, 20(18), 2020.

[5] Judith Su. Label-Free Biological and Chemical Sensing Using Whispering Gallery Mode Optical Resonators: Past, Present, and Future. *Sensors*, 17(3):540, March 2017.

[6] D. K. Armani, T. J. Kippenberg, S. M. Spillane, and K. J. Vahala. Ultra-high-Q toroid microcavity on a chip. *Nature*, 421(6926):925–928, February 2003.

[7] T. Lu, H. Lee, T. Chen, S. Herchak, J.-H. Kim, S. E. Fraser, R. C. Flagan, and K. Vahala. High sensitivity nanoparticle detection using optical microcavities. *Proceedings of the National Academy of Sciences*, 108(15):5976–5979, April 2011.

[8] Judith Su, Alexander FG Goldberg, and Brian M Stoltz. Label-free detection of single nanoparticles and biological molecules using microtoroid optical resonators. *Light: Science & Applications*, 5(1):e16001–e16001, January 2016.

[9] Hansuek Lee, Tong Chen, Jiang Li, Ki Youl Yang, Seokmin Jeon, Oskar Painter, and Kerry J. Vahala. Chemically etched ultrahigh-Q wedge-resonator on a silicon chip. *Nature Photonics*, 6(6):369–373, June 2012.

[10] Martin Hubert Peter Pfeiffer, Clemens Herkommer, Junqiu Liu, Tiago Morais, Michael Zervas, Michael Geiselmann, and Tobias J. Kippenberg. Photonic Damascene Process for Low-Loss, High-Confinement Silicon Nitride Waveguides. *IEEE Journal of Selected Topics in Quantum Electronics*, 24(4):1–11, July 2018.

[11] Yong Yang, Xuefeng Jiang, Sho Kasumie, Guangming Zhao, Linhua Xu, Jonathan M. Ward, Lan Yang, and Síle Nic Chormaic. Four-wave mixing parametric oscillation and frequency comb generation at visible wavelengths in a silica microbubble resonator. *Optics Letters*, 41(22):5266, November 2016.

[12] Tong Chen, Hansuek Lee, and Kerry J. Vahala. Thermal stress in silica-on-silicon disk resonators. *Applied Physics Letters*, 102(3):031113, January 2013.

[13] T. Herr, V. Brasch, J. D. Jost, C. Y. Wang, N. M. Kondratiev, M. L. Gorodetsky, and T. J. Kippenberg. Temporal solitons in optical microresonators. *Nature Photonics*, 8(2):145–152, February 2014.

[14] H. Guo, M. Karpov, E. Lucas, A. Kordts, M.H.P. Pfeiffer, V. Brasch, G. Lihachev, V.E. Lobanov, M.L. Gorodetsky, and T.J. Kippenberg. Universal dynamics and deterministic switching of dissipative Kerr solitons in optical microresonators. *Nature Physics*, 13(1):94–102, January 2017.

[15] Gwangho Choi, Adley Gin, and Judith Su. Optical frequency combs in aqueous and air environments at visible to near-IR wavelengths. *Optics Express*, 30(6):8690, March 2022.

[16] T. J. Kippenberg, S. M. Spillane, and K. J. Vahala. Kerr-Nonlinearity Optical Parametric Oscillation in an Ultrahigh- Q Toroid Microcavity. *Physical Review Letters*, 93(8):083904, August 2004.

[17] Tobias J. Kippenberg, Alexander L. Gaeta, Michal Lipson, and Michael L. Gorodetsky. Dissipative Kerr solitons in optical microresonators. *Science*, 361(6402):eaan8083, August 2018.

[18] Alexander L. Gaeta, Michal Lipson, and Tobias J. Kippenberg. Photonic-chip-based frequency combs. *Nature Photonics*, 13(3):158–169, March 2019.

[19] Erol Ozgur, Kara Ellen Roberts, Ekin Ozge Ozgur, Adley Nathanael Gin, Jaden Robert Bankhead, Zhikun Wang, and Judith Su. Ultrasensitive Detection of Human Chorionic Gonadotropin Using Frequency Locked Microtoroid Optical Resonators. *Analytical Chemistry*, 91(18):11872–11878, September 2019.

[20] Cheng Li, Lei Chen, Euan McLeod, and Judith Su. Dark mode plasmonic optical microcavity biochemical sensor. *Photonics Research*, 7(8):939, August 2019.

[21] Lei Chen, Cheng Li, Yu-Min Liu, Judith Su, and Euan McLeod. Simulating robust far-field coupling to traveling waves in large three-dimensional nanostructured high-Q microresonators. *Photonics Research*, 7(9):967, September 2019.

[22] Judith Su. Label-free Single Molecule Detection Using Microtoroid Optical Resonators. *Journal of Visualized Experiments*, (106):53180, December 2015.

[23] Phuong-Diem Nguyen, Xuanru Zhang, and Judith Su. One-Step Controlled Synthesis of Size-Tunable Toroidal Gold Particles for Biochemical Sensing. *ACS Appl. Nano Mater.*, 2(12):7839–7847, December 2019.

[24] Sartanee Suebka, Phuong-Diem Nguyen, Adley Gin, and Judith Su. How Fast It Can Stick: Visualizing Flow Delivery to Microtoroid Biosensors. *ACS Sensors*, page acssensors.1c00748, June 2021.

[25] Judith Su. Label-Free Single Exosome Detection Using Frequency-Locked Microtoroid Optical Resonators. *ACS Photonics*, 2(9):1241–1245, September 2015.

[26] Shuang Hao and Judith Su. Noise-Induced Limits of Detection in Frequency Locked Optical Microcavities. *Journal of Lightwave Technology*, 38(22):6393–6401, November 2020.

[27] Ian Coddington, Nathan Newbury, and William Swann. Dual-comb spectroscopy. *Optica*, 3(4):414, April 2016.

[28] Mengjie Yu, Yoshitomo Okawachi, Austin G. Griffith, Michal Lipson, and Alexander L. Gaeta. Microresonator-based high-resolution gas spectroscopy. *Optics Letters*, 42(21):4442–4445, November 2017. Publisher: Optical Society of America.

[29] Avik Dutt, Chaitanya Joshi, Xingchen Ji, Jaime Cardenas, Yoshitomo Okawachi, Kevin Luke, Alexander L. Gaeta, and Michal Lipson. On-chip dual-comb source for spectroscopy. *Science Advances*, 4(3):e1701858, March 2018.

[30] Nicolas Riesen, Wen Qi Zhang, and Tanya M. Monro. Dispersion analysis of whispering gallery mode microbubble resonators. *Optics Express*, 24(8):8832, April 2016.

[31] Nicolas Riesen, Wen Qi Zhang, and Tanya M. Monro. Dispersion in silica microbubble resonators. *Optics Letters*, 41(6):1257, March 2016.

[32] Shun Fujii and Takasumi Tanabe. Dispersion engineering and measurement of whispering gallery mode microresonator for Kerr frequency comb generation. *Nanophotonics*, 9(5):1087–1104, February 2020.

[33] Yun Zhao, Xingchen Ji, Bok Young Kim, Prathamesh S. Donvalkar, Jae K. Jang, Chaitanya Joshi, Mengjie Yu, Chaitali Joshi, Renato R. Domeneguetti, Felippe A. S. Barbosa, Paulo Nussenzveig, Yoshitomo Okawachi, Michal Lipson, and Alexander L. Gaeta. Visible nonlinear photonics via high-order-mode dispersion engineering. *Optica*, 7(2):135, February 2020.

[34] Jiyang Ma, Longfu Xiao, Jiaxin Gu, Hao Li, Xinyu Cheng, Guangqiang He, Xiaoshun Jiang, and Min Xiao. Visible Kerr comb generation in a high-Q silica microdisk resonator with a large wedge angle. *Photonics Research*, 7(5):573, May 2019.

[35] Renato R. Domeneguetti, Yun Zhao, Xingchen Ji, Marcelo Martinelli, Michal Lipson, Alexander L. Gaeta, and Paulo Nussenzveig. Parametric sideband generation in CMOS-compatible oscillators from visible to telecom wavelengths. *Optica*, 8(3):316, March 2021.

[36] Xueying Jin, Jing Wang, Mengyu Wang, Yongchao Dong, Fei Li, and Keyi Wang. Dispersion engineering of a microsphere via multi-layer coating. *Applied Optics*, 56(28):8023, October 2017.

[37] Mengyu Wang, Xueying Jin, Fei Li, Bolin Cai, and Keyi Wang. Whispering-gallery modes in a triple-layer-coated microsphere resonator for refractive index sensors. *Optics Communications*, 427:70–78, November 2018.

[38] Johann Riemensberger, Klaus Hartinger, Tobias Herr, Victor Brasch, Ronald Holzwarth, and Tobias J. Kippenberg. Dispersion engineering of thick high-Q silicon nitride ring-resonators via atomic layer deposition. *Optics Express*, 20(25):27661, December 2012.

[39] Nicolas Riesen, Shahraam Afshar V., Alexandre François, and Tanya M. Monro. Material candidates for optical frequency comb generation in microspheres. *Optics Express*, 23(11):14784, June 2015.

[40] Tal Carmon, Harald G. L. Schwefel, Lan Yang, Mark Oxborrow, A. Douglas Stone, and Kerry J. Vahala. Static Envelope Patterns in Composite Resonances Generated by Level Crossing in Optical Toroidal Microcavities. *Physical Review Letters*, 100(10):103905, March 2008.

[41] A. A. Savchenkov, A. B. Matsko, W. Liang, V. S. Ilchenko, D. Seidel, and L. Maleki. Kerr frequency comb generation in overmoded resonators. *Optics Express*, 20(24):27290, November 2012.

[42] Xiaoxiao Xue, Yi Xuan, Cong Wang, Pei-Hsun Wang, Yang Liu, Ben Niu, Daniel E. Leaird, Minghao Qi, and Andrew M. Weiner. Thermal tuning of Kerr frequency combs in silicon nitride microring resonators. *Optics Express*, 24(1):687, January 2016.

[43] Maxim Karpov, Martin H. P. Pfeiffer, Junqiu Liu, Anton Lukashchuk, and Tobias J. Kippenberg. Photonic chip-based soliton frequency combs covering the biological imaging window. *Nature Communications*, 9(1):1146, December 2018.

[44] Elham Nazemosadat, Attila Fülöp, óskar B. Helgason, Pei-Hsun Wang, Yi Xuan, Dan E. Leaird, Minghao Qi, Enrique Silvestre, Andrew M. Weiner, and Victor Torres-Company. Switching dynamics of dark-pulse Kerr frequency comb states in optical microresonators. *Physical Review A*, 103(1):013513, January 2021.

[45] Yang Liu, Yi Xuan, Xiaoxiao Xue, Pei-Hsun Wang, Steven Chen, Andrew J. Metcalf, Jian Wang, Daniel E. Leaird, Minghao Qi, and Andrew M. Weiner. Investigation of mode coupling in normal-dispersion silicon nitride microresonators for Kerr frequency comb generation. *Optica*, 1(3):137, September 2014.

[46] Xiaoxiao Xue, Yi Xuan, Pei-Hsun Wang, Yang Liu, Dan E. Leaird, Minghao Qi, and Andrew M. Weiner. Normal-dispersion microcombs enabled by

controllable mode interactions: Normal-dispersion microcombs. *Laser & Photonics Reviews*, 9(4):L23–L28, July 2015.

[47] Steven A. Miller, Yoshitomo Okawachi, Sven Ramelow, Kevin Luke, Avik Dutt, Alessandro Farsi, Alexander L. Gaeta, and Michal Lipson. Tunable frequency combs based on dual microring resonators. *Optics Express*, 23(16):21527, August 2015.

[48] Seung Hoon Lee, Dong Yoon Oh, Qi-Fan Yang, Boqiang Shen, Heming Wang, Ki Youl Yang, Yu-Hung Lai, Xu Yi, Xinbai Li, and Kerry Vahala. Towards visible soliton microcomb generation. *Nature Communications*, 8(1):1295, December 2017.

[49] Heming Wang, Yu-Kun Lu, Lue Wu, Dong Yoon Oh, Boqiang Shen, Seung Hoon Lee, and Kerry Vahala. Dirac solitons in optical microresonators. *Light: Science & Applications*, 9(1):205, December 2020.

[50] Xiaoxiao Xue, Yi Xuan, Yang Liu, Pei-Hsun Wang, Steven Chen, Jian Wang, Dan E. Leaird, Minghao Qi, and Andrew M. Weiner. Mode-locked dark pulse Kerr combs in normal-dispersion microresonators. *Nature Photonics*, 9(9):594–600, September 2015.

[51] Sangsik Kim, Kyunghun Han, Cong Wang, Jose A. Jaramillo-Villegas, Xiaoxiao Xue, Chengying Bao, Yi Xuan, Daniel E. Leaird, Andrew M. Weiner, and Minghao Qi. Dispersion engineering and frequency comb generation in thin silicon nitride concentric microresonators. *Nature Communications*, 8(1):372, December 2017.

[52] P. Del'Haye, O. Arcizet, M. L. Gorodetsky, R. Holzwarth, and T. J. Kippenberg. Frequency comb assisted diode laser spectroscopy for measurement of microcavity dispersion. *Nature Photonics*, 3(9):529–533, September 2009.

[53] Jiyang Ma, Xiaoshun Jiang, and Min Xiao. Kerr frequency combs in large-size, ultra-high-Q toroid microcavities with low repetition rates [Invited]. *Photonics Research*, 5(6):B54, December 2017.

[54] Shuangyou Zhang, Jonathan M. Silver, Toby Bi, and Pascal Del'Haye. Spectral extension and synchronization of microcombs in a single microresonator. *Nature Communications*, 11(1):6384, December 2020.

[55] Xu Yi, Qi-Fan Yang, Ki Youl Yang, Myoung-Gyun Suh, and Kerry Vahala. Soliton frequency comb at microwave rates in a high-Q silica microresonator. *Optica*, 2(12):1078, December 2015.

[56] Guoping Lin, Khaldoun Saleh, Rémi Henriet, Souleymane Diallo, Romain Martinenghi, Aurélien Coillet, and Yanne K. Chembo. Wide-range tunability, thermal locking, and mode-crossing effects in Kerr optical frequency combs. *Optical Engineering*, 53(12):122602, July 2014.

[57] S. M. Spillane, T. J. Kippenberg, O. J. Painter, and K. J. Vahala. Ideality in a Fiber-Taper-Coupled Microresonator System for Application to Cavity Quantum Electrodynamics. *Physical Review Letters*, 91(4):043902, July 2003.

[58] Faraz Monifi, Sahin Kaya Ozdemir, Jacob Friedlein, and Lan Yang. Encapsulation of a Fiber Taper Coupled Microtoroid Resonator in a Polymer Matrix. *IEEE Photonics Technology Letters*, 25(15):1458–1461, August 2013.

[59] Tal Carmon, Lan Yang, and Kerry J. Vahala. Dynamical thermal behavior and thermal self-stability of microcavities. *Optics Express*, 12(20):4742, October 2004.

[60] T. Herr, K. Hartinger, J. Riemensberger, C. Y. Wang, E. Gavartin, R. Holzwarth, M. L. Gorodetsky, and T. J. Kippenberg. Universal formation dynamics and noise of Kerr-frequency combs in microresonators. *Nature Photonics*, 6(7):480–487, July 2012.

[61] Bok Young Kim, Yoshitomo Okawachi, Jae K. Jang, Mengjie Yu, Xingchen Ji, Yun Zhao, Chaitanya Joshi, Michal Lipson, and Alexander L. Gaeta. Turn-key, high-efficiency Kerr comb source. *Optics Letters*, 44(18):4475, September 2019.

[62] Judith Su. Portable and sensitive air pollution monitoring. *Light: Science & Applications*, 7(1):3, s41377–018–0017–x, December 2018.

[63] Jae K. Jang, Yoshitomo Okawachi, Mengjie Yu, Kevin Luke, Xingchen Ji, Michal Lipson, and Alexander L. Gaeta. Dynamics of mode-coupling-induced microresonator frequency combs in normal dispersion. *Optics Express*, 24(25):28794, December 2016.

[64] M.-G. Suh, Q.-F. Yang, K. Y. Yang, X. Yi, and K. J. Vahala. Microresonator soliton dual-comb spectroscopy. *Science*, 354(6312):600–603, November 2016.

[65] Mengjie Yu, Yoshitomo Okawachi, Austin G. Griffith, Nathalie Picqué, Michal Lipson, and Alexander L. Gaeta. Silicon-chip-based mid-infrared dual-comb spectroscopy. *Nature Communications*, 9(1):1869, December 2018.

[66] Yanne K. Chembo and Curtis R. Menyuk. Spatiotemporal Lugiato-Lefever formalism for Kerr-comb generation in whispering-gallery-mode resonators. *Physical Review A*, 87(5):053852, May 2013.

[67] Jianqi Hu, Jijun He, Junqiu Liu, Arslan S. Raja, Maxim Karpov, Anton Lukashchuk, Tobias J. Kippenberg, and Camille-Sophie Brès. Reconfigurable radiofrequency filters based on versatile soliton microcombs. *Nature Communications*, 11(1):4377, December 2020.

[68] Gwangho Choi and Judith Su. Impact of stimulated raman scattering on dark soliton generation in a silica microresonator. *Journal of Physics: Photonics*, 5(1):014001, dec 2022.

[69] Kerry J. Vahala. Optical microcavities. *Nature*, 424(6950):839–846, August 2003.

[70] T. J. Kippenberg, R. Holzwarth, and S. A. Diddams. Microresonator-Based Optical Frequency Combs. *Science*, 332(6029):555–559, April 2011.

[71] Guoping Lin and Qinghai Song. Review on Kerr Frequency Comb Interaction with Raman, Brillouin, and Second Order Nonlinear Effects. *Laser & Photonics Reviews*, page 2100184, November 2021.

[72] S. M. Spillane, T. J. Kippenberg, and K. J. Vahala. Ultralow-threshold Raman laser using a spherical dielectric microcavity. *Nature*, 415(6872):621–623, February 2002.

[73] P. Del'Haye, A. Schliesser, O. Arcizet, T. Wilken, R. Holzwarth, and T. J. Kippenberg. Optical frequency comb generation from a monolithic microresonator. *Nature*, 450(7173):1214–1217, December 2007.

[74] Imad H. Agha, Yoshitomo Okawachi, Mark A. Foster, Jay E. Sharping, and Alexander L. Gaeta. Four-wave-mixing parametric oscillations in dispersion-compensated high- Q silica microspheres. *Physical Review A*, 76(4):043837, October 2007.

[75] Anatoliy A. Savchenkov, Andrey B. Matsko, Vladimir S. Ilchenko, Iouri Solomatine, David Seidel, and Lute Maleki. Tunable Optical Frequency Comb with a Crystalline Whispering Gallery Mode Resonator. *Physical Review Letters*, 101(9):093902, August 2008.

[76] T. Hansson, D. Modotto, and S. Wabnitz. Dynamics of the modulational instability in microresonator frequency combs. *Physical Review A*, 88(2):023819, August 2013.

[77] Luming Zhao, Dingyuan Tang, Xuan Wu, and Han Zhang. Dissipative soliton generation in Yb-fiber laser with an invisible intracavity bandpass filter. *Optics Letters*, 35(16):2756, August 2010.

[78] H. Zhang, D. Y. Tang, L. M. Zhao, and R. J. Knize. Vector dark domain wall solitons in a fiber ring laser. *Optics Express*, 18(5):4428, March 2010.

[79] Han Zhang, Dingyuan Tang, Luming Zhao, Qiaoliang Bao, and Kian Ping Loh. Vector dissipative solitons in graphene mode locked fiber lasers. *Optics Communications*, 283(17):3334–3338, September 2010.

[80] Yufeng Song, Xujie Shi, Chengfa Wu, Dingyuan Tang, and Han Zhang. Recent progress of study on optical solitons in fiber lasers. *Applied Physics Reviews*, 6(2):021313, June 2019.

[81] A Mahalingam, K Porsezian, M S Mani Rajan, and A Uthayakumar. Propagation of dispersion–nonlinearity-managed solitons in an inhomogeneous erbium-doped fiber system. *Journal of Physics A: Mathematical and Theoretical*, 42(16):165101, April 2009.

[82] S. Vijayalekshmi, M.S. Mani Rajan, A. Mahalingam, and A. Uthayakumar. Hidden possibilities in soliton switching through tunneling in erbium doped birefringence fiber with higher order effects. *Journal of Modern Optics*, 62(4):278–287, February 2015.

[83] Attila Fülöp, Mikael Mazur, Abel Lorences-Riesgo, Óskar B. Helgason, Pei-Hsun Wang, Yi Xuan, Dan E. Leaird, Minghao Qi, Peter A. Andrekson, Andrew M. Weiner, and Victor Torres-Company. High-order coherent communications using mode-locked dark-pulse Kerr combs from microresonators. *Nature Communications*, 9(1):1598, December 2018.

[84] Óskar B. Helgason, Francisco R. Arteaga-Sierra, Zhichao Ye, Krishna Twayana, Peter A. Andrekson, Magnus Karlsson, Jochen Schröder, and Victor Torres-Company. Dissipative solitons in photonic molecules. *Nature Photonics*, 15(4):305–310, April 2021.

[85] H. Liu, S.-W. Huang, J. Yang, M. Yu, D.-L. Kwong, and C. W. Wong. Bright square pulse generation by pump modulation in a normal GVD microresonator. In *Conference on Lasers and Electro-Optics*, page FTu3D.3, San Jose, California, 2017. OSA.

[86] Valery E. Lobanov, Nikita M. Kondratiev, Artem E. Shitikov, Ramzil R. Galiev, and Igor A. Bilenko. Generation and dynamics of solitonic pulses due to pump amplitude modulation at normal group-velocity dispersion. *Physical Review A*, 100(1):013807, July 2019.

[87] Hao Liu, Shu-Wei Huang, Wenting Wang, Jinghui Yang, Mingbin Yu, Dim-Lee Kwong, Pierre Colman, and Chee Wei Wong. Stimulated generation of deterministic platicon frequency microcombs. *Photonics Research*, 10(8):1877, August 2022.

[88] Wei Liang, Anatoliy A. Savchenkov, Vladimir S. Ilchenko, Danny Eliyahu, David Seidel, Andrey B. Matsko, and Lute Maleki. Generation of a coherent near-infrared Kerr frequency comb in a monolithic microresonator with normal GVD. *Optics Letters*, 39(10):2920, May 2014.

[89] Heming Wang, Boqiang Shen, Yan Yu, Zhiquan Yuan, Chengying Bao, Warren Jin, Lin Chang, Mark A. Leal, Avi Feshali, Mario Paniccia, John E. Bowers, and Kerry Vahala. Self-regulating soliton switching waves in microresonators. *Physical Review A*, 106(5):053508, November 2022.

[90] Grigory Lihachev, Wenle Weng, Junqiu Liu, Lin Chang, Joel Guo, Jijun He, Rui Ning Wang, Miles H. Anderson, Yang Liu, John E. Bowers, and Tobias J. Kippenberg. Platicon microcomb generation using laser self-injection locking. *Nature Communications*, 13(1):1771, April 2022.

[91] V.B. Braginsky, M.L. Gorodetsky, and V.S. Ilchenko. Quality-factor and nonlinear properties of optical whispering-gallery modes. *Physics Letters A*, 137(7-8):393–397, May 1989.

[92] Erol Ozgur, Kara Ellen Roberts, Ekin Ozge Ozgur, Adley Nathanael Gin, Jaden Robert Bankhead, Zhikun Wang, and Judith Su. Ultrasensitive Detection of Human Chorionic Gonadotropin Using Frequency Locked Microtoroid Optical Resonators. *Anal. Chem.*, 91(18):11872–11878, September 2019.

[93] Francesco Dell'Olio, Judith Su, Thomas Huser, Virginie Sottile, Luis Enrique Cortés-Hernández, and Catherine Alix-Panabières. Photonic Technologies for Liquid Biopsies: Recent Advances and Open Research Chal-

lenges. *Laser & Photonics Reviews*, 15(1):2000255, 2021. _eprint: https://onlinelibrary.wiley.com/doi/pdf/10.1002/lpor.202000255.

[94] Tao Lu, Tsu-Te Judith Su, Kerry J. Vahala, and Scott E. Fraser. Split frequency sensing methods and systems, November 2013.

[95] T. J. Kippenberg, S. M. Spillane, D. K. Armani, and K. J. Vahala. Ultralow-threshold microcavity Raman laser on a microelectronic chip. *Optics Letters*, 29(11):1224, June 2004.

[96] Maxim Karpov, Hairun Guo, Arne Kordts, Victor Brasch, Martin H.P. Pfeiffer, Michail Zervas, Michael Geiselmann, and Tobias J. Kippenberg. Raman Self-Frequency Shift of Dissipative Kerr Solitons in an Optical Microresonator. *Physical Review Letters*, 116(10):103902, March 2016.

[97] Qi-Fan Yang, Xu Yi, Ki Youl Yang, and Kerry Vahala. Stokes solitons in optical microcavities. *Nature Physics*, 13(1):53–57, January 2017.

[98] Teng Tan, Zhongye Yuan, Hao Zhang, Guofeng Yan, Siyu Zhou, Ning An, Bo Peng, Giancarlo Soavi, Yunjiang Rao, and Baicheng Yao. Multispecies and individual gas molecule detection using Stokes solitons in a graphene over-modal microresonator. *Nature Communications*, 12(1):6716, December 2021.

[99] Yoshitomo Okawachi, Mengjie Yu, Vivek Venkataraman, Pawel M. Latawiec, Austin G. Griffith, Michal Lipson, Marko Lončar, and Alexander L. Gaeta. Competition between Raman and Kerr effects in microresonator comb generation. *Optics Letters*, 42(14):2786, July 2017.

[100] Di Xia, Yufei Huang, Bin Zhang, Pingyang Zeng, Jiaxin Zhao, Zelin Yang, Suwan Sun, Liyang Luo, Guiying Hu, Dong Liu, Zifu Wang, Yufei Li, Hairun Guo, and Zhaohui Li. Engineered Raman Lasing in Photonic Integrated Chalcogenide Microresonators. *Laser & Photonics Reviews*, page 2100443, January 2022.

[101] Shunyu Yao, Chengying Bao, Pan Wang, and Changxi Yang. Generation of stable and breathing flat-top solitons via Raman assisted four wave mixing in microresonators. *Physical Review A*, 101(2):023833, February 2020.

[102] Guoping Lin and Yanne K. Chembo. Phase-locking transition in Raman combs generated with whispering gallery mode resonators. *Optics Letters*, 41(16):3718, August 2016.

[103] Ryo Suzuki, Akihiro Kubota, Atsuhiro Hori, Shun Fujii, and Takasumi Tanabe. Broadband gain induced Raman comb formation in a silica microresonator. *Journal of the Optical Society of America B*, 35(4):933, April 2018.

[104] Haizhong Weng, Jia Liu, Adnan Ali Afridi, Jing Li, Jiangnan Dai, Xiang Ma, Yi Zhang, Qiaoyin Lu, John F. Donegan, and Weihua Guo. Octave-spanning Kerr frequency comb generation with stimulated Raman scattering in an AlN microresonator. *Optics Letters*, 46(3):540, February 2021.

[105] Xianwen Liu, Changzheng Sun, Bing Xiong, Lai Wang, Jian Wang, Yanjun Han, Zhibiao Hao, Hongtao Li, Yi Luo, Jianchang Yan, Tongbo Wei, Yun Zhang, and Junxi Wang. Integrated High- Q Crystalline AlN Microresonators for Broadband Kerr and Raman Frequency Combs. *ACS Photonics*, 5(5):1943–1950, May 2018.

[106] Bumki Min, Lan Yang, and Kerry Vahala. Controlled transition between parametric and Raman oscillations in ultrahigh-Q silica toroidal microcavities. *Applied Physics Letters*, 87(18):181109, October 2005.

[107] Ivan S. Grudinin, Lukas Baumgartel, and Nan Yu. Impact of cavity spectrum on span in microresonator frequency combs. *Optics Express*, 21(22):26929, November 2013.

[108] Yu Yang, Shuai Zhao, Yuan Shen, Lingjun Meng, Tianci Chen, Ziwen Huang, Lei Zhang, and Keyi Wang. Transition From Kerr Comb to Raman Soliton Comb in Micro-Rod Resonator for Broadband Comb Applications. *IEEE Journal of Quantum Electronics*, 57(6):1–6, December 2021.

[109] Yanne K. Chembo, Ivan S. Grudinin, and Nan Yu. Spatiotemporal dynamics of Kerr-Raman optical frequency combs. *Physical Review A*, 92(4):043818, October 2015.

[110] Victor Torres-Company, David Castelló-Lurbe, and Enrique Silvestre. Comparative analysis of spectral coherence in microresonator frequency combs. *Optics Express*, 22(4):4678, February 2014.

[111] Shun Fujii, Takumi Kato, Ryo Suzuki, Atsuhiro Hori, and Takasumi Tanabe. Transition between Kerr comb and stimulated Raman comb in a silica whispering gallery mode microcavity. *Journal of the Optical Society of America B*, 35(1):100, January 2018.

[112] Zong-Ren Yang and Pei-Hsun Wang. Stability analysis of mode-coupling-assisted microcombs in normal dispersion. *Optics Express*, 30(21):37637, October 2022.

[113] C. Milián, A. V. Gorbach, M. Taki, A. V. Yulin, and D. V. Skryabin. Solitons and frequency combs in silica microring resonators: Interplay of the Raman and higher-order dispersion effects. *Physical Review A*, 92(3):033851, September 2015.

[114] Guoping Lin, Souleymane Diallo, John M. Dudley, and Yanne K. Chembo. Universal nonlinear scattering in ultra-high Q whispering gallery-mode resonators. *Optics Express*, 24(13):14880, June 2016.

[115] Chengying Bao, Jose A. Jaramillo-Villegas, Yi Xuan, Daniel E. Leaird, Minghao Qi, and Andrew M. Weiner. Observation of Fermi-Pasta-Ulam Recurrence Induced by Breather Solitons in an Optical Microresonator. *Physical Review Letters*, 117(16):163901, October 2016.

[116] Takumi Kato, Atsuhiro Hori, Ryo Suzuki, Shun Fujii, Tomoya Kobatake, and Takasumi Tanabe. Transverse mode interaction via stimulated Raman scattering comb in a silica microcavity. *Optics Express*, 25(2):857, January 2017.

[117] Yadong Wang, Miles Anderson, Stéphane Coen, Stuart G. Murdoch, and Miro Erkintalo. Stimulated Raman Scattering Imposes Fundamental Limits to the Duration and Bandwidth of Temporal Cavity Solitons. *Physical Review Letters*, 120(5):053902, January 2018.

[118] Zheng Gong, Xianwen Liu, Yuntao Xu, and Hong X. Tang. Near-octave lithium niobate soliton microcomb. *Optica*, 7(10):1275, October 2020.

[119] A. V. Cherenkov, N. M. Kondratiev, V. E. Lobanov, A. E. Shitikov, D. V. Skryabin, and M. L. Gorodetsky. Raman-Kerr frequency combs in microresonators with normal dispersion. *Optics Express*, 25(25):31148, December 2017.

[120] Mulong Liu, Huimin Huang, Zhizhou Lu, Yuanyuan Wang, Yanan Cai, and Wei Zhao. Dynamics of dark breathers and Raman-Kerr frequency combs influenced by high-order dispersion. *Optics Express*, 29(12):18095, June 2021.

[121] P. Parra-Rivas, S. Coulibaly, M. G. Clerc, and M. Tlidi. Influence of stimulated Raman scattering on Kerr domain walls and localized structures. *Physical Review A*, 103(1):013507, January 2021.

[122] Shun Fujii, Yusuke Okabe, Ryo Suzuki, Takumi Kato, Atsuhiro Hori, Yoshihiro Honda, and Takasumi Tanabe. Analysis of Mode Coupling Assisted Kerr Comb Generation in Normal Dispersion System. *IEEE Photonics Journal*, 10(5):1–11, October 2018.

[123] N.R. Newbury. Pump-wavelength dependence of Raman gain in single-mode optical fibers. *Journal of Lightwave Technology*, 21(12):3364–3373, December 2003.

[124] Q. Lin and Govind P. Agrawal. Raman response function for silica fibers. *Optics Letters*, 31(21):3086, November 2006.

[125] G. P. Agrawal. *Nonlinear fiber optics*. Academic Press, London, United Kingdom ; San Diego, CA, United States, sixth edition edition, 2019. OCLC: on1112387654.

[126] Chengying Bao, Yi Xuan, Cong Wang, Attila Fülöp, Daniel E. Leaird, Victor Torres-Company, Minghao Qi, and Andrew M. Weiner. Observation of Breathing Dark Pulses in Normal Dispersion Optical Microresonators. *Physical Review Letters*, 121(25):257401, December 2018.

[127] Di Xia, Zelin Yang, Pingyang Zeng, Bin Zhang, Jiayue Wu, Zifu Wang, Jiaxin Zhao, Jianteng Huang, Liyang Luo, Dong Liu, Shuixian Yang, Hairun Guo, and Zhaohui Li. Integrated Chalcogenide Photonics for Microresonator Soliton Combs. *Laser & Photonics Reviews*, page 2200219, November 2022.

[128] P. Parra-Rivas, E. Knobloch, D. Gomila, and L. Gelens. Dark solitons in the Lugiato-Lefever equation with normal dispersion. *Physical Review A*, 93(6):063839, June 2016.

[129] Pedro Parra-Rivas, Damià Gomila, Edgar Knobloch, Stéphane Coen, and Lendert Gelens. Origin and stability of dark pulse Kerr combs in normal dispersion resonators. *Optics Letters*, 41(11):2402, June 2016.

[130] Haowen Shu, Lin Chang, Yuansheng Tao, Bitao Shen, Weiqiang Xie, Ming Jin, Andrew Netherton, Zihan Tao, Xuguang Zhang, Ruixuan Chen, Bowen Bai, Jun Qin, Shaohua Yu, Xingjun Wang, and John E. Bowers. Microcomb-driven silicon photonic systems. *Nature*, 605(7910):457–463, May 2022.

[131] Jin Li, Shuai Wan, Jin-Lan Peng, Zheng-Yu Wang, Rui Niu, Chang-Ling Zou, Guang-Can Guo, and Chun-Hua Dong. Thermal tuning of mode crossing and the perfect soliton crystal in a Si $_3$ N $_4$ microresonator. *Optics Express*, 30(8):13690, April 2022.

[132] Cyril Godey, Irina V. Balakireva, Aurélien Coillet, and Yanne K. Chembo. Stability analysis of the spatiotemporal Lugiato-Lefever model for Kerr optical frequency combs in the anomalous and normal dispersion regimes. *Physical Review A*, 89(6):063814, June 2014.

[133] Xiaoqin Shen, Rigoberto Castro Beltran, Vinh M. Diep, Soheil Soltani, and Andrea M. Armani. Low-threshold parametric oscillation in organically modified microcavities. *Science Advances*, 4(1):eaao4507, January 2018.

[134] Jose A. Jaramillo-Villegas, Xiaoxiao Xue, Pei-Hsun Wang, Daniel E. Leaird, and Andrew M. Weiner. Deterministic single soliton generation and compression in microring resonators avoiding the chaotic region. *Optics Express*, 23(8):9618, April 2015.

[135] Enxu Zhu and Chaoying Zhao. Modulation instability of Kerr optical frequency combs in dual-coupled optical cavities. *Physical Review A*, 105(1):013524, January 2022.